

**Simplified Cardiodynamic Tissue Electrophysiology Characterization, Reduced Order
Modeling with Therapeutic Perspective**

A Thesis
Submitted to the Faculty
of
Drexel University
by
Celal Alagöz
in fulfillment of the
requirements for the degree
of
Doctor of Philosophy
May 2017



© Copyright 2017
Celal Alagöz.

This work is licensed under the terms of the Creative Commons Attribution-ShareAlike
license Version 3.0. The license is available at
<http://creativecommons.org/licenses/by-sa/3.0/>.

Dedications

To Yasemin and Meryem, my beloved ones.

Acknowledgments

"How could it be that He who has created (all) should not know (all)?..." - Qur'an 67:14

First and foremost, all my gratitudes ultimately goes to my Lord who grants existence of both myself and whatever I interact with. He is the necessarily existent on whom every other being is contingent. I feel full of excitement and life whenever I reflect on the sign that all beings with all qualities manifested on them point to existence of only His Knowledge and Power.

I thank my advisor Allon Guez for his supervision and mentoring during my studies. I benefited from his experience and his approach towards the knowledge in general. Besides, conceive and coordination of the project, he has been quite responsive and consistent in his supervision during the dissertation process.

I thank John Bullinga for his guidance and help in development of my knowledge in state of the art in the medical field. I also thank Daniel Frisch for his review and constructive feedbacks regarding medical background of the thesis. I thank Nagarajan Kandasamy, Paul Kalata, and Andrew Cohen for their willingness to serve on the committee and for their constructive suggestions.

I thank my fellow graduate students Saran Phatharodom and Oday Bshara for their friendship. Saran's discussions and immediate feedbacks, especially his questions and curiosity have been a driving force. In brief, offering his genuine partnership during the project, he has been far more than an average colleague for me.

I thank Yusuf Osmanlioğlu, Salih Tolga Özaslan, Birkan Tunç, Mustafa Ömer Furkan, Osman Demir, Murat Çıkan, Furkan Salman, Gökmen Durmuş, Abdurrahman Gümüş, and Ziya Ete for their congenial companionship that rendered my times in Philadelphia more fruitful. Each, in a particular way, has been means for me to see there is much more to the life than my mere academic endeavors.

I thank mother and father, Cennet and Ali for their unflappable support, understanding and care during my pretty long abroad times. I also thank my siblings Ramazan, Şerife, İsa, Hacı Ahmed,

Selma, Feride, Mehmet Akif and all my nephew and nieces for their invaluable care and bond. Hacı Ahmed's genuine interest in my studies and his discussions has kept my enthusiasm uplifted. İsa's support in administrative parts of my life during the studies provided comfort and security for me. I also thank mother and father in law, Rahime and Abidin, together with sister and brother in law, Fatma Kübra and İsmail for their unceasing support and trust.

Last but not least, my special gratitude goes to my wife Yasemin for her understanding and patience. Her positive attitude has boosted my motivation and determination. Her and our daughter Meryem's presence has been a blessed haven for me.

Table of Contents

LIST OF TABLES	viii
LIST OF FIGURES	ix
ABSTRACT	xv
I INTRODUCTION AND BACKGROUND	1
1. INTRODUCTION	2
1.1 Reduced Order Modeling of Cardiac Tissue	3
1.2 Simplified Cardiodynamic Tissue Characterization	4
2. ATRIAL FIBRILLATION BACKGROUND	7
2.1 Definition	7
2.1.1 Epidemiology and Prognosis	8
2.2 Cardiac Electrophysiology	9
2.2.1 Action Potential	10
2.3 Pathophysiology and Mechanism	12
2.3.1 Basic Mechanisms	13
2.3.2 Tissue Mechanisms	14
2.4 Atrial Remodeling	20
2.4.1 Electrical Remodeling	20
2.4.2 Structural Remodeling	21
2.5 Treatment Options	21
2.5.1 Rate and Rhythm Control	22
2.5.2 Catheter Ablation	23
2.6 Cardiac Electroanatomical Mapping	25
2.6.1 Mapping Tools	26
2.6.2 Computational Mapping Techniques	27

3. CARDIAC ELECTROPHYSIOLOGY SIMULATION	32
3.1 Modeling Cardiac Electrophysiology	32
3.1.1 Human Cardiac Models	32
3.2 Cardiac Electrical Restitution	34
3.3 Numerical Methods	37
3.3.1 PDE Solution	38
3.3.2 Simulating Electrograms	38
3.3.3 Parallel Computation Using GPUs	39
II METHODS	43
4. REDUCED ORDER CARDIAC MODELING	44
4.1 Electrophysiological Models	44
4.2 Electrophysiological Properties	47
4.3 Parameter Estimation Schemes	50
4.3.1 Extended Kalman Filter	51
4.3.2 Sequential Quadratic Programming	56
4.3.3 Particle Swarm Optimization	57
5. SIMPLIFIED CARDIODYNAMIC TISSUE CHARACTERIZATION	59
5.1 Simulating Spiral Waves and Intra-cardiac Electrograms	60
5.2 Normalized Compression Distance	67
5.3 Normalized Compression Distance with Feature Bias	68
5.4 Clustering	70
5.4.1 Spectral Clustering	70
5.4.2 Cluster Analysis	71
5.5 Classification	72
III RESULTS AND DISCUSSIONS	73
6. RESULTS: REDUCED ORDER CARDIAC MODELING	74
6.1 EKF Analysis	74

6.2	Heterogeneous Action Potential Fitting	77
6.3	Electrically Remodeled Action Potential Fitting	78
6.4	Limitations	84
7.	RESULTS: SIMPLIFIED CARDIODYNAMIC TISSUE CHARACTERIZATION	85
7.1	Clustering Analysis	85
7.2	Classification Analysis	86
7.3	Analysis of Robustness in Classification	89
7.4	Discussions	93
7.4.1	Clinical Implications and Future Works	93
7.4.2	Relevance to Clinical Applications	94
7.4.3	Limitations	96
8.	CONCLUSIONS	97
	BIBLIOGRAPHY	100
	APPENDIX A: MINIMAL RESISTOR MODEL EQUATIONS	113
	APPENDIX B: MINIMAL RESISTOR MODEL PARAMETERS	115
	APPENDIX C: SPIRAL WAVE GENERATION	117
	VITA	130

List of Tables

4.1	Human atrial AP heterogeneity	48
4.2	Constructing electrically remodeled CRN model	49
5.1	Parameter Analysis of MRM	64
7.1	Classification Performance for Measurement Setups	89
7.2	Classification performance for inter-measurement configurations.	90
7.3	Inter Locations 3 and 5 Classification	91
7.4	Inter Locations 3 and 5 with Noise Classification	91
B.1	Upper and lower bounds of MRM parameters	115
B.2	Fitted Parameters of MRM for Afib-AP under dynamic stimuli.	115
B.3	Parameters sets of MRM used for spiral wave generation	116

List of Figures

1.1	Presentation of the problems, scales, components and approaches categorized under two experiments conducted in the present thesis.	3
2.1	Schematic representation of natural time course of Afib progression for a typical patient. Gray areas represent the time periods where sinus rhythm and black ones represent when the . Adopted from [Schotten et al. ¹]	8
2.2	Electrophysiology of heart with (A) Normal rhythm and (B) Atrial fibrillation. Adopted from [Wakili et al. ²]	9
2.3	AP from human atria (on left) and ventricle (on right). Adopted from [Ehrlich et al. ³] .	11
2.4	A representation of the mechanisms on different level interacting and leading to Afib. Adopted from [Nattel ⁴]	12
2.5	Ectopic firing mechanism at the cellular level. A) Spontaneous firing, B) Delayed afterdepolarization, and C) Early afterdepolarization. Adopted from Nattel et al. ⁵	13
2.6	Schematic representation of generally accepted mechanisms of Afib. (A) Ectopic foci causing discordant propagation, (B) Single-circuit reentry generally around a conduction block, (C) Multiple-circuit reentry, (D) Relationship between Afib patterns, mechanisms, and remodeling. Adopted from Iwasaki et al. ⁶	15
2.7	Mother rotor observed in an experimental setup (a) and simulation (b). Adopted from [Cherry and Fenton ⁷]	19
2.8	Therapeutic flow diagram for Afib.	22
2.9	Afib ablation strategies. Adopted from Calkins et al. ⁸	24
2.10	Cardiac mapping tools used commonly in AF therapy.	27
2.11	The setup for the computational mapping of electrical rotors during AF from FIRM study group. A) Intracardiac Electrgrams B) Monitoring 64-pole basket catheter replacement in both atria using fluoroscopy C) Isochronal maps computed through activation times reveal the rotors 3 consecutive revolution in both left and right atria. D) Respective activation times captured from the filtered ECG signals represented. Adopted from Narayan et al. ⁹	29
2.12	Characterization of unipolar electrograms from [Konings et al. ¹⁰]	30
3.1	Schematic representation of cellular components such as ionic currents, pumps and ion exchangers. The interactions happen between 3 mediums: myoplasm, junctional sarcoplasmic reticulum (JSR) and network sarcoplasmic reticulum (NSR). Adopted from Courtemanche et al. ¹¹	33
3.2	APs reproduced through various cardiac electrophysiological models for different regions of the heart and for different species. Adopted from Cherry and Fenton ⁷	34

3.3	Electrical restitution curve derivation. (A) S1S2 protocol to derive APD restitution curve. Here, first stimulus S1 with a fixed frequency is applied for a number of times and then the second stimulus S2 with varying frequency is applied at each time that results different DIs and APDs. (B) A standard APD restitution curve. Adopted from Qu et al. ¹²	36
3.4	Comparison between CPU and GPU architectures. Adopted from Corporation ¹³	40
3.5	Memory architecture for a typical GPU. Adopted from Programming ¹⁴	41
4.1	Model complexity reduction block diagram	45
4.2	Comparison of computational speed between MRM and CRN.	46
4.3	Representation of electrophysiological properties from cellular to organ level with different characteristics used for different fitting-testing purposes.	47
4.4	APs of different cell types from atrial regions PM, CT, APG, and AVR. (a) Experimentally measured heterogeneous APs by Feng et al. [Feng et al. ¹⁵] and (b) modeled APs. Figure from Seemann et al. ¹⁶ .	48
4.5	Healthy and Afib based electrically remodeled APs experimentally recorded from patients are respectively compared with modeled ones. Figure from Courtemanche et al. ¹⁷ .	49
4.6	Visualization of estimated parameter evaluation and error computation for (a) APD, (b) APD standard restitution during EKF implementation. Indication of normalized changes in the estimated parameters at a filtering step with respect to their initial values (c).	56
5.1	Spiral waves characterization work-flow	60
5.2	Spiral behavior prototypes simulated on 10 cm x 10 cm 2D patches (a) with corresponding recorded unipolar electrograms measured from the center of each patch (b), DF, OI and RI (c), and CL histogram (d) extracted for demonstration purpose only. In this case, only RI and OI parameters for stationary spiral behavior results in distinct values. OI: Organization index, RI: Regularity index, DF: Dominant Frequency, CL: Cycle Length.	61
5.3	Left: Spiral wave using the MRM on a 512 x 512 grid. Middle: Simulation speed comparison between GPU with texture memory used and CPU. Right: Simulation speed comparison of GPU with global memory used versus texture memory used. Grid dimension represents the number of elements (cells) on one side of rectangular lattice on which the simulation was performed.	62
5.4	Snapshots of spiral waves and their corresponding tip movements when τ_w^+ and τ_w^- varied. Adopted from Bartocci et al. ¹⁸	63
5.5	An example that represents the simulation of monopolar EGMs (c) with respective APs (b) through simulation of a spiral wave breakup on a 2D patch of 10cm x 10cm (a) for which parameter set EKF (see Table B.3) with $\tau_w^+=250$, $\tau_{w1}^-=250$, $\tau_{w2}^-=140$, $\tau_{fi}=0.05$, $\tau_{si}=20$, and $\tau_{so1}=50$ is used. Readings are taken from the center of the patch which is shown with a red marker.	65

5.6	Delineation of simulation and electrogram recording setup and data handling. (a) Snapshot of a meandering spiral wave simulation on the 25.6 cm x 25.6 cm grid. The locations catheters positioned (in this case only the spiral shaped catheter) are also shown. (b) A close view on modeled catheters displaying electrode positions and configurations. (c) Unipolar electrograms recorded at Location 4. (d) Recorded unipolar electrograms represented as a digital dataset as being stacked columnwise to form a matrix and being converted to image.	66
5.7	Unipolar EGMs spike detection. Nonlinear energy of the signal is derived first (a), then negative (blue x-mark) and positive (red x-mark) deflections are detected (b) which are used to extract CL and EGM morphology parameters. After extracting features, they are tiled into respective unipole channels and the channels are then stacked vertically as shown in part (c). Note that the length for each channel together with for each simulated behavior can vary since number of resulting features is not fixed for each case. Also features represented in this paper are either CLs or EGM morphology indices or consecutive addition of both. Any of two behaviors are concatenated vertically as shown in part (c).	69
6.1	Goodness of fitting comparison for EKF under different magnitudes of measurement and process noise covariances.	75
6.2	Change in error values over the course of EKF implementation.	76
6.3	Fitting results of heterogeneous APs throughout human atria through the estimation schemes EKF, SQP, and PSO. For each case, NRMSE of AP is evaluated.	77
6.4	Goodness of fitting comparison for EKF, SQP, and PSO.	79
6.5	Fitting results for matching train of APs resulted from dynamic pacing of an Afib based electrically remodeled cell. Fitting performance is compared through the estimation schemes EKF, SQP, and PSO. In each case, NRMSEs of AP and APD Standard RC are simultaneously evaluated.	80
6.6	An example of different AP shapes obtained from different parameter sets resulting the similar APD standard RC.	81
6.7	Diffusion coefficient adjustment of MRM parameters estimated through EKF, SQP, and PSO for the case of dynamic APs fitting. Diffusion coefficient of CRN, σ , is set as reference conductivity rate for the rest.	82
6.8	Excitation propagation comparison between CRN and estimated MRM parameters through EKF, SQP, and PSO for the dynamic pacing. Spiral waves for each case is initiated using cross-field stimulation protocol. The time for the delivery the second wave is set as initial time and excitation pattern is demonstrated through snapshots from different time instants.	83
7.1	Comparison of parameters extracted from unipolar electrograms representing each spiral behaviors. Measurements were taken from the first unipole of PentaRay catheter from <i>Location 4</i> of the tissue.	86

7.2	Spectral clustering with respective gap statistics for various distance measure assessments using feature-free NCD approach with <code>bzip2</code> (a) and <code>gzip</code> (b), or using feature-biased approach with NFFTD (c), the series of EGM morphology indices (d) and of CLs (e) or of both (f). Optimal number of classes for each case, k , estimated via gap statistics are put in respective gap value plots. Ground truth and estimated labels are represented with colors and marker sizes, respectively (shown on top-right). Measurements were taken from PentaRay catheter on <i>Location 5</i> with unipolar readings. (JI: Jaccard index, NMI: Normalized Mutual Information)	87
7.3	True classification rate comparison for different compression techniques. Specifically, featurefree NCD schemes using different compressors and feature-biased distance measure assesment techniques are involved in the comparison.	88
7.4	Display of effect of noise on a piece of unipolar EGM signal.	90
7.5	Classification of spiral behaviors in case of heterogeneous spiral behavior distribution around the tissue patch. Each case is represented with four snapshots taken at 2.5, 5, 7.5 and 10 s. Classified behaviors at each location is labeled with respective spiral behavior. S: Stationary, M: Meander, B: Breakup.	92
8.1	A diagram representing a system identification scheme that may lead to development of patient - specific electrophysiology modeling and simulation. Components inside the dashed box represent the workflow to be done only in a clinical environment.	98
C.1	Respective APs and APD restitutions for the parameter sets EPI, ENDO, and EKF. . .	118
C.2	Snapshots of spiral waves and their corresponding APs and APD restitutions when parameters varied for producing stationary spiral behaviors using the parameter set EPI. τ_{fi} is fixed at 0.05, τ_{si} is varied as 2 and 3, τ_w^+ varied between 25 and 125, τ_w^- is varied between 50 and 400, and τ_{so1} is varied as 20 and 40. Spiral wave led to breakup for same parameter combinations associated with longer APD and steeper APD restitution curves. Spiral wave is not sustained, indicated by the images with only green background, for the parameter regimes that result longer APDs.	119
C.3	Snapshots of spiral waves and their corresponding APs and APD restitutions when parameters varied for producing stationary spiral behaviors using the parameter set ENDO. τ_{fi} is fixed at 0.05, τ_{si} is varied between 2 and 6, τ_w^+ varied between 10 and 400, τ_w^- is fixed at 400, and τ_{so1} varied between 20 and 80. Spiral wave led to breakup for same parameter combinations associated with longer APD and steeper APD restitution curves. Spiral wave is not sustained, indicated by the images with only green background, for the parameter regimes that result longer APDs and highly steep APD resitution curves.	120
C.4	Snapshots of spiral waves and their corresponding APs and APD restitutions when parameters varied for producing stationary spiral behaviors using the parameter set EKF. τ_{fi} is fixed at 0.05, τ_{si} is varied between 2 and 6, τ_w^+ varied between 10 and 400, τ_w^- is fixed at 400, and τ_{so1} varied between 20 and 80. Spiral wave led to breakup for same parameter combinations associated with longer APD and steeper APD restitution curves. Spiral wave is not sustained, indicated by the images with only green background, for the parameter regime that result longer APDs and highly steep APD resitution curves.	121

- C.5 Snapshots of spiral waves and their corresponding APs and APD restitutions when parameters varied for producing meandering spiral behaviors using the parameter set EPI. τ_{fi} is varied as 0.1 and 0.2, τ_{si} is varied as 1.5 and 2, τ_w^+ varied between 150 and 350, τ_w^- varied between 50 and 400, and τ_{so1} varied between 30 and 50. Spiral wave is not sustained, indicated by the images with only green background, for parameter regimes that result longer APDs and highly steep APD resitution curves. 122
- C.6 Snapshots of spiral waves and their corresponding APs and APD restitutions when parameters varied for producing meandering spiral behaviors using the parameter set ENDO (top) and EKF (bottom). In case of ENDO, τ_{fi} is fixed at 0.2, τ_{si} is varied as 2 and 4, τ_w^+ varied between 50 and 350, τ_w^- varied between 50 and 400, and τ_{so1} varied between 30 and 50. In case of EKF, τ_{fi} is fixed at 0.3, τ_{si} is varied as 3 and 4, τ_w^+ varied between 200 and 400, τ_w^- varied between 200 and 400, and τ_{so1} varied between 40 and 50. Spiral wave is not sustained, indicated by the images with only green background, for parameter regimes that result longer APDs and highly steep APD resitution curves. 123
- C.7 Snapshots of spiral waves and their corresponding APs and APD restitutions when parameters varied for producing spiral breakup behaviors using the parameter set EPI. τ_{si} is fixed at 2, τ_{fi} is varied as 0.05 and 0.075, τ_w^+ varied between 225 and 400, τ_w^- varied between 120 and 400, and τ_{so1} varied between 25 and 30. Breakup did not take place for parameter regimes associated with shorter APDs and more flat APD restitution curve. Also, spiral wave is not sustained, indicated by the images with only green background, for parameter regimes that result longer APDs and highly steep APD resitution curves. 124
- C.8 Snapshots of spiral waves and their corresponding APs and APD restitutions when parameters varied for producing spiral breakup behaviors using the parameter set EPI. τ_{fi} is fixed at 0.11, τ_{si} is fixed at 1.89, τ_w^+ varied between 230 and 390, τ_w^- varied between 140 and 380, and τ_{so1} varied between 20 and 30. Breakup did not take place for parameter regimes associated with shorter APDs and more flat APD restitution curve. Also, spiral wave is not sustained, indicated by the images with only green background, for parameter regimes that result longer APDs and highly steep APD resitution curves. 125
- C.9 Snapshots of spiral waves and their corresponding APs and APD restitutions when parameters varied for producing spiral breakup behaviors using the parameter set ENDO. τ_{fi} is fixed at 0.05, τ_w^+ varied between 150 and 400, τ_w^- varied between 200 and 400, τ_{si} varied as 2 and 3 and τ_{so1} varied between 40 and 60. Breakup did not take place for parameter regimes associated with shorter APDs and rather flat APD restitution curve. Also, spiral wave is not sustained, indicated by the images with only green background, for parameter regimes that result longer APDs and highly steep APD resitution curves. 126
- C.10 Snapshots of spiral waves and their corresponding APs and APD restitutions when parameters varied for producing spiral breakup behaviors using the parameter set ENDO. τ_{fi} is fixed at 0.05, τ_w^+ varied between 150 and 400, τ_w^- varied between 200 and 350, τ_{si} varied as 1 and 1.5 and τ_{so1} varied between 40 and 60. Breakup did not take place for parameter regimes associated with shorter APDs and rather flat APD restitution curve. Also, spiral wave is not sustained, indicated by the images with only green background, for parameter regimes that result longer APDs and highly steep APD resitution curves. 127

- C.11 Snapshots of spiral waves and their corresponding APs and APD restitutions when parameters varied for producing spiral breakup behaviors using the parameter set EKF. τ_{fi} is fixed at 0.05, τ_w^+ varied between 150 and 400, τ_w^- varied between 200 and 350, τ_{si} varied as 2 and 3 and τ_{so1} varied between 40 and 60. Breakup did not take place for parameter regimes associated with shorter APDs and rather flat APD restitution curve. Also, spiral wave is not sustained, indicated by the images with only green background, for parameter regimes that result longer APDs and highly steep APD resitution curves. 128
- C.12 Snapshots of spiral waves and their corresponding APs and APD restitutions when parameters varied for producing spiral breakup behaviors using the parameter set EKF. τ_{fi} is fixed at 0.05, τ_w^+ varied between 150 and 400, τ_w^- varied between 200 and 400, τ_{si} varied as 1 and 1.5 and τ_{so1} varied between 40 and 60. Breakup did not take place for parameter regimes associated with shorter APDs and rather flat APD restitution curve. Also, spiral wave is not sustained, indicated by the images with only green background, for parameter regimes that result longer APDs and highly steep APD resitution curves. 129

Abstract

Simplified Cardiodynamic Tissue Electrophysiology Characterization, Reduced Order Modeling
with Therapeutic Perspective

Celal Alagöz

Allon Guez, Ph.D.

Atrial fibrillation (Afib) is the most common cardiac arrhythmia affecting millions of people around the world. Mapping and analysis of electrical activation patterns such as electric rotors during Afib is crucial in understanding arrhythmic mechanisms and assessment of diagnostic measures. To date, there exists various mapping studies where '*quantitative*' features such as local activation time, dominant frequency, wave direction, and conduction velocity are extracted from recorded intracardiac electrograms (EGMs). However, obtaining quantitative features further adds to multiplicity of the data and henceforth does not help interpretation of measured signals as opposed to using a more compressed diagnostic terms such as linking the measurements to reentry mechanisms. Through some techniques it is possible to construct isopotential and phase mappings by the help of monophasic action potential recordings in higher spatial resolution. In those cases, however, both expensive mapping tools performing multi-site simultaneous recordings which are not available to most of electrophysiologists are required. On the other hand, the most commonly used catheters which provide high resolution but local measurements remain rather rudimentary in mapping a spatially more global arrhythmic behaviors in a simultaneous fashion.

Spiral waves are tissue level phenomena observed in both clinical and experimental settings. They are the product of electrical rotors which are associated with reentry mechanisms during Afib. They can be reproduced using computer models of cardiac electrical activity. Current computer models vary in complexity, accuracy, and efficiency. One particular type is called biophysical models which are based on detailed ion channel interactions. Besides being computationally demanding, they are exceedingly complex and intractable preventing their use in a systems approach where multilevel events are generally considered together. Phenomenological models, on the other hand, include summarized details of ionic events yet preserve fundamental biophysical accuracy. A particular one

of them, a minimal resistor model (MRM), was shown to reproduce relevant basic electrophysiological behaviors such as (action potential) AP and electrical restitution properties for human ventricular tissue.

The objective in present thesis is to '*qualitatively*' characterize fibrillatory wavefront propagation dynamics in cardiac tissue using simulated intracardiac EGMs obtained from most commonly used and lower cost catheter types providing high resolution but localized readings. Another purpose connected to the previous is to show adequacy of a phenomenological model, MRM, in reproducing biophysically related behaviors for human atria. In this respect, two category of problems are handled throughout the thesis: (1) parameter estimation of MRM and (2) discrimination of spiral wave behaviors through intracardiac EGMs simulated using MRM. In the first part, representativeness of MRM for human atrial electrophysiology is established through adaptation of it to a biophysically detailed model originated from experimental data. Specifically, a method is proposed for parameter estimation of the simple model, MRM, to match a targeted behavior such as AP and electrical restitutions first generated from a complex model, by using extended Kalman filter (EKF). In the second part, a method that receives intracardiac EGMs and returns corresponding wavefront propagation patterns classified in terms of electric rotor dynamics is introduced. The method incorporates an information theoretical distance which is called normalized compression distance (NCD) used for assessment of distance measure between simulated behaviors. Achieving outstanding performance together with robustness in discrimination through usage of simulated data enables a theoretical validation of the method. Proposed frameworks collectively yield (1) potential usability of a computationally efficient and easier in analysis model for tissue level cardiac events and (2) simplicity and practicality in clinics through a mapping from a multiple, complex EGM signals to electric rotor behaviors, symptoms more relevant to the diagnosis.

Part I

Introduction and Background

Chapter 1: Introduction

The present thesis is studied under two category of problems: Adaptation of a phenomenological model to represent human atrial electrophysiology properties and characterization of simulated cardiac tissue fibrillatory patterns. In this chapter, problem statements with a brief state of art in the fields of computer modeling of cardiac electrophysiology and analysis of fibrillatory dynamics are discussed and afterwards respective objectives and approaches in the thesis are highlighted. At first, a preface that covers logistics of experimental design in both parts is provided.

The problems studied in this thesis lead to two main tasks: (1) Parameter estimation of a phenomenological cardiac model and (2) classification of simulated spiral wave patterns. Figure 1.1 depicts a summary of the problems, the scales, components and the approaches taken for each category which are named as Experiment I and II, respectively. In the first part, the problem is defined as reproducing basic electro-physiological properties for human atria. The model operates here on cellular level and accordingly the observed outputs and measurements are on the scale of trans-membrane voltage. The signal used in that experiment is then a single channel time-varying EGM. Therefore, the objective is to minimize the error between the observed output which is originally from human atria and reproduced by a biophysical model and the measurement from a phenomenological model. The task thereby is to estimate the parameters of the phenomenological model. In the second part, the problem is to characterize the spiral wave patterns simulated using the phenomenological model whose parameters were tweaked in the first part. The model works on the tissue level, a 2D patch in this context, hence the components are a network of cells. The measurements are on the scale of EGMs which are basically surface potentials recorded through a multi-electrode catheter. The signal used is then characterized as multi-channel and time-varying. Therefore, the task is to classify the simulated spiral behaviors using simulated EGMs locally measured by the catheter which in effect involves only a subset of cells out of a whole network.

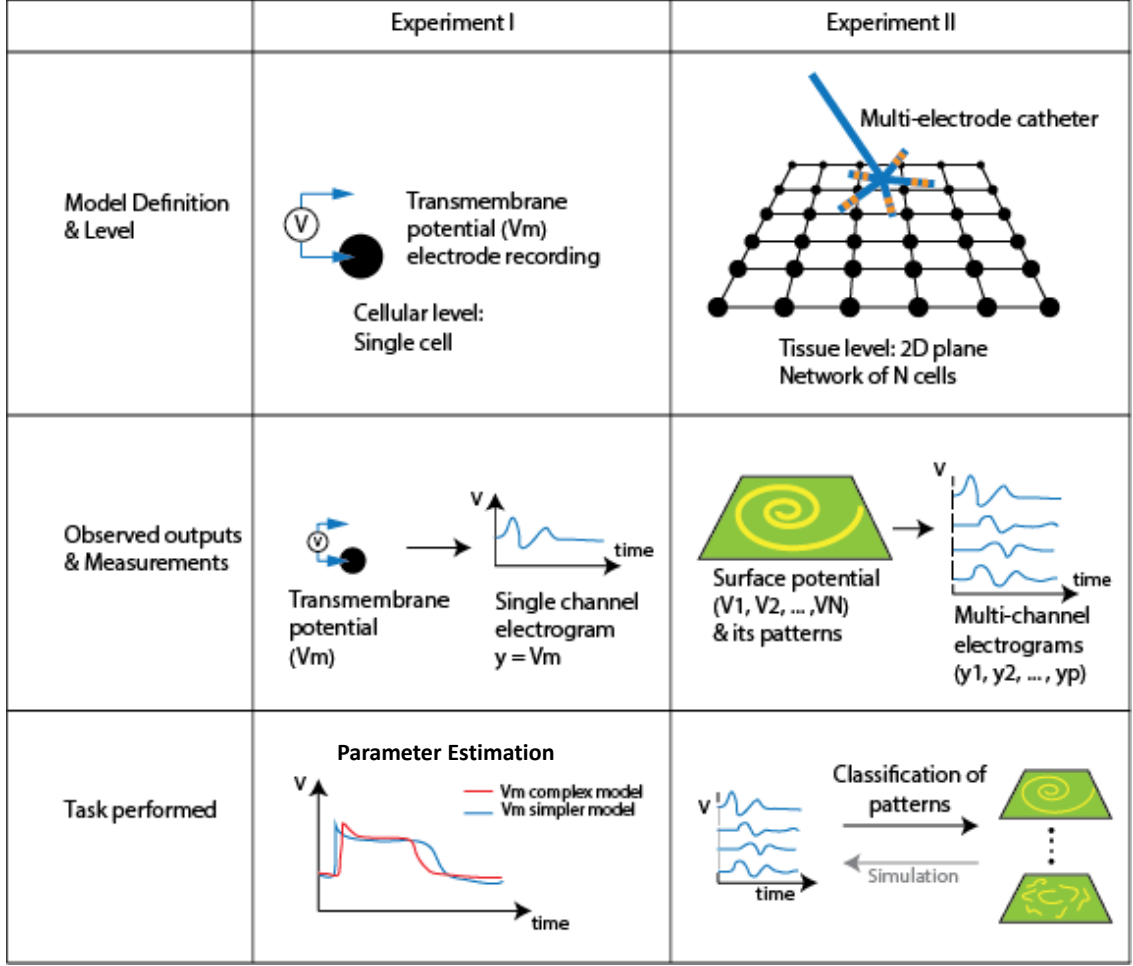


Figure 1.1: Presentation of the problems, scales, components and approaches categorized under two experiments conducted in the present thesis.

1.1 Reduced Order Modeling of Cardiac Tissue

Computer models for cardiac membrane are of great importance to understand and analyze underlying electrophysiological mechanisms of abnormality in the cardiac tissue functioning and to take therapeutic measures accordingly. Biophysically detailed models for human atria [Courtemanche et al.¹⁷; Nygren et al.¹⁹] are developed from cellular level measurements including complex interactions of ionic currents and are represented by around 25 variables. Therefore, they are computationally demanding and difficult to analyze. Phenomenological models, on the other hand, arise from reduction of biophysical details, by summarizing ionic movements as inward and outward

currents [Fenton and Karma²⁰; Mitchell and Schaeffer²¹]. They include intermediary complexity and moderate computational load with 3-4 state variables. They virtually preserve action potential (AP) morphology and arrhythmogenic characteristics. They are preferential for fast and large-scale simulation of electrophysiological dynamics of cardiac tissue, and also easier for analysis as well as computationally more tractable for optimization.

The aim in this part is then to adapt MRM [Bueno-Orovio et al.²²], a phenomenological model, to human atrial electrophysiological properties in both cellular and tissue level. In this respect, its parameters are tuned to match targeted AP and electrical restitution behaviors generated from a biophysically detailed human atrial model. Furthermore, excitation patterns on 2D tissue patch is also compared. For parameter estimation, a scheme incorporating EKF is introduced. Other optimization schemes such as sequential quadratic programming (SQP) and particle swarm optimization (PSO) are also investigated in respect to the same task. This leads to the comparison of parameter estimation schemes in adaptation performance.

1.2 Simplified Cardiodynamic Tissue Characterization

The complex nature of cardiac fibrillation makes mechanistic understanding hard to characterize. Although consensus of opinion exists on how fibrillation starts, the mechanism(s) that maintain and perpetuate fibrillation remain elusive. Spiral waves are symptoms accompanying cardiac electric rotors observed during fibrillation [Comtois et al.²³]. Studies have shown evidences for the association of spiral waves with cardiac fibrillation [Cox et al.²⁴, Davidenko et al.²⁵, Konings et al.²⁶, Gray et al.²⁷, Nash et al.²⁸, Ten Tusscher et al.²⁹, Narayan et al.³⁰, Narayan et al.³¹, Cherry and Fenton⁷]. Specifically, both stationary and meandering spiral waves which are associated with cardiac electric rotors have been observed in-vitro [Cox et al.²⁴], in-vivo [Nash et al.²⁸, Ten Tusscher et al.²⁹, Narayan et al.³⁰, Narayan et al.³¹] and rotor break-ups have been revealed through high density mapping of human right atrium [Konings et al.²⁶]. However, special tissue preparations and high density mapping is required for these processes. Also, in-silico studies uses membrane potentials, cellular level data, from the entire tissue [Kay and Gray³², Murthy et al.³³]. In this thesis, spiral waves are segregated using localized, smaller number of EGMs which are surface potentials,

standard electrophysiological data obtained with most commonly used diagnostic catheters.

Distinct wavefront propagation patterns are manifested through distinct EGMs [Konings et al.¹⁰, Wells Jr et al.³⁴]. Hence, features or quantities extracted from EGM signals [Baumert et al.³⁵] and their optimal selection [Nollo et al.³⁶] is needed in order to analyze fibrillatory patterns. Considering time varying EGM signals from multi-channels, this task becomes even more difficult. In this thesis, NCD, a similarity metric, is used which gives the distance between two objects without a need to extract features or parameters nor does it require background knowledge of the domain of the application [Cilibrasi and Vitányi³⁷]. NCD is a state of the art method and based on the computed bit lengths of data files where compression of single, pair, or multisets [Cohen and Vitányi³⁸] of data files is performed. It is demonstrated to yield successful results in diverse fields and applications [Cilibrasi and Vitányi³⁷].

The objective in this part can be summarized in three items: (1) To characterize cardiac tissue fibrillatory excitation patterns within the context of known electrical rotor behaviors observed in experimental and clinical setups and in silico. (2) To demonstrate that the most commonly used catheters providing localized readings can be used for prediction of spatially extended electrophysiological events. (3) To show that the distance measurement scheme, NCD, is a powerful and robust tool in discrimination of distinct properties manifested on a set of EGM signals without a need to extract features. In this respect, simulated spiral waves are discriminated via both clustering and classification in terms of wavefront propagation dynamics classified into stationary, meandering, and breakup. This is implemented through a set of EGMs obtained from a catheter whose type, location on the tissue and reading style as unipolar or bipolar is varied. To assess distance measures between simulated behaviors, set of EGMs as a representative of behaviors are then introduced to NCD. To demonstrate robustness of discrimination scheme, classifications for varying measurement configurations both within the same ones and between the different ones are performed. In addition, robustness of classification to noise and heterogeneous spiral behaviors on a tissue are tested.

This thesis is organized as follows: In chapter 2, background of the disease is provided including definition of Afib, epidemiology, cardiac electrophysiology, foundations of pathophysiology and

mechanism, atrial remodeling, therapy, and cardiac mapping. In chapter 3, modeling and simulation of cardiac electrophysiology is discussed. In chapter 4, methods for adaptation of MRM to human atrial electrophysiological properties are presented. In chapter 5, methods for cardiodynamic tissue characterization are presented. In chapter 6, results of adaptation of MRM to human atrial electrophysiological properties are discussed. In chapter 7, results of cardiodynamic tissue characterization are discussed. In chapter 8, the thesis is concluded.

Chapter 2: Atrial Fibrillation Background

Cardiac fibrillation is the rhythm disorder of the heart and the common cause of morbidity around the world. The two common types are Afib and ventricular fibrillation (Vfib) which are also the most complex cardiac rhythm disorder types. The former is the most common cardiac arrhythmia [Feinberg et al.³⁹] whereas the latter is one of the primer contributor to the sudden death [Zipes and Wellens⁴⁰]. Although both Afib and Vfib are considered concomitantly in many aspects, in the present context, the attributes and features which are related to Afib more are discussed.

2.1 Definition

Afib is a type of abnormal heart rhythm occurring at the upper chambers of the heart, the atria. It is the case when pacemaker activity of sinus node which results sinusoidal heart rhythm is taken over by rapid activity or activities in various regions of atria. Therefore normal heart rhythm is thrown off and instead, irregular and quivering contraction patterns arise. This chaotic, rapid atrial contraction decreases effectiveness of the heart's overall mechanical function. Furthermore, blood pumping to the brain and other organs is also deteriorated.

Afib types in terms of progressive episodes can be classified in general terms as:

- Paroxysmal Afib, called also intermittent Afib, typically equal or more than two episodes are seen and they terminate spontaneously in seven days
- Persistent Afib, sustained beyond seven days (or less). However, it does not terminate spontaneously but by pharmacology or electrical cardio-version.
- Longstanding persistent Afib, if persistent Afib goes beyond a year.
- Permanent Afib is the term used to define Afib when no methods can terminate persistent Afib.

Afib progression for a typical patient is visualized in Figure 2.1. As can be seen from the figure, the first diagnosis of the disease can take several episodes. It is worth to note that more than one of above-mentioned Afib episodes can simultaneously occur in a particular patient. Considerable amount of patients with older age and with underlying heart disease such as hypertension, coronary artery disease, heart failure, previous stroke are shown to be subject to Afib progression [de Vos et al.⁴¹].

2.1.1 Epidemiology and Prognosis

Afib is the most common chronic cardiac arrhythmia observed at 1-2 percent of the population [Feinberg et al.³⁹, Waktare⁴²], about 2.3 million people in North America and 4.5 million people in Europe Union [Go et al.⁴³]. Afib prevalence is increasing such that it is expected to double or triple within the next two to three decades [Hobbs et al.⁴⁴]. Furthermore, the number of people affected from it is expected to reach to 30 million in North America and Europe [Miyasaka et al.⁴⁵]. The incidence of Afib is also increasing where it is expected to double as the 1.2 million cases in 2010 increase to 2.6 million cases in US [Colilla et al.⁴⁶].

Afib does not cause morbidity by itself as long as it does not modify ventricular activation. However, it reduces quality of life causing lightheadedness, palpitations, and shortness of breath. Rapid beating of quivering atria for some period of time causes atrial enlargement which is called cardiomegaly [Waktare⁴²]. Both rapid beating and cardiomegaly can lead to coagulation within the atria, especially in the blind pouch atrial appendage [Waktare⁴²]. Hence, Afib increases the risk of

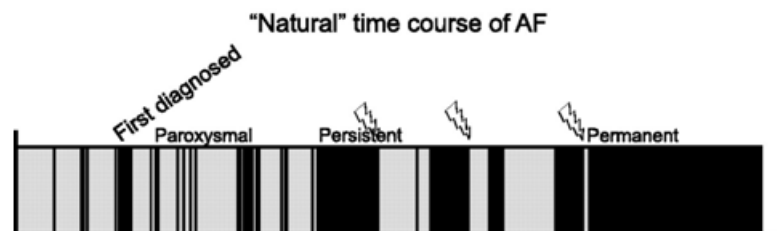


Figure 2.1: Schematic representation of natural time course of Afib progression for a typical patient. Gray areas represent the time periods where sinus rhythm and black ones represent when the . Adopted from [Schotten et al.¹]

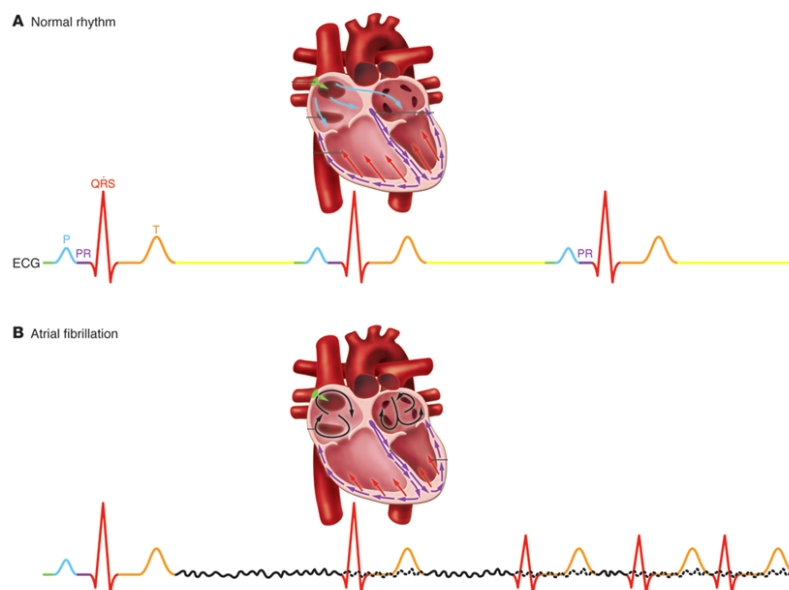


Figure 2.2: Electrophysiology of heart with (A) Normal rhythm and (B) Atrial fibrillation. Adopted from [Wakili et al.²]

stroke [Wolf et al.⁴⁷, Waktare⁴², Tsang et al.⁴⁸, Pedersen et al.⁴⁹, Knecht et al.⁵⁰]. The risk of stroke is the same in paroxysmal, permanent, and persistent Afib [Friberg et al.⁵¹].

Risk factors for Afib can be listed as hypertension, rheumatic and ischaemic heart disease, congestive heart failure, and older age. About in one-third of the cases, however, AF might be too subtle to detect earlier such that no symptoms can be seen to be aware of abnormal heart rhythm [Schmidt et al.⁵²].

2.2 Cardiac Electrophysiology

The essential function of the heart is to pump blood to various parts of the body. A synchronous contraction pattern throughout cardiac myocytes plays a crucial role for an efficient pumping. Synchronous contraction of cardiac myocytes is driven by sinusoidal propagation of electrical signals. The sinusoidal rhythm is maintained in a healthy heart as following. The sinoatrial (SA) node (also referred to as sinus node) serves as the natural pacemaker of the heart. Located in the upper area of

the right atrium, it sends the electrical impulse that triggers each heartbeat. The impulse spreads through the atria, prompting the cardiac muscle tissue to contract in a coordinated, wave-like manner. It is then propagates through the atrioventricular (AV) node, which is located in the lower portion of the right atrium. The AV node responds to the stimulation by forwarding it through the nerve network to the ventricles that initiates the same wave-like contraction of the ventricles. The electrical network surrounding the ventricles partitions through right and the left bundle branches after leaving the AV node. The impulse then propagates through the ventricular myocardium and causes the cardiac muscle tissue to contract.

Electrocardiogram (ECG) is summation of the electrical activity throughout the whole heart. The summation of electrical activity of atria results in P-wave. When it is going through AV node, there is an electrical delay. The major QRS complex is reflection of activation of ventricles while for repolarization of ventricles it is T-wave (Figure 2.2A). AF, however, is characterized by a chaotic and usually rapid activation of atria in which fibrillatory mechanisms cause continuous activation of atria. Whereas in normal functioning heart we see P-wave with discrete activation, there is continuous activation while one area is repolarizing while another area is depolarizing during AF. That results continuous summation of electrical activity on the atria and it is reflected on ECG as continuously moving baseline and rapid, irregular ventricular activity (Figure 2.2B).

Optimum heart rate for normal people varies between 60 and 80 beats per minute (bpm). In AF, however, atrial depolarization occurs at a rate of between 400 and 600 bpm [Waktare⁴²].

2.2.1 Action Potential

The action potential (AP) is a basic electrophysiological property of excitable cells such as neuron and muscle cells. It happens with a rapid rise and relatively gradual fall of membrane potential in a certain frequency. It leads to muscle contraction and stimulus propagation.

The membrane potential change that causes AP is the result of chain of activities that take place at special voltage gated ion channels. They are embedded in plasma membrane. The morphology of AP varies due to the cell type. In neuronal cells, for instance, the time between the rise and fall is rather short which takes about 1 ms and hence shape is like a spike. The cardiac muscle cells,

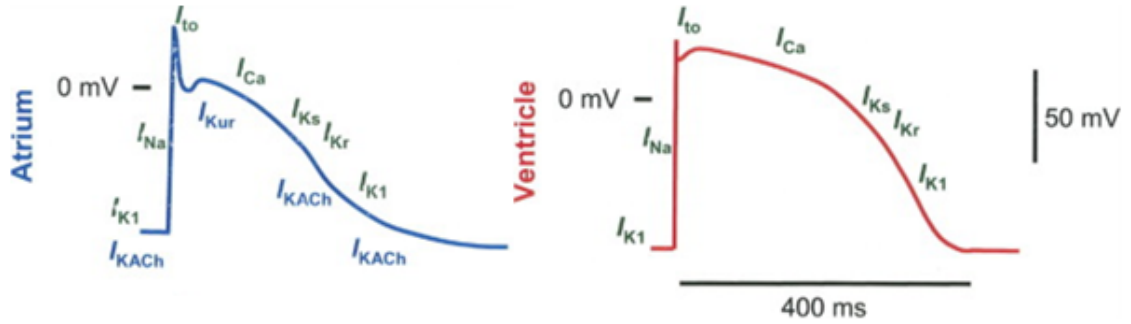


Figure 2.3: AP from human atria (on left) and ventricle (on right). Adopted from [Ehrlich et al.³]

however, have a typical AP whose duration ranges from 200 to 400 ms. Even the cardiac muscle cell AP varies in different regions of the heart. Figure 2.3 shows typical APs observed in human atrial and ventricular muscle cells.

The interactions of voltage gated ion channels follow a specific pattern for a typical AP. As can be seen from the Figure 2.3, specific ionic currents are active in respective phases of APs. Also note that different ionic currents can be observed in atrial than the ventricular muscle cells. For a typical AP, the phases are:

Phase 0 (Upstroke): Transmembrane potential increases dramatically due to voltage-gated Na^+ channels actively taking Na^+ ions inside the cell.

Phase 1 (Early repolarization): When the membrane voltage reaches to about 40 mV, voltage-gated Na^+ channels are inactivated.

Phase 2 (Plateau): Although the Na^+ permeability rapidly plummets to resting value, the membrane potential is maintained close to this level, which is a characteristic of the cardiac muscle cells, called plateau phase. This plateau is maintained by two voltage-dependent permeability changes: activation of slow L-type Ca^{2+} channels and a marked decrease in K^+ permeability in the cardiac contractile cell membrane. Atrial AP has a narrower plateau phase than ventricular AP.

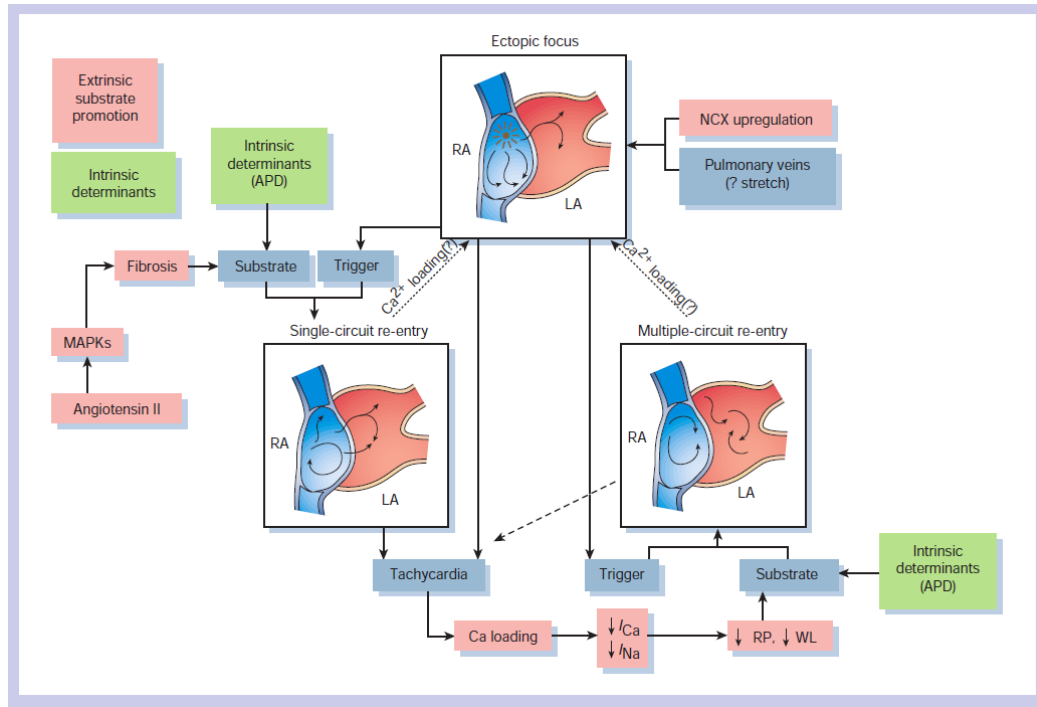


Figure 2.4: A representation of the mechanisms on different level interacting and leading to Afib. Adopted from [Nattel⁴]

Phase3 (Late repolarization): Late repolarization results from inactivation of the Ca^{2+} channels and delayed activation of voltage-gated K^+ channels. Atrial AP has more gradual repolarizing period then ventricular AP [Vigmond et al.⁵³].

Phase 4 (Resting): Resting membrane is about -85 to -95 mV and is maintained by the selective permeability of the cell membrane to various ions such as Na^+-Ca^{2+} and Na^+-K^+ ion exchangers or K^+ gradient across the cell.

2.3 Pathophysiology and Mechanism

As disorganized and chaotic as it is, in recent years there have been numerous in vivo and in vitro studies addressed to underlying pathophysiological processes, mechanisms for initiation and maintenance of Afib in order to find implications for the management. What is going on in Afib is question of a disordered physiology for a broad range of levels ranging from molecular level to the organ level, in other words, from basic mechanisms such as ion channel determinants to tissue

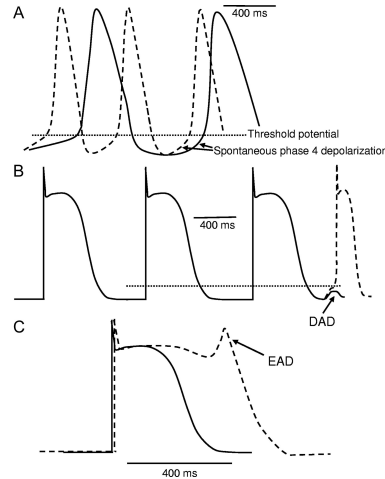


Figure 2.5: Ectopic firing mechanism at the cellular level. A) Spontaneous firing, B) Delayed afterdepolarization, and C) Early afterdepolarization. Adopted from Nattel et al.⁵

mechanisms. As depicted in Figure 2.4, complex interaction of triggers, perpetuators, and substrate leads the cardiac tissue into Afib [Nattel⁴].

2.3.1 Basic Mechanisms

The fibrillatory behavior observed at cardiac tissue is the result of more basic mechanisms which include interactions happening at the cellular level. Hence, rise of Afib pretty much depends on mechanisms of cellular level activities.

Ectopic firings, for instance, are localized abnormal impulse formations in the areas other than the SA node, the normal pacemaker of the heart. Figure 2.5 shows two ion channel related mechanisms, enhanced automaticity and afterdepolarizations, which are thought to be responsible for ectopic firings [Nattel et al.⁵].

Enhanced automaticity may be attributed to irregular interplay of depolarizing or repolarizing ionic currents during diastolic phase of action potentials (APs) of heart muscle cells (Figure 2.5 A). Inward rectifier K^+ current (I_{K1}) predominating the funny current I_f , known as pacemaker current, maintains the resting potential at normal atrial cells. Decrease in I_{K1} and overexpression of I_f breaks that balance and causes enhanced automaticity.

Afterdepolarizations are abnormal depolarization that occur at phase 2, phase 3, or phase 4 of

AP in the form of either early afterdepolarizations (EADs) or delayed afterdepolarizations (DADs). EADs is characterized by premature, abortive action potentials during phase 2 and phase 3 causing atrial AP duration (APD) prolongation due to (Figure 2.5 C). It is caused by reduced repolarizing K^+ currents and increased depolarizing inward movements of Ca^{2+} ions. DADs result from spontaneously increasing diastolic Ca^{2+} release from sarcoplasmic reticulum which interrupts late repolarization phase, phase 4, of action potential (Figure 2.5 B).

2.3.2 Tissue Mechanisms

What initiates, maintains, and perpetuates, or rather drives Afib has been interest to numerous studies, debates, and speculations for more than a century. Discussions converged to the point that the main arrhythmogenic sources of Afib are the reentries and/or rapidly firing ectopic foci (enhanced impulses).

Earlier in 1907, it was predicted that Afib might be driven by multiple firing foci [Winterberg⁵⁴]. In 1913, the circus movement theory was introduced to be responsible for the tachyarrhythmias [Mines⁵⁵, Garrey⁵⁶, Lewis et al.⁵⁷]. Circus movement theory surpassed the focus theory for a long time, until a study showed pharmacologically inducing rapidly firing foci by focally applying aconitine to the atrium would induce fibrillation in atria as well [Scherf⁵⁸]. Besides these, Moe and Abildskov in their later experimental study showed that Afib is self-sustaining provided by co-existence of randomly propagating, self-initiating multiple mother and daughter wavelet reentries independent of whatever initiating agency [Moe and Abildskov⁵⁹]. Moe and Abildskovs multiple wavelet hypothesis was confirmed by activation pattern analysis of simultaneously recorded electrograms from fibrillating canine atria [Allessie⁶⁰]. It was later confirmed on human right atrium using multi-array electrodes [Konings et al.²⁶]. However, despite being a dominant theory of how Afib is maintained for a long time, multiple wavelet hypothesis would not explain Afib initiation. On the other hand, findings from a cardiac mapping study would address the existence of rapid ectopic firings, mostly originated around pulmonary veins (PVS), which may trigger and probably maintain Afib as paroxysmal Afib is concerned [Haissaguerre et al.⁶¹]. More recent studies suggest that, in some cases, Afib can be driven by localized source(s) activated at exceedingly high frequencies in

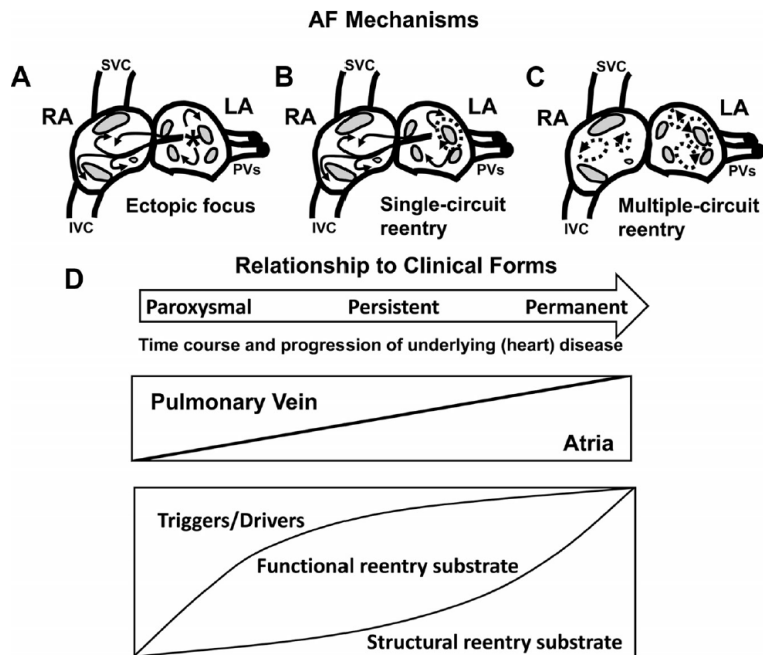


Figure 2.6: Schematic representation of generally accepted mechanisms of Afib. (A) Ectopic foci causing discordant propagation, (B) Single-circuit reentry generally around a conduction block, (C) Multiple-circuit reentry, (D) Relationship between Afib patterns, mechanisms, and remodeling. Adopted from Iwasaki et al.⁶

the form of reentries [Skanes et al.⁶², Mandapati et al.⁶³, Mansour et al.⁶⁴, Vaquero et al.⁶⁵] or focal impulses [Sahadevan et al.⁶⁶]. This phenomena is also called "mother rotor theory".

In the light of the findings to date, a generalization can be drawn as to represent the principal tissue level mechanisms responsible for Afib (Figure 2.6 A-C). Those can be listed as:

- Ectopic focus
- Single-circuit reentry
- Multiple circuit reentry

The relationship between Afib types in clinical terms and presumed Afib mechanisms are shown in Figure 2.6 A-C). Afib often starts out with paroxysmal Afib and the mechanisms are somewhat simpler at this stage. It usually has ectopic foci as a sole driving factor for Afib. So it is the ectopic firings most of which occur in the region of PVs which can be classified as triggers, or sort

of drivers, as far as the problem is what perpetuates Afib. As Afib progresses, however, there are more structural changes to the atrium and from this point forward it is easier to have Afib and the circuits become more complex. It may no longer be only ectopic foci but also reentry of circuits within the atria can be present. And it progresses from being paroxysmal or being in and out of Afib to going into and staying in Afib or what is called persistent Afib. Therefore, it is no longer a PV problem only but there is also the change in atrial tissue that perpetuates Afib. And at this stage the elements that can be classified as functional and structural or substrate that keeps the Afib going are not just atrial triggers. And as Afib keeps going for longer periods from within classified as permanent or long-standing Afib where it is not just one circuit but multiple circuits or multiple mechanisms retaining the Afib in which case it may just be mostly driven by mechanisms within the left atrium body and as Afib keeps going there may be additional structural changes of atrial body itself that further perpetuate Afib.

This is a somewhat commonly agreed series of events happening during Afib [Calkins et al.⁸]. But there are still many unknowns. It is probable that there can exist foci within PV that is driving Afib where there is less of atrial problem but as there is additional structural changes in atrial myocardium such as further dilation of the atrium scarring [Zipes⁶⁷, Okishige et al.⁶⁸], it is easier to have circuits within the atria. Then it probably progresses from having single circuits to multiple circuits that really keep Afib from ever terminating spontaneously. These circuits may manifest themselves in the form of a macro reentry involved in large areas or may be what looks like an ectopic focus or sort of focal mechanism. Although there are still many unknowns about the mechanisms of Afib, a remarkable observation is that reentries are byproducts of fibrillatory mechanism. In the following section, a more detailed discussion of reentry mechanisms where there is a delineation on the electroanatomical factors and features that contribute to reentries is provided.

Reentry Mechanisms

As discussed thus far, chaotic nature of fibrillation together with the multiplicity of factors behind it makes understanding the cause or causes of cardiac arrhythmias. However, despite the fact that the mechanisms maintaining Afib is not yet clear, many studies have shown the role of electrical

rotors or reentries during cardiac fibrillation [Cox et al.²⁴, Davidenko et al.²⁵, Konings et al.²⁶, Gray et al.²⁷, Cherry and Fenton⁷, Ikeda et al.⁶⁹, Nash et al.²⁸]. Hence, insight into the cardiac wave dynamics can provide more clues to understand fibrillatory mechanisms and identify the driving factors. As mentioned in tissue mechanisms section, observations from electro-anatomical mapping studies have been linked to different paradigm of reentry mechanisms which can be listed as circus movement theory, leading circle concept, spiral wave reentry, multiple wavelet theory, and mother rotor theory.

Circus Movement Reentry: Circus movement reentry, also called anatomical reentry, is characterized by pinning of subsequent activation patterns around a preformed anatomical structure where there is a conductional block. The important factor for circus movement reentry keeps going is that there is an excitable area between head and tail of the reentry. This is also called as 'excitable gap'. This gap arises if path of the circuit is longer than the wavelength (WL) of circus movement. A WL can be calculated as:

$$WL = RP \times CV \quad (2.1)$$

where RP is the refractory period and CV is the conduction velocity. Because the WL is short enough to allow an excitable gap, a slow conduction and a short refractory period are underlying factors which lead to circus movement reentry. Having so many electrically not active anatomical structures such as cavo-tricuspid isthmus, valve annuli, blood vessels, atria are quite favorable to predispose the reentry. Atrial anatomical reentry, also known as atrial flutter (AFL), has been of clinical interest since the earlier times [Mines⁵⁵, Garrey⁵⁶, Lewis et al.⁵⁷].

Leading Circle Concept: Allesie et al. showed in rabbit left atrium that a rotating reentry can take place without an anatomical obstacle [?]. Hence, unlike circus movement reentry, leading circle concept does not include anatomical obstacle while the reentry follows the minimal possible loop and therefore very small excitable gap. Similar to circus movement reentry, the underlying parameters are cellular refractoriness and conduction velocity and the balance between them. Another significant

component for maintenance of the reentry is centripetal wavelets moving towards the center and keeping there in a permanent state of refractoriness which is also called electro-tonic depolarization, a functional block.

Spiral Wave Reentry: According to spiral wave theory, the wavefront is like a spiral rotating around a core (centre). The core is a fully polarized bounded circular region where electrotonic effect arises. That renders the core as a current sink which shortens the APD in the surrounding region. As the falling side of the wave just gets active, twisting occurs towards that region. That interaction maintains the spiral wave. The core represents phase singularity. Unlike leading circle concept, the centre is excitable but not excited. Both leading circle concept and spiral wave together are the type of functional re-entry. In fact, they are competing concepts for the explanation of cardiac wave reentries. Clinical and experimental observations from recent studies favor spiral wave over leading circle concept suggesting that it is more consistent with biophysical properties like electrotonicity, source -sink relation, and dynamics around the core [Comtois et al.²³]. Observations from chemical reactions in excitable media provides a more theoretical and intuitive basis for spiral wave theory [Kapral and Showalter⁷⁰, Swinney and Krinsky⁷¹]. Hence, results from computer simulation (in-silico) studies favor the spiral wave re-entry. In fact, other re-entry mechanisms such as circus movement, multiple wavelet, and mother rotor can also be explained by spiral waves if appropriate parameterization and stimulus protocol is implemented.

Multiple Wavelet Theory: For a long time dominant theory of Afib has been the multiple wavelet theory. The reentry mechanism here involves break up of wave fronts along the propagation through the atrial tissue and causing multiple self-sustaining daughter reentries [Moe and Abildskov⁵⁹]. The essential factors behind this mechanism is the refractory period, tissue mass, and conduction velocity. Namely, the critical number of wavelets sustaining the arrhythmia depends on the shortened enough cycle lengths of the wavelets and sufficiently large atrium. It has been verified in vivo in humans using simultaneous recordings from multiple electrodes [Cox et al.²⁴]. It also corresponds to spiral wave breakup derived from in-silico studies.

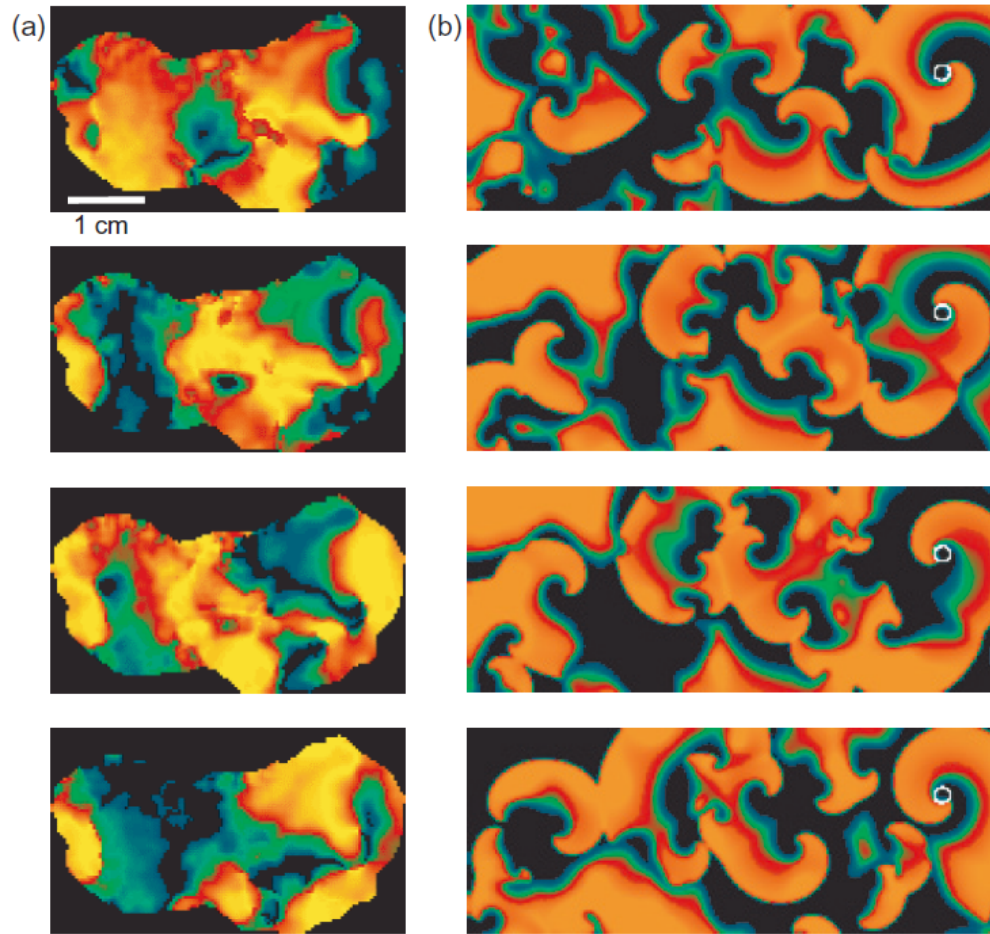


Figure 2.7: Mother rotor observed in an experimental setup (a) and simulation (b). Adopted from [Cherry and Fenton⁷]

Mother Rotor Theory: Another fibrillatory mechanism including reentry formation is mother rotor theory in which a mother rotor of continuous activity is sustained and sheds daughter rotors [Davidenko et al.²⁵, Chen et al.⁷², Jalife et al.⁷³, Ideker and Rogers⁷⁴, Vaquero et al.⁶⁵] (see 2.7). Whereas multiple wavelets do not require it for self-sustaining dynamics of wave breaks, electrophysiological heterogeneity which prevents 1:1 conduction between the areas of mother and daughter rotors maintains the activity in mother rotor theory. Typically, mother rotor is stable and has a longer refractory period than daughter rotors do have. Potentially extinguishing the mother rotor may destabilize the fibrillatory process and may allow returning to the sinus rhythm.

2.4 Atrial Remodeling

In this section we will cover the phenomena called atrial remodeling observed during AF which is highly correlated with AF mechanism. There is interdependence between atrial remodeling and maintenance of AF [Wijffels et al.⁷⁵]. That is, atrial remodeling can be caused by the AF itself or concomitant (underlying) heart disease while atrial remodeling promotes increasing propensity to AF. It can be classified as electrical remodeling and structural remodeling. They incorporate into AF initiation and perpetuation both individually and mutually. For instance, as electrical remodeling shortens APD and structural remodeling causes slow conduction, they both decrease the wavelength that incorporates into reentry. Krogh-Madsen et al.⁷⁶ showed in their atrial simulation study that their effect can differ when more comprehensive dynamics are considered. They specifically showed that maximal number of filaments, wave fragmentation, restitution properties, and whether dominant waves are anchored to anatomical obstacles or meandering freely differs in case of electrical and structural remodeling.

2.4.1 Electrical Remodeling

The detail of mechanism behind electrical remodeling is covered in Section 2.3.1 on cellular level. It is basically characterized by alterations in ion channel functions resulting progressive shortening of effective refractory periods and therefore reduced wavelengths that potentially increase the vulnerability and presumably stability of arrhythmia [Wijffels et al.⁷⁵, Morillo et al.⁷⁷, Rensma et al.⁷⁸, Allessie⁷⁹]. In this respect, it is virtually associated with 'triggers' of AF henceforth with initiation of arrhythmia. Interdependency between atrial electrical remodeling and repeated episodes of AF was shown to be different [Garratt et al.⁸⁰]. In that study, the data suggested that initial AF episodes would cause certain electrical remodeling and returning back to sinus rhythm was adequate to reverse all abnormalities. However, repetitive AF episodes afterwards would not lead to further electrical remodeling. Another study, in addition, showed that repetitive cardioversions would not prevent AF progression [Fynn et al.⁸¹]. These findings have brought up the idea of 'second factor' in progression and development of AF [Garratt et al.⁸⁰].

The 'second factor' was then attempted to be identified in a comparison study between patients with paroxysmal lone AF and patients with another arrhythmia, atrioventricular tachycardia with left-sided accessory pathways and no history of AF and no risk factors for AF [Stiles et al.⁸²]. They looked at each group in detail and showed that patients with paroxysmal lone AF have larger atrium, slower conduction across the atrium leading to longer total activation time of both atria, more areas of fractionated electrogram, and lower overall voltage.

2.4.2 Structural Remodeling

As pointed before, atrial structural modeling is involved in 'second factor' in the development of sustained AF. There are basically two types of cells in cardiac tissue: electrically active muscular cells and fibrosis that are electrically not active but can cause slow conduction. Hence, the main component of structural remodeling is fibrotic tissue which is associated with 'substrate' of AF and hence perpetuation of arrhythmia. Fibrosis, in general, can be characterized by inflammation, scarring or any damage to tissue resulting extracellular matrix deposition which is typically collagen production and accumulation [Bishop⁸³, Burstein and Nattel⁸⁴]. Remarkably, however, a study revealed that atrial fibrosis increases by solely age [Gramley et al.⁸⁵]. The estimation suggests that every year a person is alive, 1 percent of the atrium turns into fibrosis. That rate can increase based on having multiple risk factors such as hypertension, diabetes or being a smoker. Furthermore, reduction of atrial contractility and consequently atrial dilatation contribute further to structural changes that fuel persistence of AF [Allessie et al.⁸⁶].

2.5 Treatment Options

As Afib is a progressive disease with broad range of mechanisms, therapeutic strategies differ depending on where a patient stands. Figure 2.8 shows therapeutic options for Afib. Upstream therapy is anything preventing development of Afib substrate. It aims at interference in structural remodeling of myocardium associated with hypertension and heart failure. We can list some upstream therapy methods as using angiotensin converting enzyme (ACE) inhibitors to treat high blood pressure, using statin to lower cholesterol, using glucocorticoids as an anti-inflammatory, omega-3 fatty

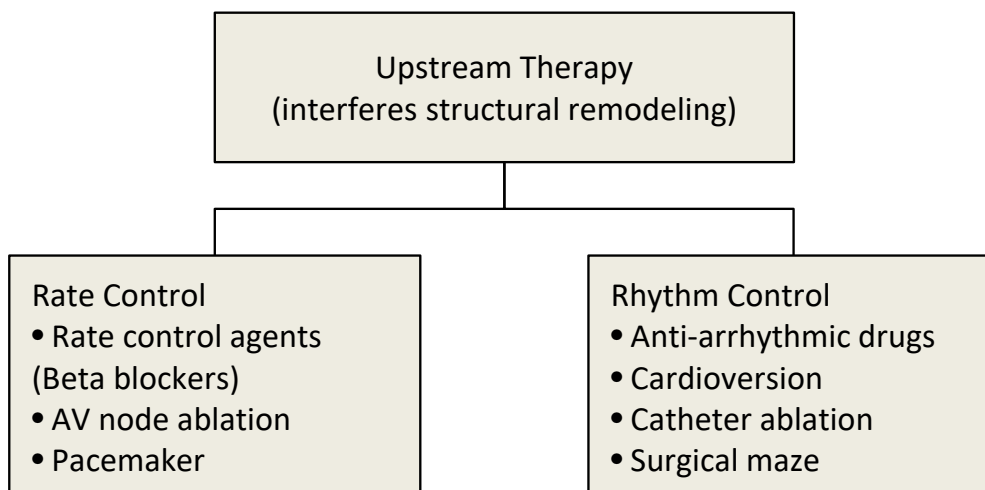


Figure 2.8: Therapeutic flow diagram for Afib.

acids, or moderate physical activity. Once you develop Afib then it is no longer upstream therapy but therapy. As long as therapy is concerned, therapeutic decision depends on achieving rate control and/or rhythm control. Rhythm control is considered more often for patients with paroxysmal Afib whereas rate control is an option mostly for patients with chronic Afib.

2.5.1 Rate and Rhythm Control

Rate control typically aims at lowering the heart rate to normal which is around 60-100 bpm. It also means staying in Afib or not specifically treating the rhythm because it virtually regulates the ventricular rate response. Hence, rate control is slowing down the heart beat but not necessarily converting to the rhythm. In general, beta blockers reduce the heart rate. Sometimes, however, drugs are not adequate to slow down the heart. Hence, AV node ablation and a pacemaker placement may be needed to control the heart rate.

The objective in rhythm control is to bring the heart to sinus rhythm. Restoration to sinus rhythm is usually performed via cardio-version. Maintenance of sinus rhythm, on the other hand, is done with anti-arrhythmic drugs. Anti-arrhythmic drugs target at suppressing ectopic activity such as enhanced automaticity or delayed or afterdepolarizations. In addition, reentries can be suppressed by basically increasing the refractory period. That requires single or multiple ion channel blockage.

Traditional antiarrhythmic drugs inhibit single currents such as Na^+ currents with class I agents that suppress ectopic activity, Ca^{2+} currents with class II agents, and K^+ currents with class III agents that suppress reentry by increasing refractory period. Favourable antiarrhythmic drugs, on the other hand, block multiple channels such as Na^+ , Ca^{2+} , and K^+ currents with amiodarone.

In theory, rhythm control is expected to be superior to rate control. However, a multitude of randomized, multi-centered studies examining the both strategies have not yet found the advantage of rhythm over rate control in terms of better survival, improvements of symptoms and quality of life (Hohnloser et al.⁸⁷, Van Gelder et al.⁸⁸, Wyse et al.⁸⁹, Carlsson et al.⁹⁰). However, on-treatment AfibFIRM study reported that the presence of sinus rhythm would significantly decrease the mortality while using antiarrhythmic drugs would increase it [Investigators et al.⁹¹]. This is mainly due to inadequacy of antiarrhythmic drugs as a sole mean to maintain sinus rhythm [Calkins et al.⁸]. Pharmacological rhythm control which mostly reverses electrical remodeling is not an efficient treatment strategy with limitations such as life-threatening ventricular proarrhythmia and extracardiac toxicity [Nattel and Carlsson⁹², Nattel and Opie⁹³]. Besides, reversing electrical remodeling would not be adequate whence structural remodeling is not yet suppressed [Cosio et al.⁹⁴]. Hence, catheter ablation, a non-pharmacological therapy, has been taken over as an alternative treatment of Afib over the past 15 years.

2.5.2 Catheter Ablation

Catheter ablation has been an improving strategy for termination of Afib. It is a procedure aiming at elimination of arrhythmogenic agents by delivering radiofrequency (RF) or cryo-energy to the heart tissue. As the first evidence that paroxysmal Afib can initiate from ectopic beats originating from the orifice or myocardial sleeve inside the PVs was provided [Jai et al.⁹⁵, Haissaguerre et al.⁶¹], discrete elimination of these foci by radiofrequency (RF) ablation has been reported to be effective in preventing recurrence of Afib [Jai et al.⁹⁵, Haissaguerre et al.⁶¹, Chen et al.⁹⁶]. However, due to limited topographical accessibility of PVs, several limitations were comprised with focal ablation in the long term. Hence, PV isolation (PVI), isolation of the triggering source from the left atrium via segmental or complete lines of block at PVs ostia was suggested to be the new and standard

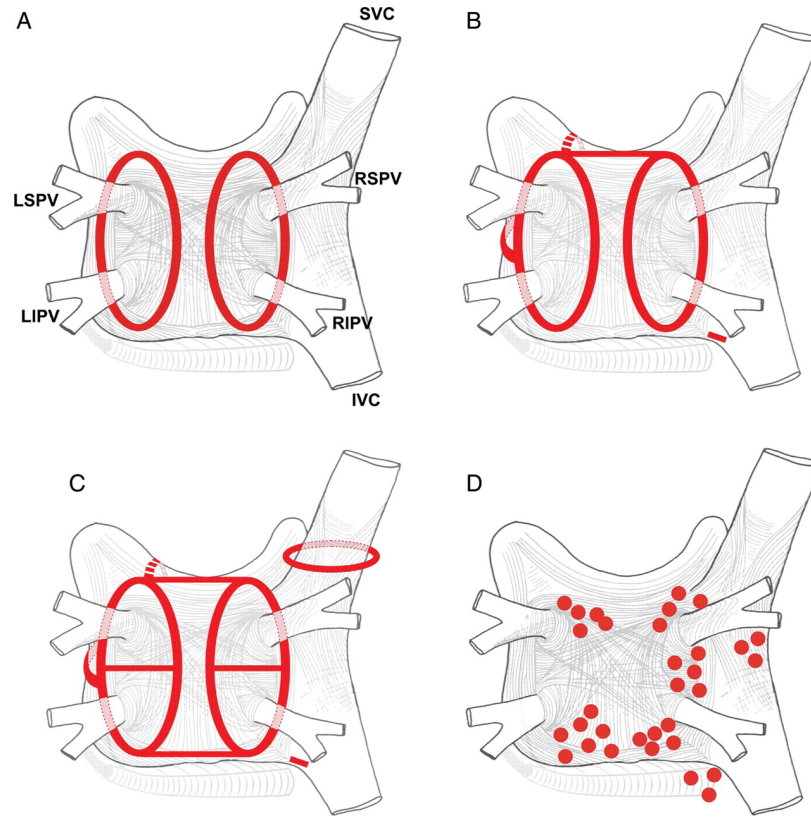


Figure 2.9: Afib ablation strategies. Adopted from Calkins et al.⁸.

ablation strategy [Haïssaguerre et al.⁹⁷].

Although elimination of ectopic firings as the 'triggers' works well in paroxysms of Afib, it is not adequate for progressive episodes such as persistent Afib Calkins et al.⁸. By recent advancement in cardiac electro-anatomical mapping technologies, regions which are thought to be 'substrates' or 'perpetuator' of Afib were also targeted as potential ablation endpoints [Haïssaguerre et al.⁹⁸]. In order to detect those sites, multi-electrode, simultaneous mapping covering many areas of the heart was required. Nevertheless, using high density intra-operative mapping it was demonstrated that complex fractionated electrograms (CFAEs) are associated with distinct electrophysiological properties of 'substrate', such as functional block, slow conduction and/or pivot points where wavelets turn around at the end of the arcs of functional blocks [Konings et al.²⁶]. Thus, such areas of CFAEs during Afib represent either continuous reentry of the fibrillation waves into the same area or overlap of different wavelets entering the same area at different times [Konings et al.¹⁰]. Such

complex electrical activity has a relatively short cycle length and heterogeneous temporal and spatial distribution in humans [Gerstenfeld et al.⁹⁹, Jais et al.¹⁰⁰]. Furthermore, it was demonstrated in a mapping study of induced Afib in dogs that cryoablation at the sites of the shortest atrial fibrillation cycle length led to termination and non-inducibility of Afib [Morillo et al.⁷⁷]. According to these observations, Nademanee et al. reported an approach for catheter ablation of Afib in humans, targeting sites of CFAEs [Nademanee et al.¹⁰¹]. However, mechanisms favoring the genesis of CFAEs are not well defined in human Afib. It is still unclear whether these sites are 'perpetuator' or a spot in the wavelet or in the collision of wavelets.

In summary, in the light of ablative experiences to the date, the ablation strategies can be listed as elimination of:

- Triggers
- Substrates
- Triggers and substrates

What type of ablation strategy needed to take virtually depends on the patient's specific condition such as progression in Afib. Still, the identification of 'substrates' needs further understanding and interpretation of clinical data and that requires high quality and informative measurements taken from the patient. In this sense, a discussion on cardiac electro-anatomical mapping follows in the next section.

2.6 Cardiac Electroanatomical Mapping

The studies revealed AF mechanism discussed previously (see Section 2.3] use invasive methods such as intra-thoracic surgery. For instance, Allesie et al. had to perform epicardial mapping in order to reveal wave patterns in both RA and LA surface [Allesie et al.¹⁰²]. They placed 244 electrodes after median sternotomy which is the incisions made in thorax to obtain a wide view of thoracic cavity and cardiopulmonary bypass procedures. But this is impractical in case of ablative treatment of AF which is a prevalent technique. Instead, cardiac catheterization, a procedure involved delivering

a thin, flexible, and hollow tube called a catheter into heart through a large blood vessel, is used. The catheter is usually inserted from groin, neck or arm and threaded through artery or vein. It is usually a very safe procedure with several minor complications.

Besides ablation, cardiac catheterization also involves diagnostic measurements such as collecting blood samples, measuring pressure, oxygen content and the blood flow in various chambers of the heart. But more importantly it provides information on electroanatomical state of heart tissue. Diagnostic findings and testings through cardiac catheterization is more clear than non-invasive methods as ECG, chest x-ray, echocardiogram, and exercise test.

2.6.1 Mapping Tools

Mapping tools basically provide electrophysiological, anatomical, and geometrical information of the heart. Endocardial tissue voltages, or the electrograms, is measured through the electrode probes that contact surface of the tissue. Today, different mapping tools are used in the electrophysiology labs. We can categorize them as multisite and local recording catheters.

Multisite mapping catheters are rather widely sampled providing a higher resolution. They constitute around 64 electrodes and allows for a simultaneous recording of endocardium electrical activity. An example is a basket catheter such as Constellation (Boston Scientific, Natick) with the array of 64 electrodes where 8 splines each constituting of 8 electrodes with 2-3 mm spacing (Figure 2.10 C). They are expensive and not commonly used in electrophysiology labs. Also ensuring the contact of the electrodes to the tissue is hard.

The most commonly used tools provide spatially local recordings with 10-20 electrodes and a diameter of 15-25 mm. The distance between neighboring electrodes is usually 2 mm. The shapes of the catheters in general are circular such as Lasso (Biosense Webster, Diamond Bar) (Figure 2.10 B) and Optima (St. Jude Medical, St. Paul) or spiral such as AFocus II (St. Jude Medical, St. Paul) (Figure 2.10 A) or five-arm such as PentaRay (Biosense Webster, Diamond Bar). There is also monophasic action potential (MAP) catheters (EPT, Sunnyvale, CA, USA).

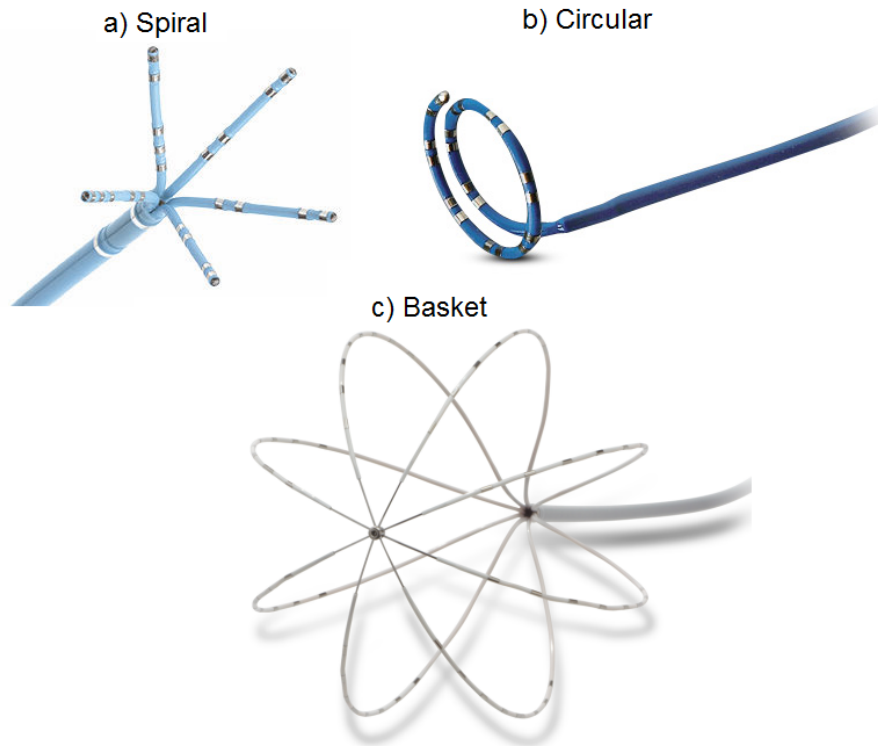


Figure 2.10: Cardiac mapping tools used commonly in AF therapy.

2.6.2 Computational Mapping Techniques

With the improvement of mapping technologies, computational techniques are concurrently employed to reveal electrical activity in atrial tissue. Innovative signal and image processing techniques are employed to obtain electrogram-derived anatomical maps and quantified parameters.

The signal obtained from the mapping is called electrogram which can be classified as a time series data. A time series data can be periodic or aperiodic depending on how much rate and regularity exist in the data. Three basic characteristics can be considered as constituents of an electrogram:

- i. Amplitude: It reflects the change of intensity of the signal which is extracellular potential in cardiac electrophysiology.
- ii. Frequency: It includes periodicity and repetitiveness information of numeric values in the time series data.

- iii. Phase: It represents respective changes on a signal within one waveform cycle divided into 2π radians.

The approach that uses phase information of recorded electrograms was introduced in [Winfree¹⁰³] that would lead to pivot point detection of reentrant circuits using phase singularities [Gray et al.²⁷]. In detail, phase-space plots represent temporal organization and phase maps represent the spatial organization. Using the time delay representation of electrograms to construct phase space which is also known as time delay embedding requires careful selection of time delay constant for an accurate phase estimation. Hilbert transform was proposed as a more robust approach that enables instantaneous phase of electrograms [Bray and Wikswo¹⁰⁴]. For the identification of phase singularities, convolution kernel is used [Bray and Wikswo¹⁰⁵].

Narayan et al. performed computational mapping of electrical rotors in human atria using 64 pole basket catheter [Narayan et al.³⁰, Narayan et al.⁹, Narayan and Briggs¹⁰⁶]. They reconstruct activation time onsets directly from the electrodes therefore isochronal maps and isopotential movies where electrophysiological validation was done through a deflectable MAP catheter. In another study they show that the similar AF activation can be obtained either directly from electrograms or using phase analysis method [Narayan et al.¹⁰⁷]. They also detect center of the rotational source [Macneil and Sehra¹⁰⁸]. Figure 2.11 shows a resulting rotor mapping from the FIRM study.

Evaluation of Arrhythmic Features

Besides mapping the electrophysiological activity of cardiac tissue, additional parameters are derived from measured electrograms. Various parameters are extracted such as local activation time, wave direction, and conduction velocity.

Using frequency domain analysis methods, parameters to characterize AF rate and organization are computed. Dominant frequency [Skane et al.⁶², Berenfeld et al.¹⁰⁹] is the frequency with highest magnitude in the FFT spectrum of electrogram. Organization index [Everett et al.¹¹⁰] is defined as the ratio of area of the dominant peak and its harmonics to the total area of the magnitude spectrum. Peak area ratio, the area ratio of the DF to the encompassing envelope at a certain frequency, is assessed to measure cycle-to-cycle regularity of electrograms [Narayan et al.¹¹¹,

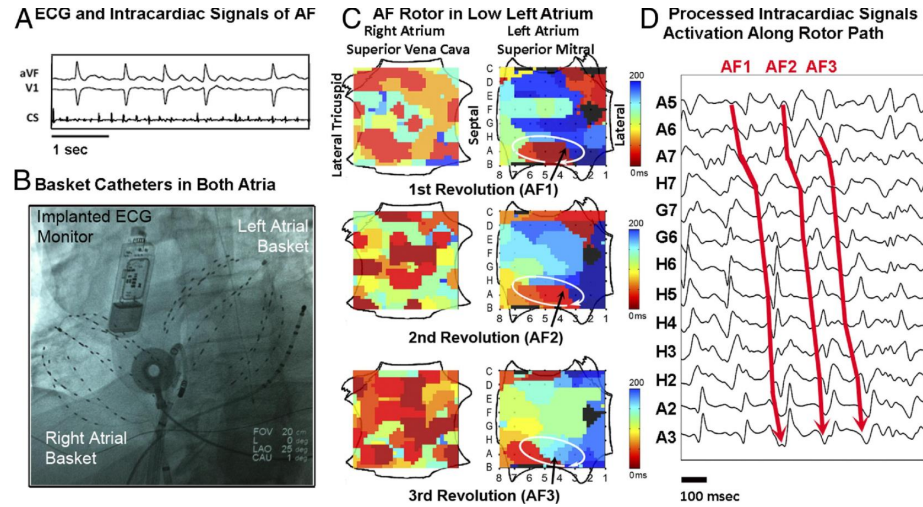


Figure 2.11: The setup for the computational mapping of electrical rotors during AF from FIRM study group. A) Intracardiac Electrograms B) Monitoring 64-pole basket catheter replacement in both atria using fluoroscopy C) Isochronal maps computed through activation times reveal the rotors 3 consecutive revolution in both left and right atria. D) Respective activation times captured from the filtered ECG signals represented. Adopted from Narayan et al.⁹

Krummen et al.¹¹²].

Several other studies reported extraction of further features such as wave direction [Weber et al.¹¹³], regularity index that detects repetitiveness of the activations on a beat-to-beat basis and indicates temporal and spatial changes in fibrillatory organization [Faes et al.¹¹⁴], APD [Narayan et al.¹¹⁵, Narayan et al.¹¹⁶] and conduction velocity restitution [Lalani et al.¹¹⁷, Weber et al.¹¹⁸] are also quantified to assess the features related to activation patterns.

Electrogram Characterization Methods

During recording, underlying electrophysiological activity reflects on the genesis of intracardiac electrograms. Hence, distinct arrhythmia organization and henceforth cardiac tissue activation patterns manifest distinct unipolar or bipolar electrograms [Wells Jr et al.³⁴, Konings et al.¹⁰]. Wells subjectively classified bipolar atrial electrograms measured on epicardium following open heart surgery in 34 patients based on their morphologies and the nature of their isoelectric baselines into four AF types [Wells Jr et al.³⁴].

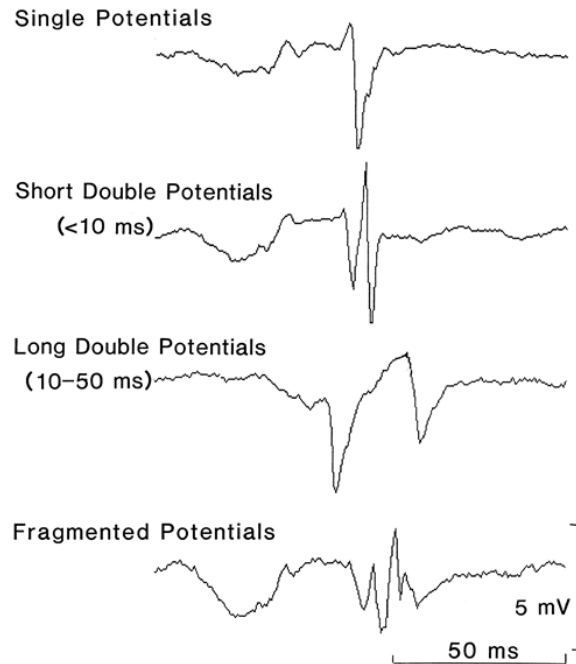


Figure 2.12: Characterization of unipolar electrograms from [Konings et al.¹⁰]

- i. Type I: Characterized with discrete manifestation of electrogram spikes and perturbation-free isoelectric baseline.
- ii. Type II: Characterized with discrete manifestation of electrogram spikes but isoelectric baseline is with perturbations.
- iii. Type III: Shows no discrete manifestation of electrogram spikes and isoelectric baseline is with perturbations.
- iv. Type IV: Includes alternation between Type III on one side and Type I and Type II on the other side.

Konings et al. [Konings et al.¹⁰] classified unipolar atrial electrograms into four categories on the basis of their morphology (Figure 2.12). The classified electrograms:

- Single potentials: Characterized with a large single negative deflection.
- Short-double potentials: Characterized with two negative deflections between which the time interval is less than 10 ms.

- Long double potentials: Characterized with two negative deflections between which the time interval is more than 10 ms.
- Fractionated electrograms: Characterized with multiple negative deflections.

A template matching technique has been used for automatic characterization of unipolar human AF electrograms obtained from multielectrode epicardial data and matched with a library of mathematically constructed unipolar electrogram templates where fractionated electrograms were excluded that led to activation time detection and hence mapping of AF [Houben et al.¹¹⁹]. In their following studies they also include fractionated electrograms which were analyzed using wavelet decomposition technique [Houben and Allesie¹²⁰, Houben et al.¹²¹]. In a simulation study electrogram morphology was shown to reflect the wavefront propagation pattern and anisotropy in the tissue [Jacquemet et al.¹²²]. Nollo et al introduced a scheme that does AF type characterization based on Wells criteria through automatic classification of atrial electrograms using Jeffries - Matusita distance [Nollo et al.³⁶].

Chapter 3: Cardiac Electrophysiology Simulation

Cardiac electrical activity can be modeled and simulated for a single cell, a cable or a 2D or 3D tissue geometry. In this chapter, modeling basic cardiac electrophysiology is covered first. Then, using models to compute restitution properties are discussed. Finally, numerical methods used in the simulations are discussed.

3.1 Modeling Cardiac Electrophysiology

Computer models can be used to analyze principles and mechanisms of cardiac electrophysiological events and support the therapeutic decision making. Modeling electrophysiology of heart simply follows the dynamics of trans-membrane potential of cardiac cells. Cardiac cells are excitable thereby a sufficient electrical current stimulus can trigger a coordinated interaction of electrogenic constituents such as ionic currents through membrane channels, pumps and ion exchangers. A detailed representation of the electrogenic elements for a human atrial myocyte are given in Figure 3.1 [Courtemanche et al.¹¹]. Therefore, modeling the dynamics of those interactions result in AP which is overall trans-membrane potential of the cell. The dynamics and inherent properties can differ for different regions of the heart and for different species therefore resulting AP for each case can be different. This is illustrated in Figure 3.2.

3.1.1 Human Cardiac Models

Today, aside from the models for animal hearts, a number of published models of human cardiac electrical activity which are based on principles of reaction diffusion systems exist [Sachse¹²³]. Based on complexity, intuitiveness, and capacity to represent molecular and tissue level characteristics, cardiac computer models can be classified as biophysical, phenomenological, and generic models.

Biophysical Models: These models are biophysically detailed including complex interactions of ionic currents and are based on the work of Hodgkin and Huxley [Hodgkin and Huxley¹²⁴].

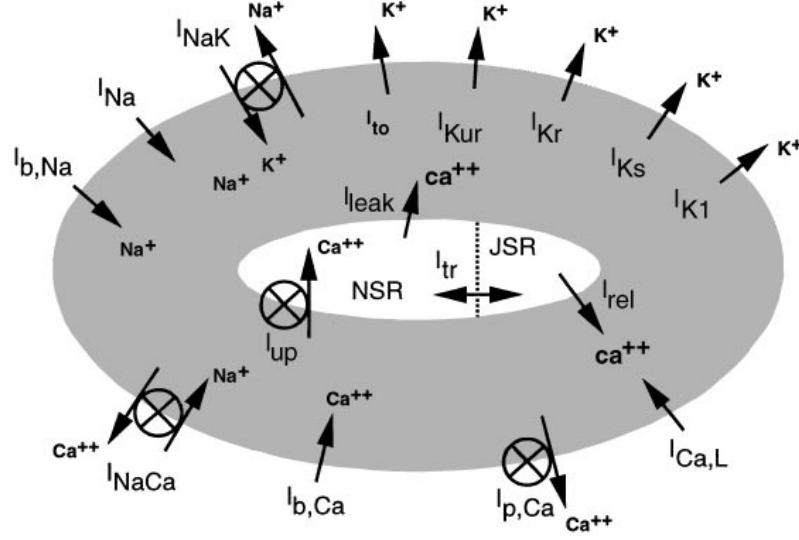


Figure 3.1: Schematic representation of cellular components such as ionic currents, pumps and ion exchangers. The interactions happen between 3 mediums: myoplasm, junctional sarcoplasmic reticulum (JSR) and network sarcoplasmic reticulum (NSR). Adopted from Courtemanche et al.¹¹

They include around 60 variables. That causes serious limitations in computational efficiency and in exhibiting all cardiac tissue characteristics and dynamics. Also, their ionic formulations are really complex hence they are not easy to analyze. BMs exist for human atrial membrane [Nygren et al.¹⁹, Courtemanche et al.¹¹] or human ventricular membrane [Beeler and Reuter¹²⁵, Priebe and Beuckelmann¹²⁶, Bernus et al.¹²⁷, Ten Tusscher et al.¹²⁸, Iyer et al.¹²⁹].

Phenomenological Models: They arise from reduction of biophysical details which are basically summarized ionic movements as inward and outward [Fenton and Karma²⁰, Mitchell and Schaeffer²¹]. They include intermediary complexity with only 3-4 variables thereby moderate computational load yet significantly faster comparing biophysical models. They virtually preserve AP morphology and arrhythmogenic characteristics.

Generic Models: The models in this class are derived from generic excitable media dynamics implementing wave propagation [FitzHugh¹³⁰, Hodgkin and Huxley¹²⁴]. Although they are efficient in computation, they are significantly limited in reproducing important electrophysiological properties.

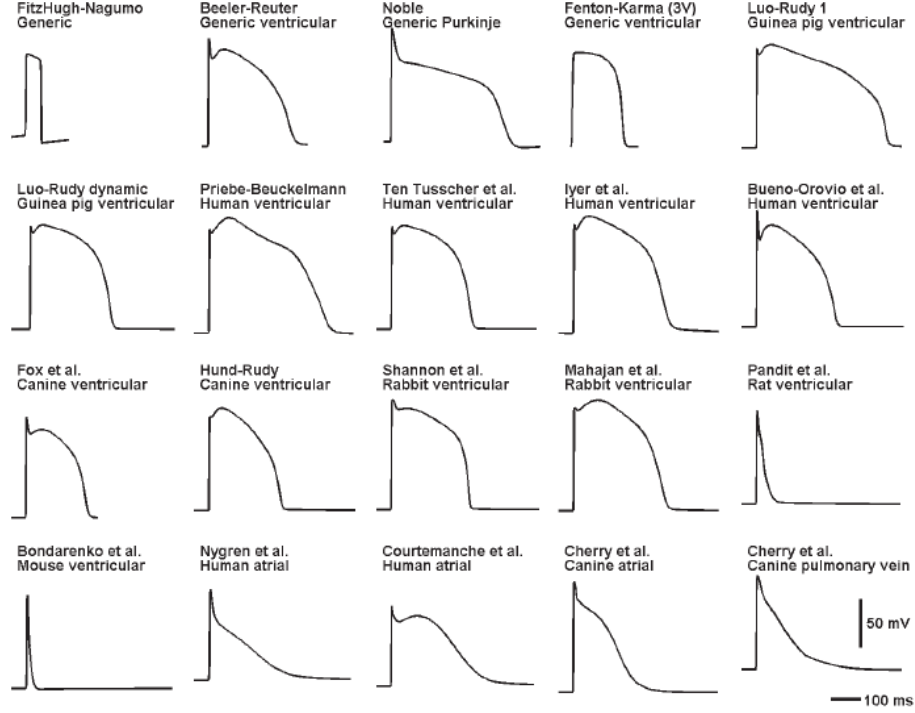


Figure 3.2: APs reproduced through various cardiac electrophysiological models for different regions of the heart and for different species. Adopted from Cherry and Fenton⁷

Eikonal Models: Eikonal models are used for simplified wave-front propagation without producing the reaction part which is basically AP [Franzone et al.¹³¹, Sermesant et al.¹³², Keener and Sneyd¹³³]. Although being very fast in computation, they substantially fail to provide insight into the arrhythmia mechanisms.

3.2 Cardiac Electrical Restitution

AP is highly responsive to the frequency of stimulus applied where the change is more prominently observed in AP duration (APD) which is a duration between the time when the cell is depolarized and the time when the cell is fully depolarized to resting membrane potential. In general, as heart rate increases APD in myocardium decreases. Electrical restitution curve, originally brought up by Bass¹³⁴, is derived from the change of APD as a function of preceding diastolic interval (DI). It is

also called as APD restitution curve and formulated as:

$$APD_{n+1} = f(DI_n) \quad (3.1)$$

The change of APD can also be represented as a function of change in basic cycle length (BCL). It reads as

$$APD_{n+1} = f(BCL_n) \quad (3.2)$$

where BCL is defined as

$$BCL_n = APD_n + DI_n \quad (3.3)$$

Different pacing protocols can be applied to measure APD restitution curve. One particular of them is called S1-S2 (or standard) protocol resulting S1-S2 (or standard) APD restitution curve. In that, the cell is paced at a CL of S1 for a number of time generally until a stability in APD and AP morphology is obtained then follows another stimulus with a CL of S2. This process is repeated for various S2 values. The whole process is depicted in Figure 3.3 where consequent APDs for different S2 values are plotted together (Figure 3.3 A) and resulting standard APD restitution curve (Figure 3.3 B) is displayed. Another type is called dynamic pacing protocol where the pacing CL is varied gradually in either incremented or decremented fashion.

Another mesoscopic property of cardiac tissue is conduction velocity (CV) in which changes in the frequency of stimulation is reflected in the propagation speed of the pulse. In the same way as APD restitution, CV restitution represents the course of change in CV as function of previous DI [Qu et al. ¹³⁵]. It reads as:

$$CV_{n+1} = f(BCL_n) \quad (3.4)$$

APD restitution can be measured either on a single cell, on a network of cells such as cable or on

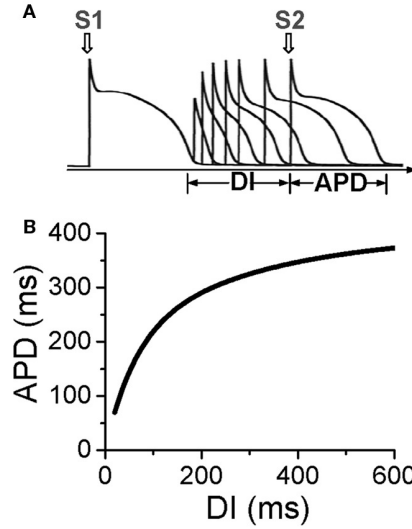


Figure 3.3: Electrical restitution curve derivation. (A) S1S2 protocol to derive APD restitution curve. Here, first stimulus S1 with a fixed frequency is applied for a number of times and then the second stimulus S2 with varying frequency is applied at each time that results different DIs and APDs. (B) A standard APD restitution curve. Adopted from Qu et al.¹²

a 2D or 3D tissue whereas CV restitution can only be measured on a network of cells. In the case of the network of cells, the stimulus is delivered on one site (or cell) and the measurement is taken from a different site.

The restitution curves portray the fundamental characteristics of cardiac tissue. They are linked with electrical alternans manifested either as APD alternans on cardiac membrane [Weiss et al.¹³⁶, Garfinkel et al.¹³⁷] or as T-wave alternans [Verrier and Nearing¹³⁸, Rosenbaum et al.¹³⁹, Smith et al.¹⁴⁰, Pastore et al.¹⁴¹, Klingenstein et al.¹⁴², Narayan et al.¹⁴³] on ECG where correlation of them with the onset of fibrillation has been revealed. The link between electrical alternans and APD restitution curve was found as the slope < 1 of APD restitution played a role in the mechanisms of electrical alternans [Nolasco and Dahlen¹⁴⁴, Guevara et al.¹⁴⁵, Karma¹⁴⁶, Koller et al.¹⁴⁷, Qu et al.¹³⁵]. The principle behind this is that for a cell paced at a certain BCL, there is an equilibrium for each BCL. That point is stable when slope < 1 which means that for a small perturbation on APD or DI values in that point results their convergence back to their values at the equilibrium. However, when the slope is greater than one, the perturbation leads to divergence from the equilibrium point

and promotes alternans. Furthermore, a CV restitution curve which is sufficiently steep over a broad range of DIs was found to be a precursor for the induction of spatially discordant alternans [Echebarria and Karma¹⁴⁸, Fenton et al.¹⁴⁹, Watanabe et al.¹⁵⁰].

3.3 Numerical Methods

In Section 3.1, the ion channel dynamics that serve to model AP for cardiac myocytes is covered. The governing equation defining transmembrane voltage in the most compact way can be defined as:

$$C_m \frac{dV_m}{dt} = I_{stim} - I_{ion} \quad (3.5)$$

where V_m is transmembrane potential, C_m is the cardiac membrane capacitance and I_{stim} is the stimulus current which is large enough to start the depolarization phase of a cardiac cell. I_{ion} is ionic current density which is the consequence of overall ionic channel interactions and changes in the course of a typical AP. There is generally multiple underlying state variables defining the ionic current density. Their number is scaled by the complexity of cardiac model used.

Cardiac cells are excitable and hence AP is propagated through it. The most widely used mono-domain reaction-diffusion equation for the simulation of electrical activity in 2D cardiac tissue adopted by many models is

$$C_m \frac{dV_m}{dt} = \nabla \cdot \sigma \nabla V_m + I_{stim} - I_{ion} \quad (3.6)$$

where σ is conductivity tensor or scalar diffusion coefficient. The reaction-diffusion equation is a system of coupled ordinary differential equations (ODEs) responsible for ionic part and partial differential equations (PDEs) governing the diffusion part. Hence, the system consists of parabolic and elliptic equation sets.

No electrical current between the boundary Γ and extracellular space is assumed. Therefore,

Neumann boundary conditions, or in other words, no flux boundary conditions are prescribed:

$$\Gamma : \mathbf{n} \cdot (\sigma \nabla V_m) = 0 \quad (3.7)$$

where \mathbf{n} is outward normal to the boundary Γ .

3.3.1 PDE Solution

Cardiac tissue is discretized through triangular or grid meshes to solve PDEs. The system of PDEs can be linearized by the discretization. It turns into a linear system of equations (LSEs) in the form:

$$Ax + b = 0 \quad (3.8)$$

Generally, there are three most commonly applied numerical methods to solve LSEs:

Finite Difference Method (FDM): Based on regular or cubic grid of cells. Good for structured, non-complex geometry. Easy to implement, efficient computation.

Finite Volume Method (FVM): Modified FDM for irregular mesh grids.

Finite Element Method (FEM): Based on sub-domain elements in non-uniform shape. Good for irregular, curved, anatomically detailed geometry. Higher computation demand.

3.3.2 Simulating Electrograms

Cardiac membrane potential computed through reaction-diffusion equation does not directly reflect the electrograms measured by electrodes. Extracellular potential has to be computed using the membrane potential. Two approaches are used for this. In the first one pseudo-electrograms are computed using a current source approximation formulation [Plonsey and Barr¹⁵¹, Virag et al.¹⁵²], whereas current source is approximated using the discretized diffusion operators and then solving the Poisson's equation in the second approach [Pullan et al.¹⁵³]. The details of these approaches are as follows.

Current source approximation which is basically integration of electrical activity in the neighborhood of an electrode yields unipolar electrograms. The extracellular potential Φ_e is obtained from this formulation as:

$$\Phi_e(x, t) = \frac{1}{4\pi\sigma_e} \int y \frac{I_m y(t)}{|x - y|} \quad (3.9)$$

where x is the electrode location vector, y is the current source location vector, I_m is the transmembrane current per unit area of cardiac tissue and σ_e is the extracellular conductivity. I_m can readily be obtained through the monodomain equation from the discretized diffusion operator:

$$I_m = I_{ion} - I_{stim} + C_m \frac{dV_m}{dt} = \nabla \cdot (\sigma_i \nabla V_m) \quad (3.10)$$

In the second approach, after finding the current source I_m , a quasistatic electric field is assumed and Φ_e is calculated from solving Poisson's equation which is also the parabolic part of the bidomain formulation:

$$\nabla \cdot [(\sigma_i + \sigma_e) \nabla \Phi_e] = I_m \quad (3.11)$$

The above formulation can be used for ECG simulation based on a torso-heart volume conductor model as well and it is solved using either FEM [Keller et al.¹⁵⁴, Werner et al.¹⁵⁵] or boundary element method (BEM) [van Oosterom and Jacquemet¹⁵⁶]. The advantage of using FEM is that it can handle anisotropy whereas BEM is computationally more efficient.

Another practical approach is the computation of extracellular potential as a weighted sum of the membrane potential since the two are linearly related [Virag et al.¹⁵²].

3.3.3 Parallel Computation Using GPUs

Simulation of cardiac electrical activity plays an important role to understand, visualize, and analyze the heart rhythm disorders such as AF and VF. Such is a type of large-scale biological simulation, hence requires high performance computing tools in order to have a satisfactory and

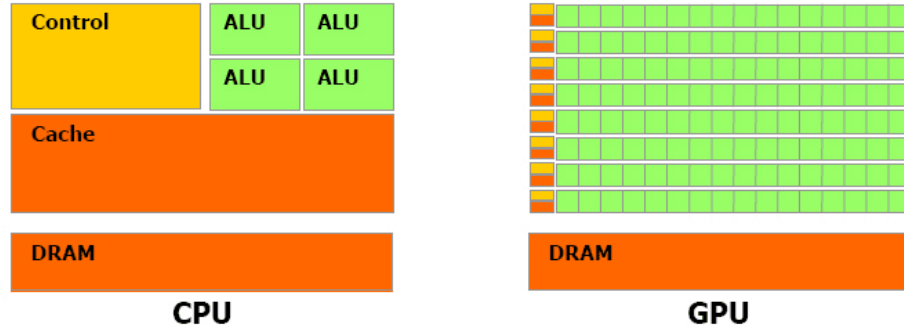


Figure 3.4: Comparison between CPU and GPU architectures. Adopted from Corporation¹³.

nearly real - time simulation speed. Using an average central processing units (CPUs) for this purpose results hours of computation duration for simulation of cardiac electrical activity of a whole heart for a couple of seconds.

Since computation load for cardiac electrical propagation simulation is such demanding, parallel computation have been considered. Early studies have used massively parallel computers, or rather supercomputers, with clusters of processors for this purpose [references]. However, supercomputers are costly and bulky and hence not convenient for every user. Recent development of general-purpose Graphic Processing Units (GPUs) and their availability in personal computers (PCs) make them advantageous for parallel computation. A comparison between typical CPUs and GPUs are depicted in the Figure 3.4. As can be seen, a GPU holds much more processing units. Several studies has already shown computational advantage of GPUs over CPUs [references].

A GPU includes hundreds of computing cores, also called multiple streamers each of which can work in parallel, whereas a CPU includes fewer of them (Figure 3.4). A comparison study based on a cardiac simulation suggests GPUs are about 30 times faster than a single CPU Sato et al.¹⁵⁷. The name general-purpose for GPUs comes from the idea of harnessing them for non-graphics problems although they are originally intended to be used for graphics computing. CUDA architecture is a kind of vendor to NVIDIA GPUs (Figure 3.5]. Hence, compatibility of functions in CUDA helps to make use of GPU architecture in an easy way. The computing cores of a GPU are called threads. In CUDA parallel computation implementen in kernels. The parallel clusters of threads

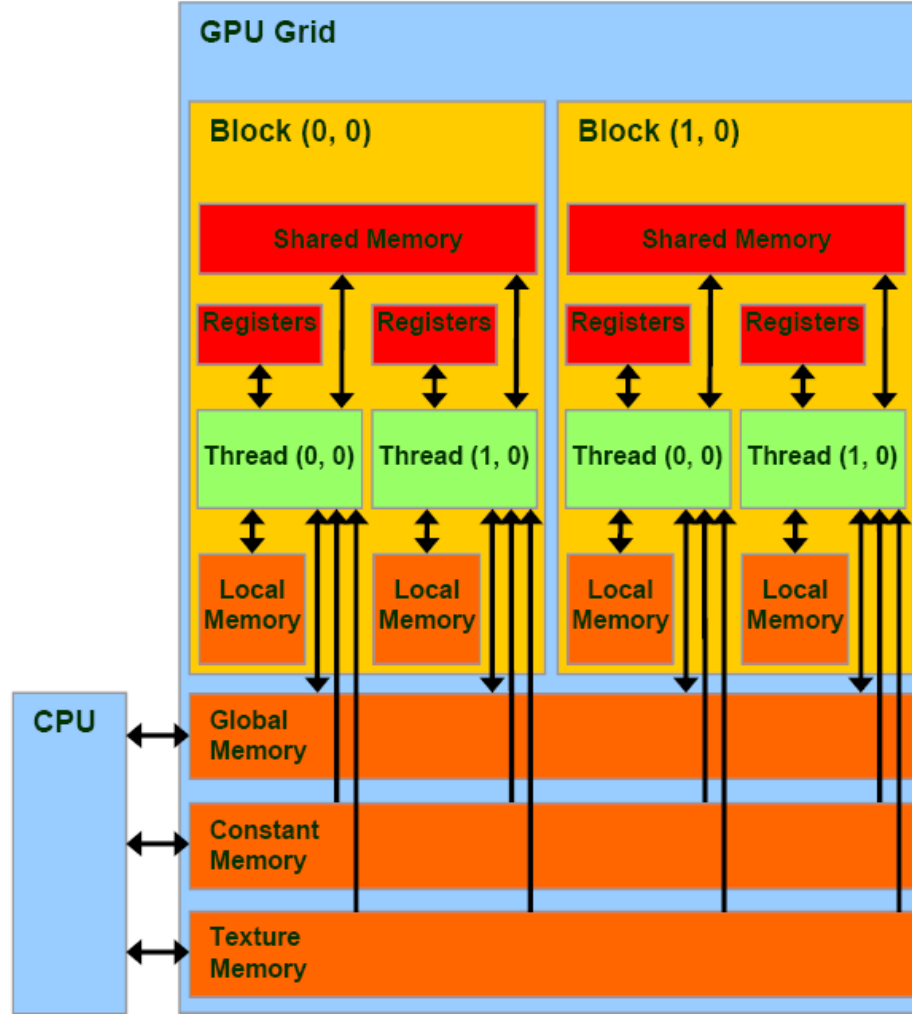


Figure 3.5: Memory architecture for a typical GPU. Adopted from Programming¹⁴.

constitutes blocks and the same way, parallel clusters of blocks constitutes grids. The fact that memory bandwidth of GPU is higher and is not restricted with the deep cache memory allows a better memory performance. Yet there are different memory types in a GPU. They can be listed as global, constant, shared and texture memories. A schematic depiction is shown in Figure 3.5. Since data transfer between threads effects the latency in the computation, using appropriate memory type is also essential for an efficient simulation.

We shall provide some more detail on the memory types:

Global Memory: As can be seen from Figure 3.5, global memory is accessible by every thread, but is not cached. It is both readable and writable. It has relatively large storage capacity (about 1 GB). It has low memory bandwidth which determines the rate at which data is read and written. Hence, it has relatively higher latency. However, specific to access pattern of an application and the device type, the memory access can be coalesced.

Local Memory: Like global memory, local memory is both readable and writable and not cached. It has a limited memory size (in KBs). Every thread has its local memory and the data access pattern is always coalesced.

Shared Memory: It is also readable and writable. It is fast, but it has a limited memory size (in KBs). It is on-chip memory where only threads in a block can get access to. Equally sized banks are allocated on the shared memory, so that threads can get access to them simultaneously. The memory access can be as fast as accessing registers as long as bank conflicts are avoided.

Registers: It is readable and writable. It is the fastest memory unit on a GPU, however, it has a very limited size.

Constant Memory: Unlike global and shared memories, constant memory is read only. Like shared memory, it has a limited memory size (in KBs), however it is cached. The number of different addresses read by all threads determines the read cost.

Texture Memory: Like constant memory, texture memory is read only and cached. However, it has a relatively large size. Another difference is that it has an optimized caching with the exploitation of 2D spatial access pattern. Depending on the application though, reading from texture memory is faster than reading from global and local memory.

As far as the solution for PDE part of cardiac wavefront propagation is concerned, the access pattern is more local than global. This fact can be exploited when using the memory.

Part II

Methods

Chapter 4: Reduced Order Cardiac Modeling

In this chapter, methods for parameter estimation of a phenomenological cardiac model to match targeted behaviors first generated from a bio-physically detailed model are discussed. In particular, a parameter estimation scheme using extended Kalman filter (EKF) is introduced. For comparison purposes, particle swarm optimization (PSO) and sequential quadratic programming (SQP) algorithms are implemented as additional parameter estimation schemes. Targeted electrophysiological behaviors are human atrial APs for which electrophysiological heterogeneity was taken into account as well as rhythm disorder disease based electrical remodeling. As such, a complexity reduction is achieved in terms of modeling electrophysiology of human atria. This is visualized in Figure 4.1.

Remainder of this chapter is organized as follows: In section 4.1, details on phenomenological and biophysically detailed models used are covered. In section 4.2, targeted electrophysiological behaviors are discussed. In section 4.3, parameter estimation scheme using EKF is introduced then other schemes using SQP and PSO are presented.

4.1 Electrophysiological Models

Existing human cardiac models in varying complexity and efficiency are covered in subsection 3.1.1. In this chapter, Courtemanche-Ramirez-Nattel (CRN) model [Courtemanche et al.¹¹] and a '*minimal resistor model*' (MRM) [Bueno-Orovio et al.²²] are used as a biophysically detailed and a phenomenological model, respectively.

CRN includes a total of 12 ionic currents of human atrial membrane and the dynamics are represented by 24 state variables. Therefore, it is computationally demanding and difficult to analyze. MRM is a modified version of 3-variable Fenton-Karma model [Fenton and Karma²⁰] including an additional state variable. MRM incorporates only 3 ionic currents which are summarized as fast inward, slow inward, and slow outward currents. AP morphology and arrhythmogenic characteristics are virtually preserved in MRM. Hence, it is preferential for fast and large-scale simulation of

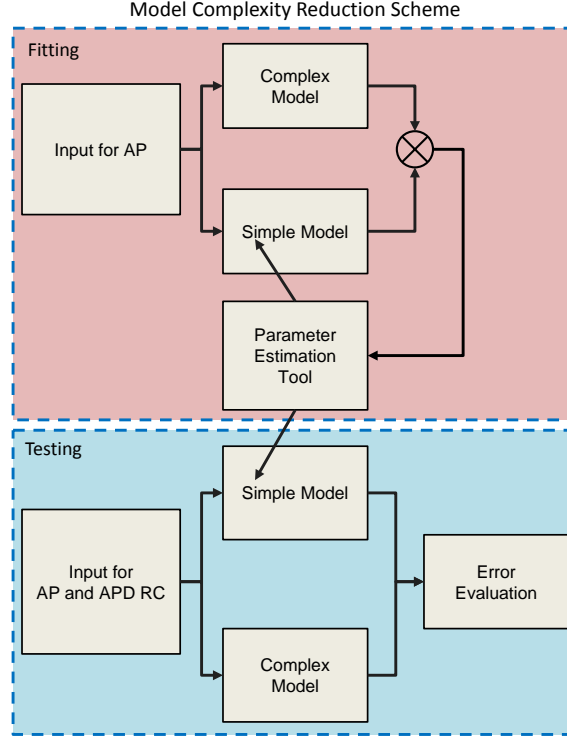


Figure 4.1: Model complexity reduction block diagram

electrophysiological dynamics of cardiac tissue, and also computationally more tractable and easier for analysis. For comparison of computational speed, 2D simulations of varying grid dimensions are performed using both models. Benchmark results are shown in Figure 4.2 where computational speed of both models are compared with respect to number of elements in the grid network of cells. Computational speed measure is assessed through dividing simulation time by real time elapsed. It can be seen that MRM is more than 3 times faster comparing to CRN for smaller dimensions. This ratio increases even more (up to more than 6) as the dimension increases. These results confirm that MRM is favorable over CRN in computational efficiency and it is even more so for larger scale simulations.

The equations defining MRM is given in Appendix A. Each parameter of MRM is in general responsible for a particular period in a typical AP and that makes parameter sensitivity analysis easier. Several studies investigated parameter estimation of MRM. In [Bueno-Orovio et al.²²], a parameter optimization using sequential quadratic programming (SQP) was performed to reproduce

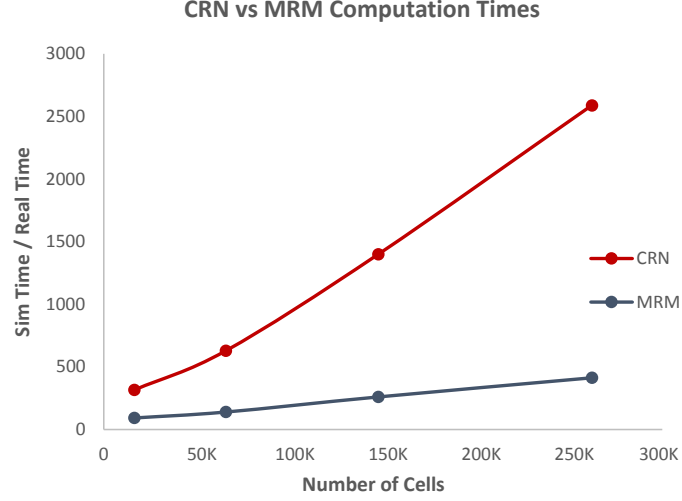


Figure 4.2: Comparison of computational speed between MRM and CRN.

cellular and tissue-level dynamics of two ventricular biophysical models with a good matching of AP and restitution curve (RC) morphologies. In [Liu et al.¹⁵⁸], a modified hybrid Nelder-Mead simplex search and PSO was used to reproduce AP morphology obtained both from an isolated guinea pig ventricular myocyte and from a ventricular biophysical model.

The transmembrane potential resulted from CRN model is defined in mV units whereas it is dimensionless when it is resulted from MRM. Therefore, the transmembrane voltage resulted from MRM is rescaled so that the error is within an admissible value when the two models are compared. The scaling is done in the following way,

$$\bar{V}_m = u^{max}(V_m - V_m^{min})/(V_m^{max} - V_m^{min}) \quad (4.1)$$

where \bar{V}_m is rescaled membrane voltage, u^{max} is the maximum value of dimensionless voltage produced by MRM, V_m^{max} and V_m^{min} are the maximum and minimum membrane voltage values produced by CRN model respectively.

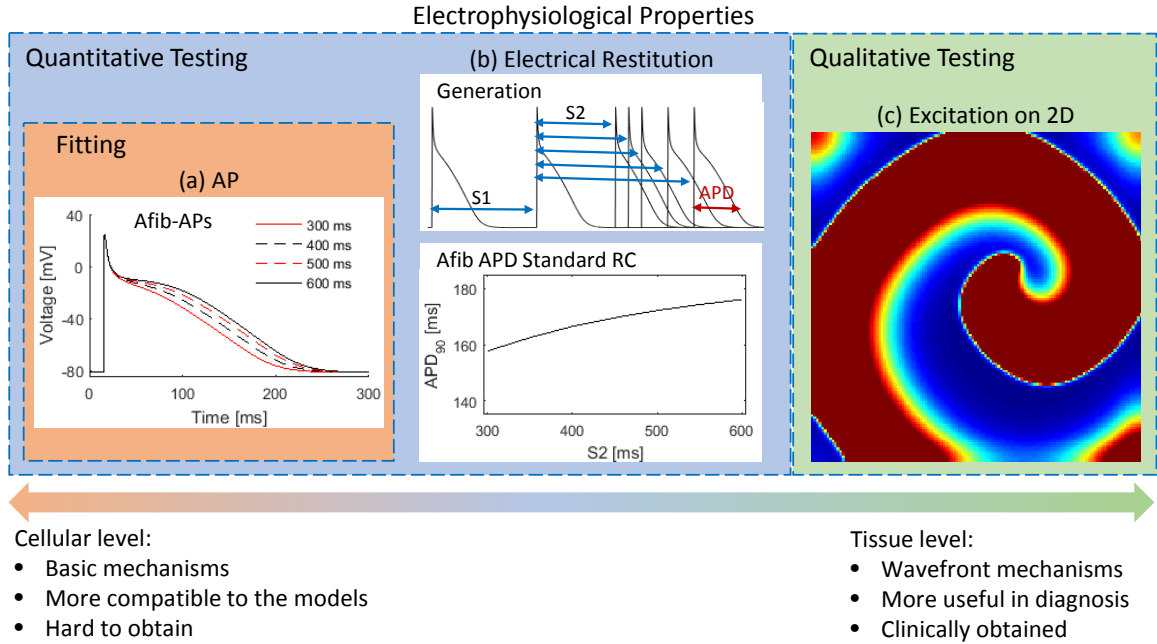


Figure 4.3: Representation of electrophysiological properties from cellular to organ level with different characteristics used for different fitting-testing purposes.

4.2 Electrophysiological Properties

As mentioned before, AP as the output of cardiac models is targeted as an electrophysiological behavior to be matched. Heterogeneity in AP morphology throughout atrial regions are considered as well. Furthermore, Afib based electrically remodeled AP for atrial working myocardium is considered besides normal AP of a healthy atrial myocardium. In some cases, APD standard RC is also matched using estimated parameter sets in order to evaluate the goodness of fitting. However, it is not used as a feedback to any of parameter estimation schemes. Finally, in order to qualitatively evaluate the matching performance, excitation patterns on a 2D tissue patch are also compared. A representation of how electrophysiological properties with different characteristics are used is provided in Figure 4.3.

Heterogeneous APs: Due to its heterogeneous structure, different regions of atria incorporates different electrophysiological characteristics. An experimental study on canine atria has shown different AP measurements from different anatomical regions such as pectinate muscle (PM), crista

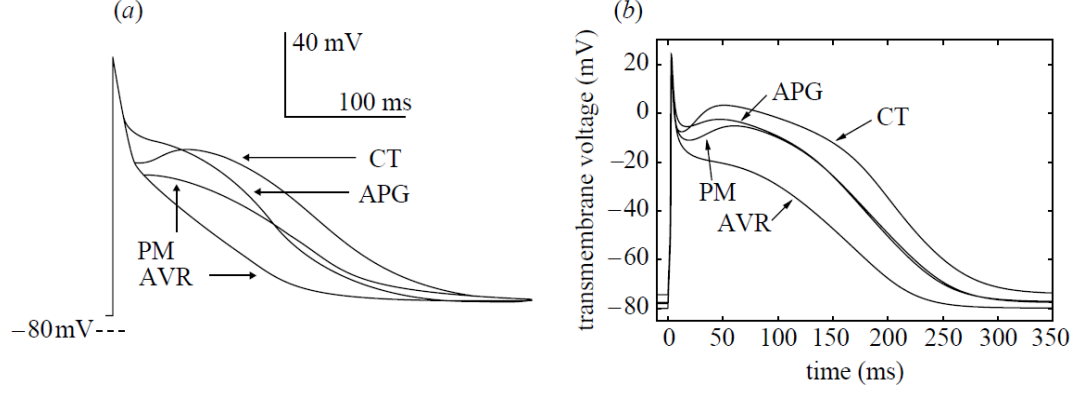


Figure 4.4: APs of different cell types from atrial regions PM, CT, APG, and AVR. (a) Experimentally measured heterogeneous APs by Feng et al. [Feng et al. ¹⁵] and (b) modeled APs. Figure from Seemann et al. ¹⁶.

terminalis (CT), atrioventricular ring (AVR), and appendage (APG) [Feng et al. ¹⁵]. Variation on AP shapes were observed even for the same regions. Later on, Seemann et al. [Seemann et al. ¹⁶] adjusted CRN model parameters, specifically maximal conductance of I_{to} , $I_{Ca,L}$, and I_{Kr} , to the average value of experimental APs and simulated APs for each region (Figure 4.3). Left atrium (LA) and right atrium (RA) working myocardium and Bachmann's Bundle (BB) cells were modeled same as PM cells. Table 4.1 shows ionic conductance scaling of CRN model to reproduce AP heterogeneity [Seemann et al. ¹⁶].

Afib APs: electrophysiological remodeling induced by Afib was modeled through CRN [Courtemanche et al. ¹⁷] in reference to experimentally recorded APs from patients Boutjdir et al. ¹⁵⁹. This was done by scaling several conductance values as shown in Table 4.2. Both healthy and Afib based electrically remodeled APs at different frequencies produced using CRN are demonstrated in Figure

Table 4.1: Human atrial AP heterogeneity

Conductances	PM, LA, RA, BB	Conductance scalings for different regions		
		CT (%)	APG (%)	AVR (%)
$G_{to,max}$	$0.1652nSpF^{-1}$	128	68	100
$G_{Ca,L,max}$	$0.1238nSpF^{-1}$	167	106	67
$G_{Kr,max}$	$0.0294nSpF^{-1}$	100	100	153

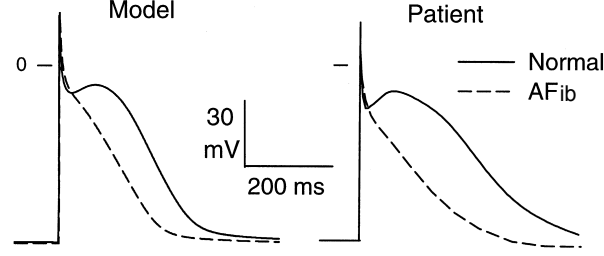


Figure 4.5: Healthy and Afib based electrically remodeled APs experimentally recorded from patients are respectively compared with modeled ones. Figure from Courtemanche et al.¹⁷.

4.5. AP is a periodic event representing the change in membrane potential for a certain period. Resulting waveform varies due to the rate the cell is paced. Therefore, AP waveforms under different frequencies are considered here.

APD Standard RC: In this context, APD standard RC is calculated for a single cell using $S1-S2$ stimulus protocol as described in Section 3.2. Generation of the curve is visualized in Figure 4.3 (b). The simulated cell was paced at a first stimulus $S1$ for 20 s, then applied afterwards was a single second stimulus $S2$ of varying CLs over a range (e.g. between 200 and 700 ms). That was repeated for each $S2$ stimulus. After the $S2$ stimulus 90% of the time required for a full repolarization, which is called APD_{90} , and the BCL was measured to form the RC.

Wavefront Propagation: Simulations of wavefront propagation are performed using mono-domain reaction-diffusion equation (see Equation 3.6) on a 200x200 discretized 2D grid with a spatial resolution $\Delta x = 0.05$ cm. The temporal resolution is set to $\Delta t = 0.1$ ms. Cardiac membrane capacitance is set to $C_m = 1$ mF. Diffusion part is solved using FDM. All of listed simulation specifics are held

Table 4.2: Constructing electrically remodeled CRN model

Conductances	Sinus Rhythm, CRN-N	Conductance scalings
		Remodeled, CRN-AF (%)
G_{to}	$0.1652nSpF^{-1}$	50
$G_{Ca,L}$	$0.1238nSpF^{-1}$	30
$G_{K_{ur}}$	-	50

the same for both models and isotropic tissue is assumed for both. The diffusion coefficient is set to $\sigma = 0.0012 \text{ cm}^2$ for CRN whereas different values are used for MRM in order to approximate conduction velocity and hence wavelength values for an estimated parameter set to that of obtained from CRN. Reentry initiation is done using cross-field stimulation.

4.3 Parameter Estimation Schemes

Once again, the task in this chapter is to estimate parameters of MRM through an estimator that uses output of CRN. For this, a general parameter estimation scheme into which any estimator can be incorporated, demonstrated via a block diagram in Figure 4.1, is proposed. Three types of estimators used: EKF, SQP, and PSO. In the scheme, the measurements to tweak parameters of simple model are obtained from a complex model; hence it implies model complexity reduction as well. Here, simple model and complex model respectively refer to CRN and MM which are called as such throughout the paper. Note that estimated parameter set is used to simulate AP and APD RC for error evaluation during testing part. Since the two models operate on different units, inputs for each model is modulated to have similar initial conditions. Error evaluated at each filtering step k for EKF whereas it is calculated at the end of estimation loop for SQP and PSO.

Before going into details of the estimators, error computation for the assessment of goodness in fitting during electrophysiological behavior matching shall be discussed. Behaviors to be compared are characterized as signals as far as AP and the APD RC matching is concerned. For evaluation of goodness in fitting, normalized root mean square error (NRMSE) which results a similarity measure between two signals in terms of percentage is used. It is defined as:

$$NRMSE = \sqrt{\frac{1}{n} \sum_{i=1}^n e_i^2} \quad (4.2)$$

where n is the length of the signals to be compared and e_i is the normalized absolute error between the signals at instance i . It reads as:

$$e_i = 100 \left| \frac{\bar{q}_i - q_i}{\bar{q}_{max} - \bar{q}_{min}} \right| \quad (4.3)$$

where \bar{q}_i is the targeted signal and q_i is the signal to be adapted at i . Note that, i represents a time instance in case of AP matching whereas it represents BCL in case of RC matching. The error value for AP is the difference between voltage values whereas it is the difference between APD values given a corresponding BCL in case of APD RC. In this study, a more collective fitting error is obtained by taking by taking average of NRMSE values resulted from AP and APD restitution. Note that error values used within each estimator as a feedback can be different. Specifically, voltage difference at each step is used in EKF whereas quadratic error is used in SQP and PSO.

4.3.1 Extended Kalman Filter

Kalman filter, named after Rudolph Kalman, originates from several different studies in the 1950s [Kalman¹⁶⁰]. It is a powerful tool for state estimation of linear systems with noises that proves to be optimal in the sense of least square estimate [Rhodes¹⁶¹]. For nonlinear systems, on the other hand, it cannot be proven to be optimal in state estimation. However, the state estimation can still be implemented in several modified forms such as EKF. EKF utilizes the approximation of a nonlinear system with linearization on its current estimates of states trajectory using Taylor series expansion. EKF has been successfully used in many practical applications [Simon¹⁶²]. The state estimation has been further developed to estimate unknown parameters of a system [Kopp and Orford¹⁶³] and that has rendered Kalman filter as a system identification tool. Furthermore, it has been used for neural network training [Sum et al.¹⁶⁴] and feedback error learning [Ruan et al.¹⁶⁵].

In this part, parameters of MRM are iteratively changed using EKF to match the output signal obtained from CRN at each iteration. Note that at each filtering step a new parameter set for the simple model is estimated and used to simulate certain cardiac behaviors for error evaluation in comparison to the behaviors simulated through complex model.

Consider a general nonlinear dynamic system with additive artificial noise profiles:

$$\dot{z} = f_c(z(t), u(t)) \quad (4.4)$$

$$y_k = h_c(z_k) + v_k \quad (4.5)$$

Where f_c is the complex model plant, h_c is the measurement function of the complex model, and v_k is the measurement noise associated with Gaussian zero mean white noise with a covariance matrix of R . Since measurement is taken here from a single state which is the membrane potential of complex model, R becomes a scalar representing only variance in the measurement.

The EKF includes a *prediction step* and a *correction step* at each filtering iteration. In the prediction step a new priori estimate of the state vector is performed using the assumed system model. In this scheme, it is the simple model. Governing equation for the simple model:

$$\dot{x} = f_s(x(t), u(t)) \quad (4.6)$$

where f_s is the nonlinear simple model plant with its state vector augmented with the parameters to be estimated. In this context, MRM the simple model includes 28 parameters, therefore the augmented system becomes 32-dimension. The states vector is then represented as:

$$x = [\lambda, \tau]^T \quad (4.7)$$

where original state vector is as follows:

$$\lambda = [u, v, w, s]^T \quad (4.8)$$

and the parameter vector is as follows:

$$\begin{aligned} \tau = & \left[u_o, u_u, \theta_v, \theta_w, \theta_o, \theta_v^-, \tau_{v1}^-, \tau_{v2}^-, \tau_v^+, \tau_{w1}^-, \tau_{w2}^-, k_w^-, u_w^-, \tau_w^+, \dots \right. \\ & \left. \dots \tau_{fi}, \tau_{o1}, \tau_{o2}, \tau_{so1}, \tau_{so2}, k_{so}, u_{so}, \tau_{s1}, \tau_{s2}, k_s, u_s, \tau_{si}, \tau_{w\infty}, w_\infty^* \right]^T \end{aligned} \quad (4.9)$$

A discrete EKF is used here. Hence, a priori estimation of the state x_k^- is evaluated as:

$$\hat{x}_k^- = \hat{x}_k^+ - 1 + \int_{(k-1)\Delta t}^{k\Delta t} f_s(\hat{x}^+(t), u(t))dt + w_k \quad (4.10)$$

Δt is the filtering time step, and dt is the integration time step for the nonlinear plant. Note that observation from the complex model also takes place at $t = k\Delta t$ at each filtering iteration, k . w_k is the process noise associated zero mean, uncorrelated Gaussian white noise covariance matrix Q which is represented as:

$$Q = \begin{bmatrix} \alpha R I_4 & \mathbf{0} \\ \mathbf{0} & \alpha R W \end{bmatrix} \quad (4.11)$$

α is process to measurement error variance ratio, I_n is $n \times n$ identity matrix. Parameter state variables are further scaled using a weighing matrix, W , whose non-diagonals are zeros and diagonals is a vector, w , whose elements are defined as:

$$w_i = \tau_{i,sup} - \tau_{i,inf}, \quad i = 1, 2, \dots, 28 \quad (4.12)$$

$\tau_{i,sup}$ and $\tau_{i,inf}$ are upper and lower bound specified for the i th parameter state, respectively.

Upper and lower bounds for the parameters are provided in Appendix B.

The predicted measurement is then estimated as:

$$\hat{y}_k = h_s(\hat{x}_k^-) \quad (4.13)$$

where h_s is the measurement function of the simple model. The nonlinear state transition and the measurement functions are linearized around the trajectory using Taylor series expansion as

shown:

$$\Phi_k = I + \Delta t \left[\frac{\partial f_s(x(t), u(t))}{\partial x(t)} \right]_{x(t)=\hat{x}_{k-1}^+} \quad (4.14)$$

$$H_k = \left[\frac{\partial h_s(x_k)}{\partial x_k} \right]_{x(t)=\hat{x}_{k-1}^+} \quad (4.15)$$

Having these obtained, propagation of *a priori* state estimation error covariance matrix P_k^- is evaluated as:

$$P_k^- = \Phi_k P_{k-1}^+ \Phi_k^T + Q \quad (4.16)$$

In the *correction step*, the predicted state estimates of the simple model are updated based on the measurement obtained from the complex model. First, Kalman gain is obtained using *a priori* state estimation error covariance, linearized output function, and the measurement error covariance matrix which is as follows:

$$K_k = P_k^- H_k^T \left[H_k^T P_k^- H_k + R \right]^{-1} \quad (4.17)$$

Then, propagation of *a posteriori* state estimation error covariance matrix is evaluated as:

$$P_k^+ = \left[I - K_k H_k \right] P_k^- \left[I - K_k H_k \right]^T + K_k R K_k^T \quad (4.18)$$

The filtered state now is as follows:

$$\hat{x}_k^+ = \hat{x}_k^- + K_k (y_k - \hat{y}_k) \quad (4.19)$$

Finally, since simple model parameters, τ , work only inside an admissible set, it is a state-constrained system to which Kalman filter is not sensitive. Hence, an estimate projection method with inequality constraints [Simon¹⁶⁶] can be used to project the unconstrained estimate $\hat{\tau}_k^+$ onto

the constraint surface and obtain the constrained estimate $\tilde{\tau}_k^+$ as:

$$\tilde{\tau}_k^+ = \arg \min_{\tau} (\tau - \hat{\tau}_k^+)^T I (\tau - \hat{\tau}_k^+) \quad (4.20)$$

The system thus satisfies the inequality constraint:

$$\tau_{inf} \leq x \leq \tau_{sup} \quad (4.21)$$

I is a positive-definite weighting matrix considered in this context as an identity matrix. This is a typical quadratic problem where different approaches can be taken such as interior point algorithm and active set method [Fletcher¹⁶⁷, Boyd and Vandenberghe¹⁶⁸]. In this context, for efficiency, the unconstrained state estimate is projected to the nearest boundary whenever that boundary is passed.

Through the estimation, the parameters change between upper and lower bounds specified for each of them. In order for better visualization of the change during different time periods of an AP or AP train course, a normalized change in each parameter from their initial values was calculated every filtering step k which reads as:

$$\bar{\tau}_{i,k} = (\hat{\tau}_{i,k} - \tau_{i,0})/w_i, \quad i = 1, 2, \dots, 28 \quad (4.22)$$

$\bar{\tau}_{i,k}$ is the normalized change, $\hat{\tau}_{i,k}$ is the estimated value, and τ_0 is the initial value for the i th parameter at time step k .

Estimated parameters at each filtering step k are evaluated for AP and APD standard RC. Visualization of the parameter estimation using EKF together with error evaluation throughout the estimation process is provided in Figure 4.6. AP and APD RC generated from the complex model, CRN, and their evaluation generated from the simple model, MRM, using estimated parameter values at an observation point (i.e. filtering step) can be seen (Figure 4.6 (a,b)). It is also shown how normalized changes in parameters at each step is tracked (Figure 4.6 (c)). Here 0 represents no change, 1 represents increasing to the upper boundary whereas -1 represents decreasing to the lower

defined as:

$$\begin{aligned} & \underset{x}{\text{minimize}} && f_0(x) \\ & \text{subject to} && f_i(x) \leq b_i, \quad i = 1, \dots, m. \end{aligned} \tag{4.23}$$

where x is a vector of variables and f_0 is a non-linear scalar function which is also called "objective function". The task is to minimize an objective function subject to one or more other functions called "constraint functions". Here f_i is one of the constraint functions that limits or defines a subset of the variables x . Here, the objective function is defined as the difference between voltage membrane computed by biophysically detailed human atrial model, CRN and phenomenological model MRM. The variables include the parameters of MRM to be tweaked in order to minimize the fitting error. The constraint function only limits the parameter values since they operate only in an admissible set.

SQP is a nonlinear programming method which is used to minimize the parameter fitting error. It is a state of art method in constrained optimization problems. It was shown to have the best performance compared to other methods [Schittkowski¹⁶⁹]. In that study, it was implemented on a collection of test models where the number of variables was up to 100.

Parameters to be optimized were constrained and Newton iteration method is applied utilizing Hessian of the Lagrangian function. At each iteration step a quadratic error function is defined. The general stages of SQP implementation can be summarized as:

- Updating the Hessian Matrix
- Quadratic Programming Solution
- Line Search and Merit Function

Here, MATLAB's *fmincon* function was used to perform SQP.

4.3.3 Particle Swarm Optimization

Here, a basic form of PSO algorithm [Kennedy¹⁷⁰] to estimate parameters of the MRM that give similar qualitative behavior to that of the CRN model is used. The objective function being

optimized is defined as to achieve AP matching to minimize quadratic error between the waveforms of APs.

PSO algorithm is biologically inspired by the way a swarm of animals making decision collectively flocking in a group to find the best location to survive or hunt for food. Each particle, a member of the swarm, has a memory of its previously found best position along with full knowledge of its neighbors individual best found positions so far. The particle then moves to a better position toward its previously found best positions and neighbors global best. PSO algorithm is iterative and has random scaling of influence of the distances between current location and the best known positions. Equations govern the position and its dynamic of each particle is as follows:

$$v_{id}(t+1) = \omega v_{id}(t) + \varphi_p r_p (p_{id}(t) - x_{id}(t)) + \varphi_g r_g (p_{gd}(t) - x_{id}(t)) \quad (4.24)$$

$$x_{id}(t+1) = x_{id}(t) + v_{id}(t+1) \quad (4.25)$$

$x_{id}(t)$ is position of the particle i in dimension d at iteration t , and similarly $v_{id}(t+1)$ is its speed. p_{id} is the best known position encountered by the particle i so far, whereas $p_{gd}(t)$ is the best known position encountered by all the particles. In this sense, the basic PSO algorithm used here has knowledge from global neighborhood of entire swarm, while other PSO variants may deploy different local network topology and swarm movement strategy [Meza et al.^{171, 172}; Arora and Singh¹⁷³]. Since global PSO algorithm has influence from all particle within the swarm, it may stuck at local minima more often than local PSO version. To mitigate this issue, the basic global PSO algorithm is run multiple times (100 runs) and the one with smallest NRMSE of AP morphology comparison is chosen. ω is the inertia weight controlling change of speed. φ_p and φ_g are the learning rate coefficients for personal best influence and swarm or neighborhood best influence, respectively.

Chapter 5: Simplified Cardiodynamic Tissue Characterization

In this chapter, methods to test a hypothesis that the wavefront propagation patterns in cardiac tissue during cardiac fibrillation can be qualitatively characterized using only spatiotemporally local recorded EGM signals based on a simulation study are discussed.

In the present context, a set of locally measured virtual EGM signals are used to characterize the tissue state of wavefront dynamics on the basis of electrical rotor behaviors. Work-flow for the characterization implemented via clustering and classification is demonstrated in Figure 5.1. The work-flow includes following steps: First, forward simulations using MRM were performed to generate spiral waves that can be classified into three distinct behaviors: stationary, meandering, and breakup. Examples of each spiral behavior including corresponding EGMs measured from single channel of each and some spectral parameters extracted from EGMs are shown in Fig. 5.2. EGMs were obtained from each simulation as measurement protocol is varied over catheter type used, their location on the tissue, and reading style as being unipolar or bipolar. An information theoretical distance measure between simulated behaviors are assessed in two ways. First, feature-free implementation of NCD scheme is used where a set of EGMs from each behavior are used directly. Second, feature bias is either introduced to the NCD scheme or NCD concept is reformulated through some features such as normalized FFT distance (NFFTD) proposed in this paper. Clustering and classification analysis is then carried out to test effectiveness of both approaches. As details are provided in Chapter 7, robustness of NCD in classification to both intra-measurement and inter-measurement protocols and presence of noise are tested. Similarly, classification of local behaviors in the presence of heterogeneous behaviors throughout tissue were tested.

The remainder of this chapter is organized as follows: In section I, methods used for simulation of spiral behaviors and intracardiac EGMs is discussed. In section II, the feature-free distance measure NCD is introduced. In section III, NCD with feature bias is presented. Finally in section IV and V, clustering and classification schemes are presented, respectively.

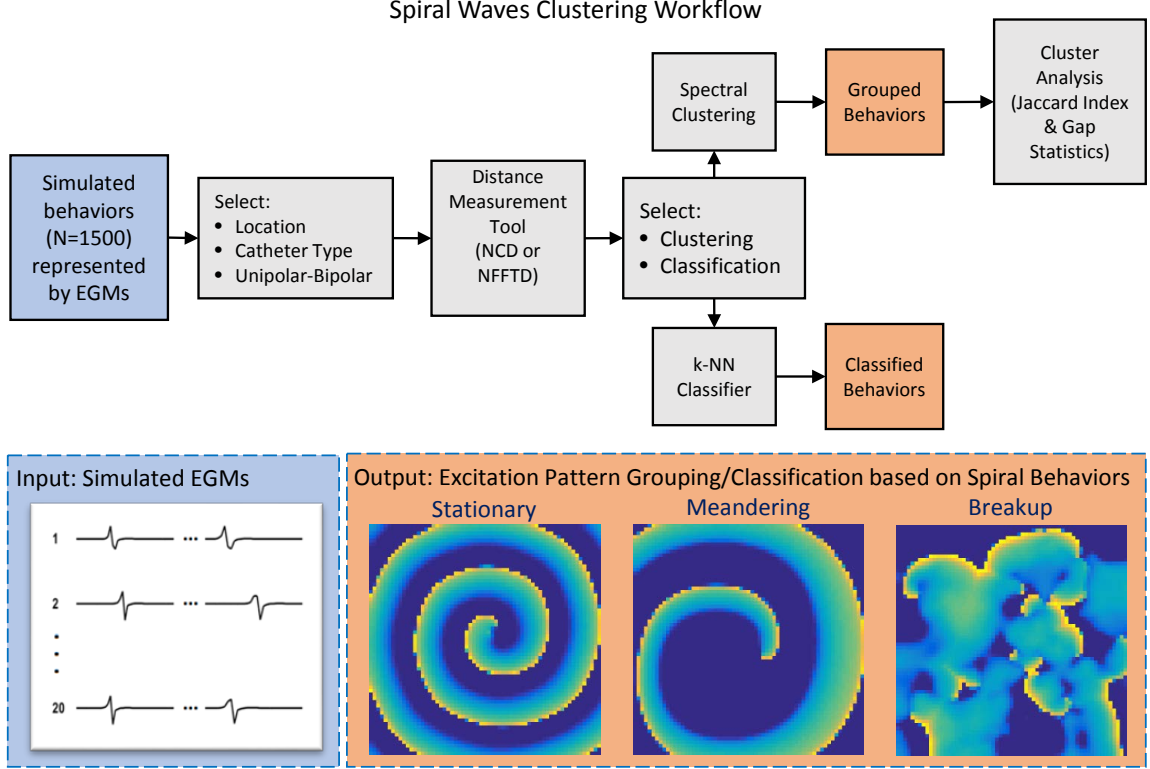


Figure 5.1: Spiral waves characterization work-flow

5.1 Simulating Spiral Waves and Intra-cardiac Electrograms

Spiral waves are simulated on a 2D grid using mono-domain reaction-diffusion equation which is the Equation 3.6 provided in Section 3.3. For the solution of diffusion part, FDM is used. The details of cardiac electro-physiology simulation was covered in Chapter 3. MRM [Bueno-Orovio et al.²²], a 3 variable version of Fenton-Karma model [Fenton and Karma²⁰], for modeling the electro-physiology hence the reaction part is used (see Appendix A). Accurate adaptability of both FK and MRM to diverse electro-physiological measurements was demonstrated in various studies. Specifically, parameters of FK was tweaked to reproduce action potential duration (APD) and conduction velocity (CV) restitution properties obtained from healthy and with chronic AF sheep atria [Goodman et al.¹⁷⁴]. FK was modified to reproduce AP and electrical restitution properties of canine pulmonary vein and left atrial myocytes [Cherry et al.¹⁷⁵]. MRM was shown to reproduce AP and electrical restitution properties of human ventricular myocardium [Bueno-Orovio et al.²²]. We

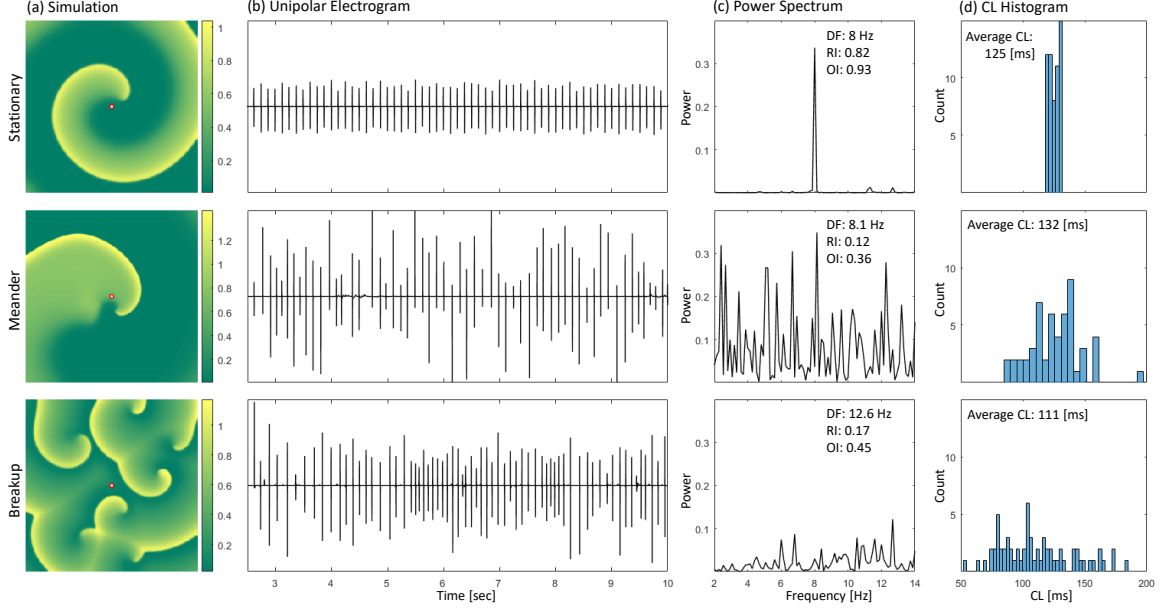


Figure 5.2: Spiral behavior prototypes simulated on 10 cm x 10 cm 2D patches (a) with corresponding recorded unipolar electrograms measured from the center of each patch (b), DF, OI and RI (c), and CL histogram (d) extracted for demonstration purpose only. In this case, only RI and OI parameters for stationary spiral behavior results in distinct values. OI: Organization index, RI: Regularity index, DF: Dominant Frequency, CL: Cycle Length.

demonstrated through a parameter estimation scheme [Alagoz et al.¹⁷⁶] that MRM could reproduce AP and APD restitution properties which were outputs from a human atrial model [Courtemanche et al.¹⁷] developed based on the measurements from electrically remodeled human atrial myocytes. Finally, we demonstrated that MRM could reproduce APs from different anatomical regions of healthy human atria [Alagoz et al.¹⁷⁷]. Thus, MRM originated from FK can be considered as a credible candidate to be a representative model for human cardiac membrane electrophysiology.

Simulations are performed on a 25.6 cm x 25.6 cm 2D patch. A temporal step of 0.1 ms and a spatial step of 0.5 mm is used. The diffusion rate or conductivity is assumed to be isotropic and set to 0.00116 cm²/S. As covered in Section 3.3.3, simulation of cardiac electro physiology is computationally demanding. However, being a distributed system, the use of parallel computation tools such as GPUs may significantly speed the simulation. Speedup advantage of parallel computing is used in the simulation. Computation was performed on NVIDIA Quadro 4000 GPU working on a HP workstation with Intel Xeon(R) CPU E5520 @2.27 GHz with 4 core is used. Simulation algorithm

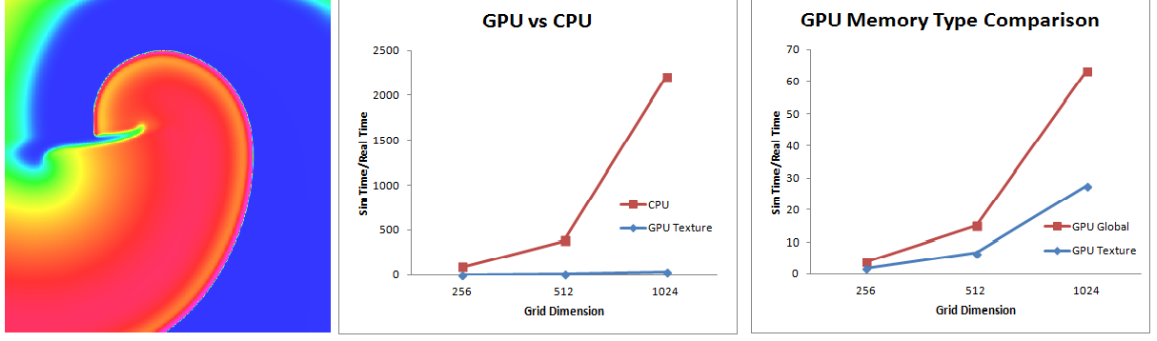


Figure 5.3: Left: Spiral wave using the MRM on a 512 x 512 grid. Middle: Simulation speed comparison between GPU with texture memory used and CPU. Right: Simulation speed comparison of GPU with global memory used versus texture memory used. Grid dimension represents the number of elements (cells) on one side of rectangular lattice on which the simulation was performed.

was run on CUDA software. For speedup purposes, floating point arithmetics were performed using single precision. A comparison of simulation speed using CPU and using GPU is provided in Figure 5.3. GPU was programmed to use texture memory for further speed up. As can be seen in Figure 5.3, GPU is about 2 times faster when programmed to use texture memory for data transfer between the threads. This makes sense since we are simulating a distributed system and texture memory is cached on the chip and the threads can benefit spatial locality where they can access the memory easily.

Multiple spiral behaviors are generated for 10 seconds by changing a subset of the parameters of MRM such as τ_w^+ , τ_w^- , τ_{fi} , τ_{si} , and τ_{so1} . The listed parameter space of MRM was explored in a workshop study where spiral initiation protocol was held fixed [Bartocci et al.¹⁸]. Figure 5.4 shows a subset of the resulting spiral behaviors and respective tip movements when changing τ_w^+ and τ_w^- . Interested reader can refer to Appendix A for the detailed model equations. Similarly, a context providing rationale behind different spiral wave behavior generation is provided in the following paragraphs. Here, a presentation of the effect of varied parameters on the spiral wave behaviors is provided in Table 5.1.

Spiral waves generated are labeled under three subtypes: stationary, meandering, and breakup. Specific tissue properties needed to be set in order to simulate each behavior. In case of stationary

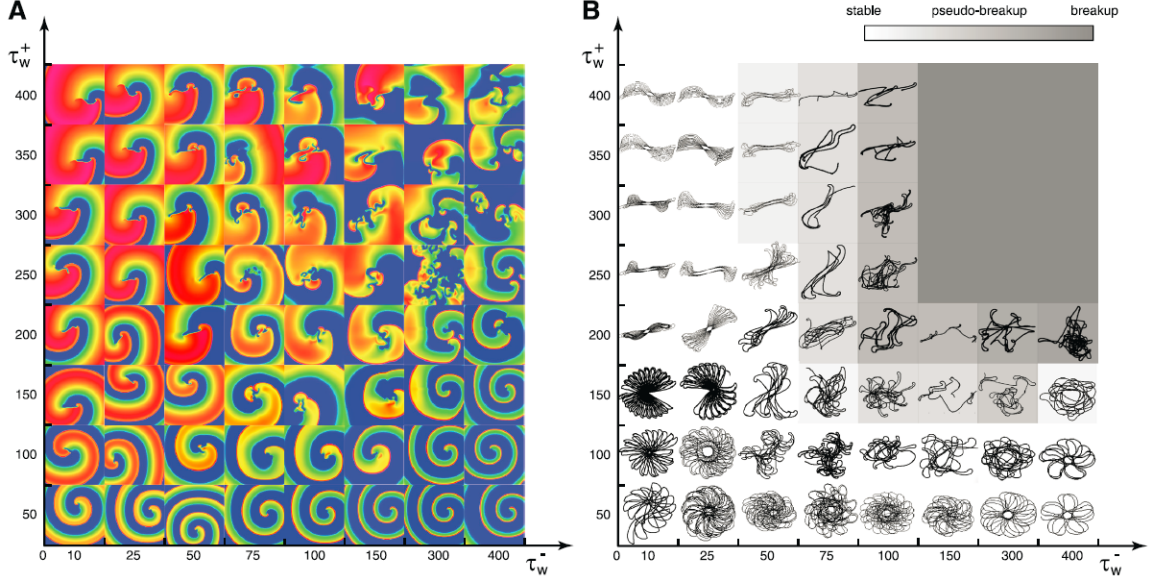


Figure 5.4: Snapshots of spiral waves and their corresponding tip movements when τ_w^+ and τ_w^- varied. Adopted from Bartocci et al.¹⁸

spiral waves, the tip of the spiral is almost fixed. For that to take place, a tissue with high excitability together with minimum effective refractoriness dispersion is needed so that spiral tip will be able to make fast turns without colliding the areas which are still refractory. Accordingly, τ_{fi} is kept at a small value in order to increase the excitability and other parameters varied to have varying WL and periodicity values. It should be noted that an absolute stationary of the tip is not possible. Furthermore, it was shown that electrical rotors in human atria can precess in a periphery of 2-3 cm^2 [Narayan et al.³¹]. Hence, using a similar approach as in [Davidenko et al.²⁵], the spiral wave is considered stationary when the tip remains in a bounded trajectory such as circular or cycloidal and confined in a circle whose diameter does not exceed 1 cm and periodicity is uniform outside the circle.

For meandering, however, the tip of spiral moves around. Several factors are shown that contribute to the meandering tip mechanism through the studies using either the insight from general excitable media and computer models [Winfree¹⁷⁸, Kogan et al.¹⁷⁹, Kogan et al.¹⁷⁹] or isolated cardiac muscle [Pertsov et al.¹⁸⁰, Ikeda et al.⁶⁹, Gray et al.¹⁸¹]. In general, it is pre-imposed by the excitation and recovery rates intrinsic to the underlying tissue. In the present study, τ_w^+ , τ_w^- , τ_{si} ,

Table 5.1: Parameter Analysis of MRM

Time Constants	Description	Effect of the Increase
τ_w^+	To inactivate the slow inward Ca^{2+} current	Plateau duration increases since inactivation takes longer therefore APD and WL increase.
τ_w^-	To recover from inactivation of the Ca^{2+} current	Time to recover from the inactivation increases hence the plateau duration for the subsequent APDs varies for longer APDs leading to increased APD dispersion.
τ_{fi}^+	For the fast inward Na^+ current	During depolarization, the amount of Na^+ current inflow decreases therefore the excitability of the tissue becomes lower.
τ_{si}^+	For the slow inward Ca^{2+} current	The smaller Ca^{2+} current and the shorter APD and WL.
τ_{so1}^+	For the slow outward K^+ current during repolarization	The smaller effective K^+ current and the larger APD and WL.

and τ_{so1} are varied in order to change the relative activation-recovery rates and effective refractory dispersion properties of the tissue whereas τ_{fi} is particularly changed to decrease the excitation so that the tip meanders more during making a turn.

In case of breakup, the spiral wave is fragmented. A multiplicity mechanisms that can produce spiral breakup and alternans are investigated and posited [Fenton et al.¹⁴⁹, ten Tusscher and Panfilov¹⁸²] including steep APD restitution curve [Nolasco and Dahlen¹⁴⁴, Guevara et al.¹⁴⁵, Karma¹⁴⁶, Koller et al.¹⁴⁷, Qu et al.¹³⁵], APD and CV restitution dispersion [Banville and Gray¹⁸³, Pak et al.¹⁸⁴], super excitability [Giaquinta et al.¹⁸⁵], lateral instability [Marée and Panfilov¹⁸⁶]. Furthermore, it was shown that intrinsic tissue dynamics can lead to breakup without heterogeneities [Panfilov¹⁸⁷]. Here, the selected parameters are varied as to increase the tissue excitability and effective refractory dispersion so that the tip will make fast turns, collide on its waveback and eventually lead to fragmentation. Consequently, τ_{fi} is varied at smaller values in order to increase the excitability, τ_w^- is varied in relatively higher values in order to increase effective refractoriness dispersion and remaining parameters varied to result have varying WL and periodicity values. A delineation on generating spiral behaviors under each category by varying parameters of MRM can be found in

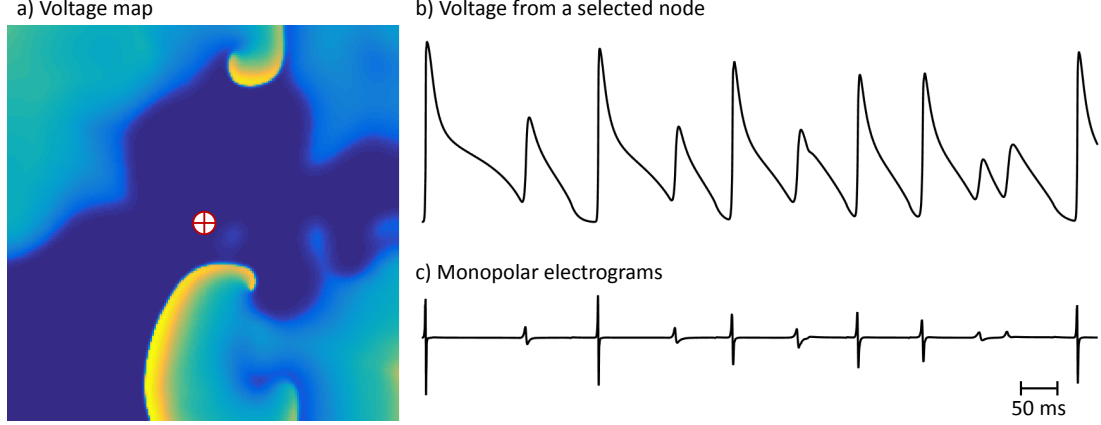


Figure 5.5: An example that represents the simulation of monopolar EGMs (c) with respective APs (b) through simulation of a spiral wave breakup on a 2D patch of $10\text{cm} \times 10\text{cm}$ (a) for which parameter set EKF (see Table B.3) with $\tau_w^+ = 250$, $\tau_w^- = 250$, $\tau_w^- = 140$, $\tau_{fi} = 0.05$, $\tau_{si} = 20$, and $\tau_{so1} = 50$ is used. Readings are taken from the center of the patch which is shown with a red marker.

Appendix C. Snapshots for each simulated behavior and their respective APs and APD restitution are also provided.

Unipolar EGMs were simulated using a practical approach [Virag et al.¹⁵²] where extracellular potentials are computed as a weighted sum of the membrane potential. The details of EGM simulation is covered in Section 3.3.2. Unipolar EGMs were computed at 1 kHz frequency. Bipolar EGMs are obtained from the difference between neighboring electrodes whose configuration depends on the catheter type used. An example of simulated unipolar electrograms with the corresponding membrane potential is shown in Figure 5.5. The effect of alternans on the morphology of monopolar electrograms as variations in the magnitude and negative and positive deflection ratios can be observed.

In EGM measurement setup during simulation, a star (PentaRay) and a circular (Lasso) shaped catheters were mimicked. They were positioned at different locations on the grid to test the effect of regional difference on segregating simulated behaviors. Figure 5.6 shows a delineation of simulation and data handling setup where an example of a simulated meandering spiral wave, star shaped catheters placed at 5 different locations, and some parts of simulated unipolar intra-cardiac EGM

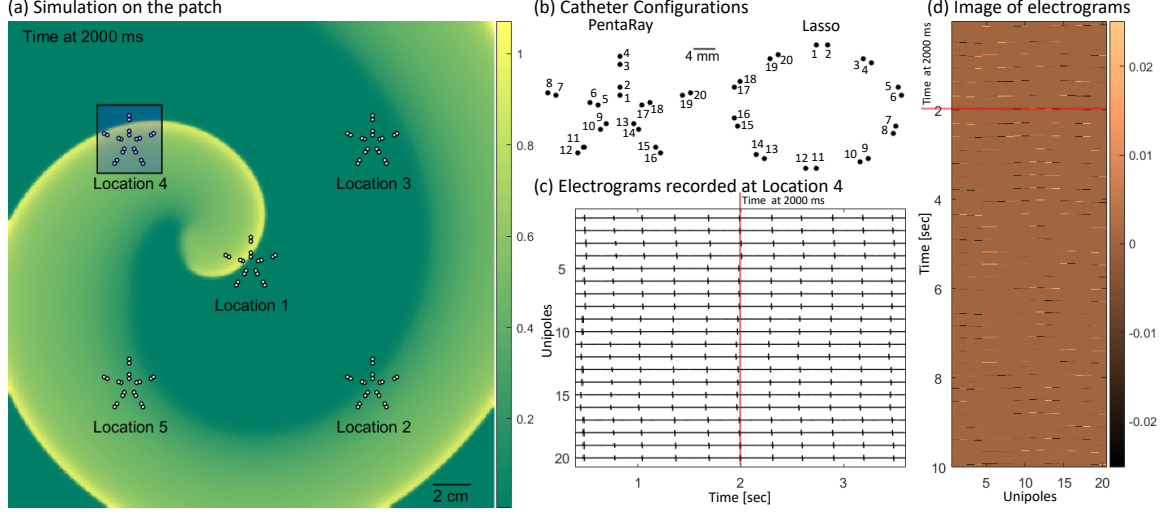


Figure 5.6: Delineation of simulation and electrogram recording setup and data handling. (a) Snapshot of a meandering spiral wave simulation on the 25.6 cm x 25.6 cm grid. The locations catheters positioned (in this case only the spiral shaped catheter) are also shown. (b) A close view on modeled catheters displaying electrode positions and configurations. (c) Unipolar electrograms recorded at Location 4. (d) Recorded unipolar electrograms represented as a digital dataset as being stacked columnwise to form a matrix and being converted to image.

signals measured from *Location 2* is displayed. As shown in Figure 5.6B, the length of a single branch of the star shaped catheter is 16 mm, each having four electrodes with the spacing between them is 242 mm. The circular shaped catheter has a radius of 16 mm. The distance between neighboring electrodes is approximately 2 mm. Total electrode numbers for each catheter is 20. The number of bipolar readings in both catheter is 10. Each simulated behavior for a particular measurement protocol is represented as a set of vectors:

$$S = \{\Gamma_1, \Gamma_2, \Gamma_3, \dots, \Gamma_N\} \quad (5.1)$$

where γ_i is a $M \times 1$ time vector representing the EGM signal recorded either from a unipole or a bipole channel i . Since simulations have in general shown transient behaviors during initial period of times, first 2.5 s in the simulations were excluded from vector representation. Consequently, each γ_i became a time vector of a 7.5 s duration. Since EGM signals are recorded in every 1 ms, M is 7500 for each channel. N is the total number of channels on both catheters which is typically 20

and 10 in case of unipolar and bipolar readings respectively. Thus, each simulated behavior for a particular measurement protocol is represented by a $M \times N$ matrix.

5.2 Normalized Compression Distance

NCD is a universal feature free, parameter free, and a normalized version of information metric [Cilibrasi and Vitanyi³⁷]. Its mathematical background is based on Kolmogorov complexity theory which briefly states that complexity of a string is scaled with the length of the shortest possible description of it. Using that principle, an information metric can be assessed between two objects. Hence, the distance between two objects is associated with the length of the shortest possible description that can be ascribed to one given the other. This is the idea behind normalized information distance (NID) and it reads as

$$NID(x, y) = \frac{\max\{K(x | y), K(y | x)\}}{\max\{K(x), K(y)\}} \quad (5.2)$$

where $K(x)$ is the algorithmic information of x and $K(y | x)$ is the algorithmic information of x . The information represented by $K(\cdot)$ is absolute, therefore in practice it can only be approximated by a real world compressor as it is done when performing NCD. The NCD between two objects therefore reads as

$$NCD(x, y) = \frac{C(x, y) - \min\{C(x), C(y)\}}{\max\{C(x), C(y)\}} \quad (5.3)$$

where $C(\cdot)$ is a compression operator, $C(x)$ is the file size (in bit length) of the compressed object x and $C(x, y)$ is the file size of the concatenated objects x and y . It follows from Equation 5.3 that NCD is between $[0, 1]$. As similarity between the two objects increases, it results values closer to 0 and vice versa.

Various compressor types with different compression algorithms can be used such as Lempel-Ziv based dictionary (gzip), block based (bzip2), image based (JPEG) or statistical (PPMZ). It was shown for some applications that the method is robust to the change of underlying compressor type used [Cebrián et al.¹⁸⁸]. In this study, mainly bzip2 was used as the compressor which includes the

Burrows-Wheeler transform on its underlying compression algorithm [Burrows and Wheeler¹⁸⁹]. In some cases, *gzip* and *JPEG* were used as well for comparison purposes.

Since NCD is a feature-free and parameter-free technique, it does not require to extract features in order to get a distance measure. It works on any object as long as it is in a file format compatible with the compressor used. In this study, the set of EGMs represented by a matrix was converted to a *bmp* image format which works under all compressors used here. An example of a resulting image is illustrated in Figure 5.6d. In this way, the data was introduced to the compressor as an image file. The steps taken through obtaining a distance measure for a measurement configuration was demonstrated in Figure 5.1.

5.3 Normalized Compression Distance with Feature Bias

The assertion stating NCD to be feature-free does not represent an absolute freedom because dominating feature(s) shared between the objects is implicitly effective in the compression algorithm therefore in the assessment of the distance. However, there is no bias on the selection of the features as far as input to compressor algorithm is concerned. In contrast to this, bias is herein provided to NCD by selecting certain features when introducing the objects, the EGM sets, to NCD scheme. Basically, instead of using set of raw EGMs, a subset of features extracted from EGMs are used. This is implemented in two ways: First, a subset of features such as list of cycle lengths (CLs) and list of EGM morphology indices are extracted and represented to the compressor in NCD scheme. Second, certain features are implicitly used through a reformulation of NCD scheme where compressor $C(.)$ in Equation 5.3 is replaced by an operator that maps the original signal into that feature domain. The details for both approaches are covered next.

Presentation of Features to NCD Formulation: It is known that an EGM signal is composed of the principal attributes as morphology, periodicity and phase. Here we extract parameters related to morphology and periodicity for which a spike detection algorithm is needed. It is important to note that only unipolar readings are considered in this part as a different algorithm might be needed to extract features in question in case of bipolar readings. For this purpose, a nonlinear energy operator

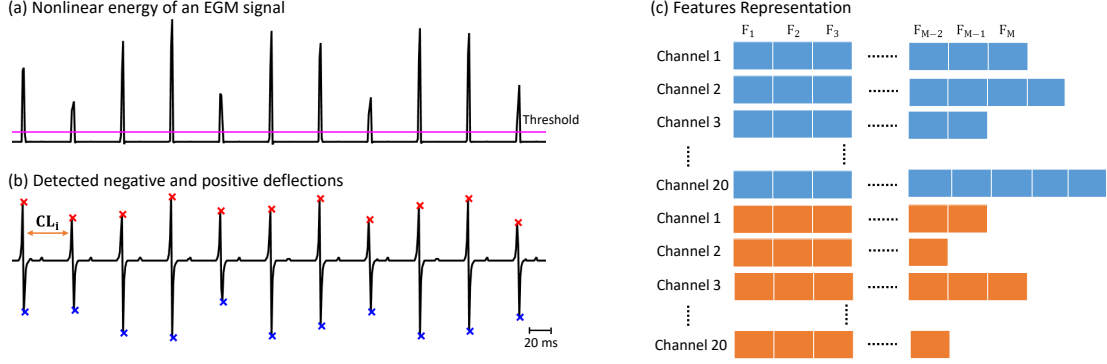


Figure 5.7: Unipolar EGMs spike detection. Nonlinear energy of the signal is derived first (a), then negative (blue x-mark) and positive (red x-mark) deflections are detected (b) which are used to extract CL and EGM morphology parameters. After extracting features, they are tiled into respective unipole channels and the channels are then stacked vertically as shown in part (c). Note that the length for each channel together with for each simulated behavior can vary since number of resulting features is not fixed for each case. Also features represented in this paper are either CLs or EGM morphology indices or consecutive addition of both. Any of two behaviors are concatenated vertically as shown in part (c).

of the EGM signal proposed at [190] was used. Then a threshold is determined and time instances where the threshold is first passed are detected. Then a time window of 10 s was considered in the barycenter of each detected time instances and maximum and minimum values and corresponding time indices are detected, thereby positive and negative deflections were obtained. This process is visualized in Fig. 5.7 (a,b). Consequently, CL and EGM morphology indices were computed. Former was computed with the difference between consecutive positive deflections and the latter was computed the same way as in [122] by dividing difference of positive and negative deflection with total amplitude. Once again, the features are represented as a set of vectors:

$$\Sigma = \{\Phi_1, \Phi_2, \Phi_3, \dots, \Phi_N\} \quad (5.4)$$

where Φ_i is a vector containing list of features can be of varying length for each channel i and for each simulated behavior. Hence, it cannot be considered as a matrix. Feature representation for an arbitrary case is depicted in Figure 5.7 (c).

Reformulation of NCD: Higher representation of a time series data such as FFT and wavelet decomposition provides intrinsic periodicity information. To get use of this, we obtained the distance using FFT which is essentially reformulation of Eq. (5.3) as pointed previously where information of the signals is represented by measures in frequency domain. The distance which is called NFFTD is now defined as:

$$NFFTD(x, y) = \frac{\|F(x, y)\| - \min\{\|F(x)\|, \|F(y)\|\}}{\max\{\|F(x)\|, \|F(y)\|\}} \quad (5.5)$$

where $F(\cdot)$ is the FFT operator and $\|\cdot\|$ is the norm-2 operator. Also, $F(x, y)$ represents FFT of concatenated signals. In above formulation, compressibility $C(\cdot)$ is replaced with $\|F(\cdot)\|$.

5.4 Clustering

5.4.1 Spectral Clustering

Once the distance between simulated behaviors were obtained, the behaviors are clustered first using spectral clustering method [191]. Specifically distance matrix can be mapped to the spectral domain where eigenvector analysis can give further information about the data. First, data affinity matrix, or item-item similarity matrix, is calculated based on the distance values between the items and a free scale parameter and can be read as:

$$A_{ij} = e^{-d(x_i, x_j)/2\sigma^2} \quad (5.6)$$

The steps below adopted from [192] are as followed:

For spectral representation:

1. Form the affinity matrix A .
2. Construct D by summing rows of A in diagonals of D where: $D_{ii} = \sum_j A_{ij}$
3. Form N by symmetric divisive normalization: $N = D^{-1/2}AD^{-1/2}$
4. Find the n largest eigenvectors of N which are x_1, x_2, \dots, x_n and form the matrix $X = [x_1, x_2, \dots, x_n]$

For clustering:

1. Cluster into k-means
2. Assign the labels

When number of the largest eigenvectors, n , is chosen to be less than 3, the groupings can be displayed on a graph enabling visual representation of the distance matrix. In this study, n is set to 3 as σ is set to 0.75.

5.4.2 Cluster Analysis

Gap Statistics: Gap statistic is presented to automatically assign the number of clusters by comparing them to random data generated by a uniform distribution [Tibshirani et al.¹⁹³]. The sum of distances within each cluster r is defined as:

$$D_r = \sum_{i,j \in C_r} d_{i,j} \quad (5.7)$$

The summation of intracluster distances across all k clusters then reads as:

$$W_k = \sum_{r=1}^k \frac{1}{2n_r} D_r \quad (5.8)$$

The gap statistics is then the difference between intracluster distances of the data and the intracluster distances of B randomly generated uniformly distributed reference data

$$Gap(k) = \frac{1}{B} \sum_{b=1}^B \log(W_{kb}) - \log(W_k) \quad (5.9)$$

The simulation error for generation of B is defined as:

$$s_k = \sigma_k \sqrt{1 + 1/B} \quad (5.10)$$

where σ_k standard deviation of set B . Then, optimal cluster number k is chosen as the smallest

value for:

$$Gap(k) > Gap(k+1) - s_{k+1} \quad (5.11)$$

Jaccard Index: Jaccard index (JI) as an external cluster validity criterion compares similarity and diversity between sample sets. It measures similarity by dividing the size of intersection divided by union of the samples:

$$J(X, Y) = \frac{|X \cap Y|}{|X \cup Y|} \quad (5.12)$$

Normalized Mutual Information: Normalized mutual information (NMI) can be expressed as:

$$NMI(X, Y) = \frac{H(X, Y) - H(X | Y) - H(Y | X)}{\max(H(x), H(y))} \quad (5.13)$$

where $H(X, Y)$ is joint entropy, $H(X | Y)$ and $H(Y | X)$ are conditional entropies. Also for both JI and NMI, X and Y represent initial and estimated labels, respectively.

5.5 Classification

After the distance matrix is created, k-NN algorithm is used for classification. Classification accuracy is then measured using 10-fold cross validation. The dataset is portioned into 10 non-overlapping subsets. In each fold, 1 subset is used for testing and the rest is used for training, resulting in classification of all behaviors after 10 folds. The whole process is repeated 500 times with ordering of data points are randomly permuted each time. Finally, an average classification rate with a confidence interval is obtained.

Part III

Results and Discussions

Chapter 6: Results: Reduced Order Cardiac Modeling

In Chapter 4, methods for parameter estimation of MRM to fit APs as an output from CRN were covered. In this chapter, the results of parameter estimation schemes for different electrophysiological behaviors are discussed.

Remainder of this chapter is organized as follows: In section 6.2, analysis of parameter estimation scheme using EKF is carried out. In section 6.2, the fitting results for heterogeneous APs of each estimator are presented. In section 6.3, for each estimator, the fitting results for AP of Afb based electrically remodeled atrial working myocardium are presented.

6.1 EKF Analysis

In this section, parameter estimation incorporating EKF is first tested under different noise models. Different noise profiles are created by varying magnitudes of measurement and process noise covariance and ratios of process to measurement covariance.

The first attempt is to discover the most effective regime of noise definition provided to EKF for the parameter estimation problem. Since there is a certain amount of stochasticity in estimation of the parameters, different results under same initial conditions is obtained. Hence, in order to make a more robust comparison of EKF performance under different noise definitions, the seeding of random number generator in MATLAB is fixed. The comparison includes here different measurement and process noise covariance values. Specifically, R and α (equal to Q/R), values are varied. Prior estimation covariance matrix P_k^- is always initialized to Q . Both integration and observation time steps, Δt and dt , are set to 0.1 ms. In this part, an AP train of 4 beats with CL of 250 ms is considered only. After each simulation, the minimum values for AP, RC fitting and their average NRMSEs are chosen. Note that each of them does not have to happen at the same iteration.

The results are displayed in Figure 6.1. In general, fitting performance for AP decreases as estimation covariance increases. However, AP fitting performance increases as Q/R increases. A

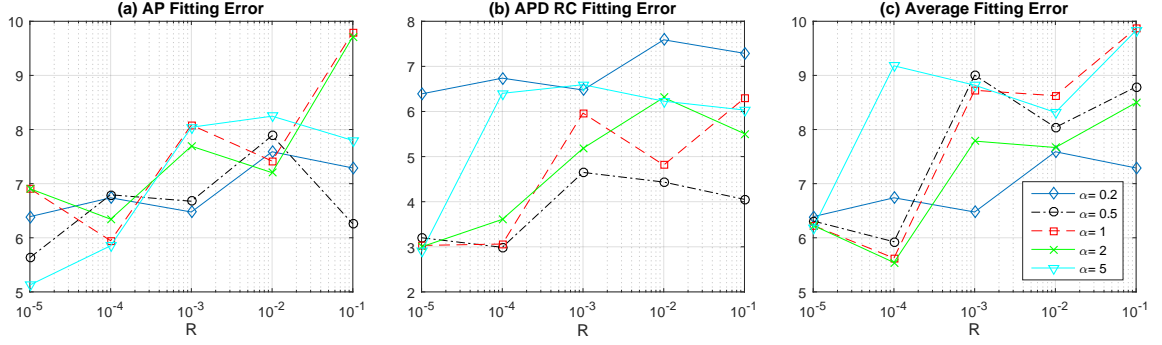


Figure 6.1: Goodness of fitting comparison for EKF under different magnitudes of measurement and process noise covariances.

same observation goes for RC fitting as well as average fitting. According to these results, an optimal selection for noise model appears to be smaller R values with greater α values.

Another observation is that goodness of fitting overall increased during early repolarization and plateau phase of a typical AP. This can be seen in Figure 6.2 where error values for AP, RC and their averages get smaller during these periods. The observations lead to following underlying mechanism: There is a moderate value in the estimation error, also called residual or innovation, which implies a moderate priori estimation error covariance and therefore a moderate Kalman gain from the relation in Equation ???. Since detectability and reachability of the system also increased around there, Kalman gain matrix with increased number of nonzero elements arises and it leads to a fine tuning of parameters of the model. On the other hand, in the late repolarization and resting phase of AP where fitting performance typically deteriorates, the residual is too big and reachability and detectability is smaller. Therefore, Kalman gain matrix with few number of nonzero elements arises and causes dramatic changes in fewer parameters.

The results obtained confirm that EKF does not find the global minima as it tends to find the closest local minima. This is expected since it does not promise optimal state estimation when the system is nonlinear. An important aspect arises from the results is that whenever a certain amount of excitation is introduced to the EKF implementation such as increase in the ratios of process to measurement covariance or a moderate increase in the difference between measured and estimated

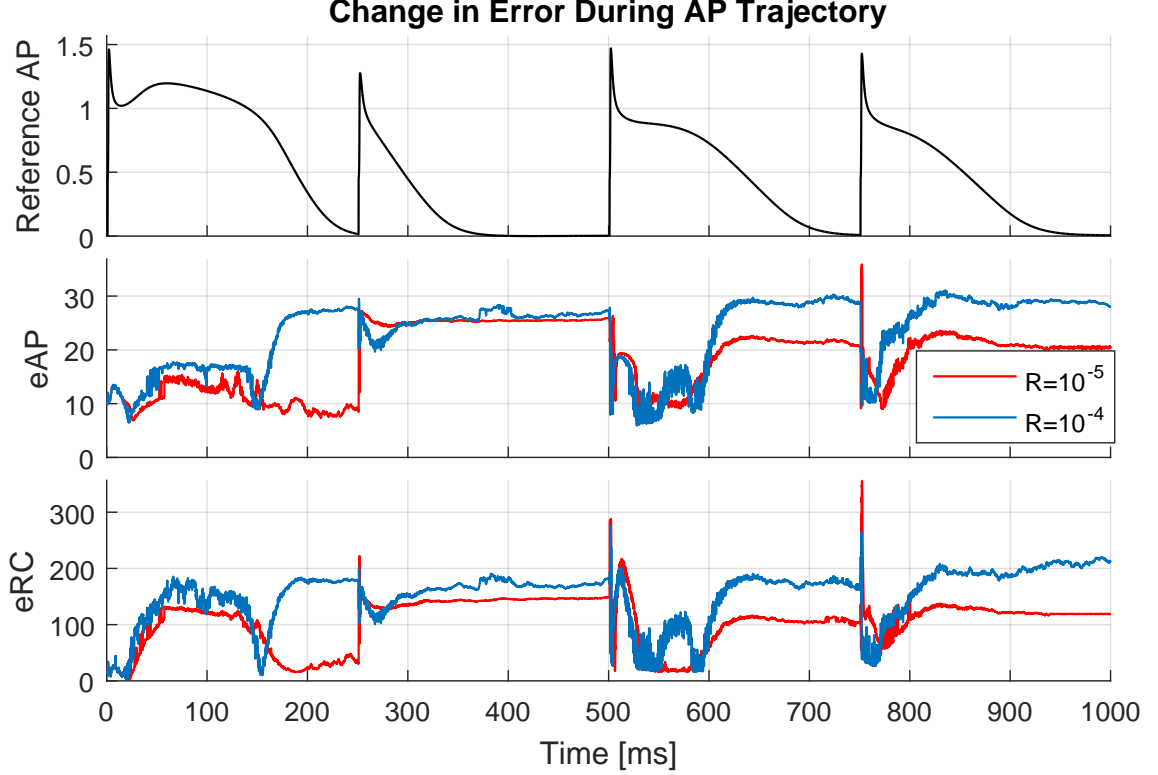


Figure 6.2: Change in error values over the course of EKF implementation.

output, there we usually observe improvement in the goodness of fitting. From this, we can infer EKF as a model training tool as well. That is, the more challenging tasks were given, the more configurations of the model variables are disclosed hence the model learned more through EKF.

Although a Grammian reachability or detectability analysis is not performed on the system, it can be seen from the change in Kalman gain vector and therefore the changes in the parameters from their initial values, the system is not fully observable anywhere during the course of a typical AP. Therefore, EKF actually optimizes some of the parameters. Those parameters are found out by inspection which are: u_o , u_u , θ_v , τ_v^+ , u_w^- , τ_{fi} , τ_{so1} , τ_{so2} , k_{so} , u_{so} , τ_{s2} , u_s , τ_{si} , $\tau_{w\infty}$, and w_∞^* . Yet, few parameters are shown to be enough to adapt the MM to reproduce different AP and APD restitution properties. We can also infer that we eliminated redundancy in the number of parameters to be optimized. It is obvious that there are more than one parameter to change certain AP and restitution properties in a phase. For instance, there are several parameters that play role

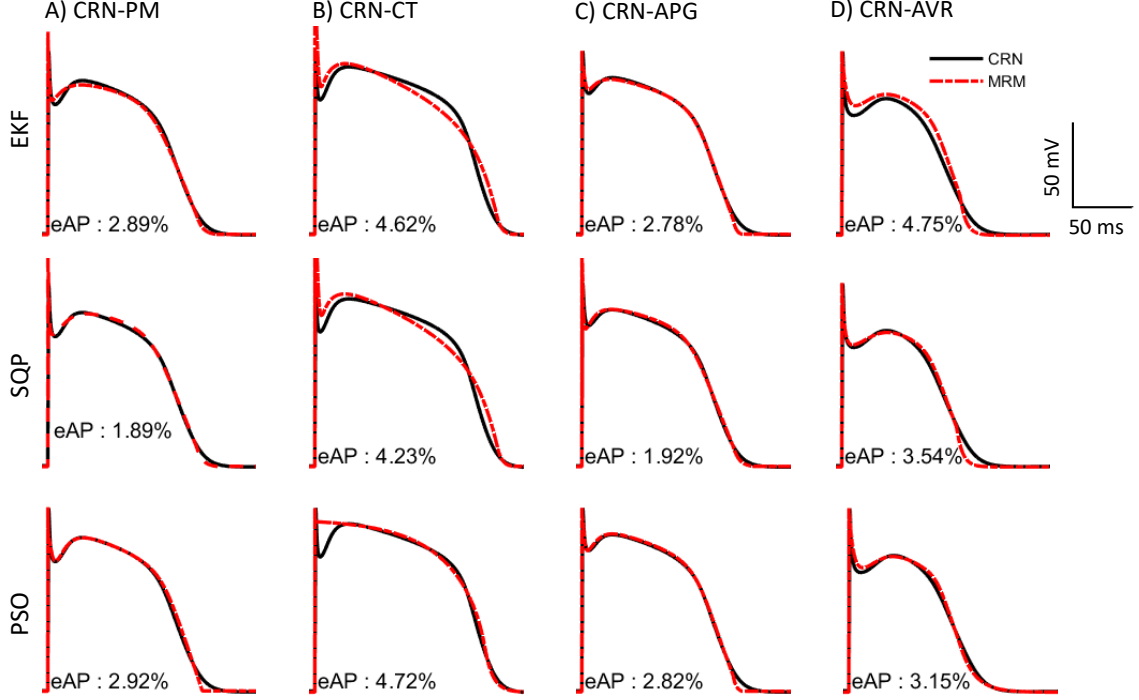


Figure 6.3: Fitting results of heterogeneous APs throughout human atria through the estimation schemes EKF, SQP, and PSO. For each case, NRMSE of AP is evaluated.

on shortening or increasing APD. Hence, fewer number of parameters may suffice to tweak the model as demonstrated here.

6.2 Heterogeneous Action Potential Fitting

Parameter estimation algorithms EKF, SQP, and PSO are used to reproduce AP morphology of different cell types from heterogeneous structure of atria. As covered in section 4.2, cell types are classified into: PM, CT, APG, and AVR regions. For each region, cells are considered to be in sinus rhythm.

In each case, a single cell is modeled in CRN and stimulated to result AP. In order to achieve a steady state of APs, each cell is paced at a CL of 600ms for 4 times and only the last AP was considered for matching. An initial parameter set is required for each estimator. In case of PSO, a randomized parameter values within a defined interval for each (see Appendix B) is used. As pointed in section 4.3.3, the best result out of 100 implementation is chosen for PSO scheme. The

initial parameter set used in the best result is then used for SQP and EKF schemes as well.

The matching results for each atrial region and estimation scheme are provided in Figure 6.3. In general, better fitting performance is obtained from SQP scheme than that of EKF and PSO schemes. An explanation can be provided on account of underlying algorithm used for each scheme. In PSO, candidate parameter values are randomly assigned at each iteration with a guidance of previous knowledge, hence convergence for error minimization depends on randomness and the history. In EKF, both system dynamics through Jacobian matrix evaluated and randomness through the noise introduced at each filtering step are effective. In SQP, the system dynamics are involved through Hessian matrix where gradients of parameters play in. This suggests that the direction towards a local minima is more likely to be stochastic in case of PSO, driven with parameter sensitivity in case of SQP, and partially stochastic and driven with parameter sensitivity in case of EKF. Therefore, from an initial point, it is more likely to find a better local minima through SQP scheme. However, this may not happen all the time given that random changes in the search direction may lead to a better local minima. Likewise, a better fitting result is achieved with PSO in case of AVR AP matching. Note that, for each of the algorithms, there is always a likelihood for better local minima since global ones are not guaranteed due to nonlinearity. In case of atrial regions, APs of CT and AVR yielded a lower fitting performance. This is believed to be due to complex early and late repolarization dynamics present in the APs of cells in those regions.

6.3 Electrically Remodeled Action Potential Fitting

In this section, Afib based electrically remodeled cells of atrial working myocardium (i.e. PM) is targeted to match. As covered in section 4.2, Afib-AP is modeled in CRN with modifications on some of the ion channel conductances. Once again, 4 consecutive stimuli protocol is applied. This time, multiple stimuli protocols with different CLs (e.g. 200, 250, 300, 400, 600 *ms*) are considered and a matching is performed for each. In addition, a dynamic stimuli protocol where the cell is paced at varying CLs (e.g. 700, 550, 400, 340, 280, 220 *ms*) in a single protocol.

Resulting NRMSEs for each case is displayed in Figure 6.4. For a more comprehensive indication of fitting performance, NRMSE of AP and APD standard RC and average NRMSE of both are

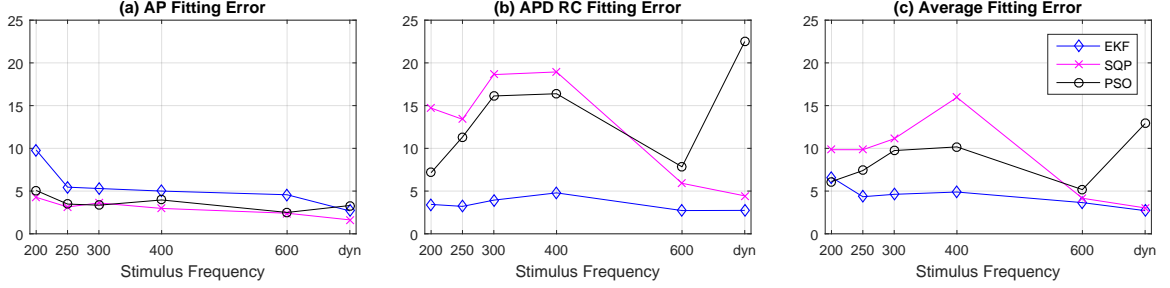


Figure 6.4: Goodness of fitting comparison for EKF, SQP, and PSO.

computed. Again, SQP in general results in the best AP morphology fitting performance. However, once APD standard RC matching is considered, EKF noticeably outperforms other schemes. Same thing is valid for average NRMSE. AP and RC fitting for each estimator in case of dynamic pacing is graphically represented in Figure 6.5. As can be seen, in PSO, a good matching is achieved in earlier phases of AP except during the late repolarization phase. Since that portion occupies a negligible place in the course of an AP, a discrepancy takes place there may not quantitatively impact the goodness of fitting. However, as there exists a significant change in characteristics of RC, the impact can be greater in terms of AP dynamics. Conversely, although AP morphology fitting in case of EKF results in a rather lower performance due to discrepancy in plateau phase, RC fitting yields the best approximation. Another observation is that restitution matching remains poor during constant stimuli for SQP whereas it dramatically increases during dynamic stimuli. This is due the fact that a dynamic stimuli is a better representative of restitution portrait than only constant stimuli. In fact, the same pattern is not observed during PSO as expected since system dynamics are not incorporated.

These findings suggest that evaluation of RC is particularly important since reproduction of AP alone is not enough to validate the reliability of the fitting task. APD restitution incorporates refractoriness response of a tissue to different pacing protocols representing a good summary of tissue dynamics. Topologically speaking, a mapping from AP morphology to restitution curve is many-to-one. That is, more than one APD RC can result in similar APD morphology whereas the opposite is not true. An example of this is shown in Figure 6.6.

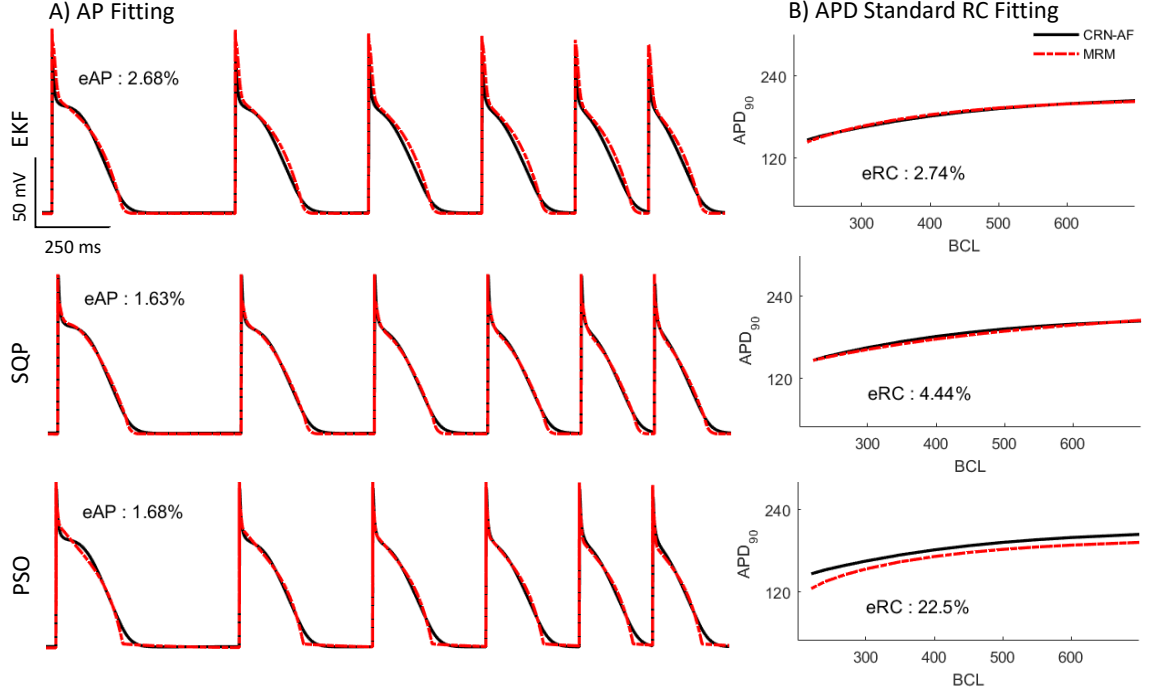


Figure 6.5: Fitting results for matching train of APs resulted from dynamic pacing of an Afib based electrically remodeled cell. Fitting performance is compared through the estimation schemes EKF, SQP, and PSO. In each case, NRMSEs of AP and APD Standard RC are simultaneously evaluated.

Further testing of estimated parameters obtained with AP waveform matching under dynamic pacing is conducted by means of 2D excitation propagation matching. CV restitution properties are not considered here for evaluation of estimated parameters hence for error estimation. To bridge the gap on this account, a manual adjustment for conductivity rate of MRM in reference to conductivity of CRN is performed. Specifically, a planar wave is delivered from an edge using CRN as diffusion coefficient is set to $\sigma=0.0012 \text{ cm}^2/\text{S}$ and the time elapsed for the wavefront's arrival to the opposite edge is marked (i.e. 380 ms). The same procedure is followed using MRM with each estimated parameter sets except that diffusion coefficient is manually adjusted to a value for each case such that wavefront arrival time will be the same as the marked time. Consequently, a different diffusion coefficient is obtained for each parameter set of MRM. This process together with adjusted diffusion coefficients is visualized in Figure 6.7. Note that although the wavefront conduction velocity is matched, differences still exist in wavelength durations. As can be observed, this is due to waveback

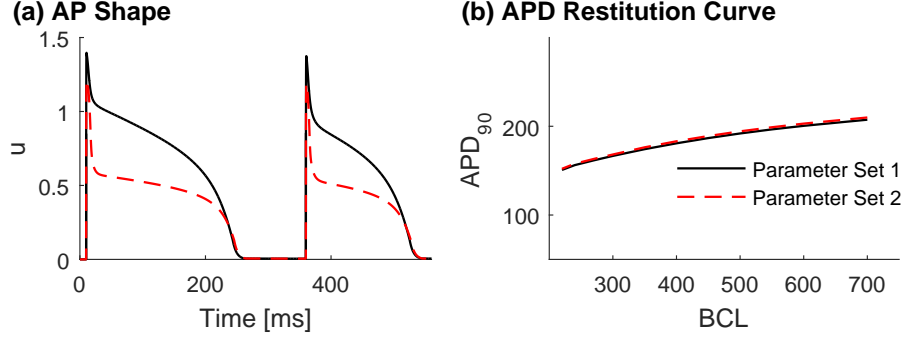


Figure 6.6: An example of different AP shapes obtained from different parameter sets resulting the similar APD standard RC.

conduction velocity mismatch. Two factors can be considered to be responsible for this: First, solely adjusting diffusion coefficient through the mentioned setup is insufficient to match conduction velocity and wavelength. Instead parameters used for AP matching could be used for conductivity matching. In order for their involvement, a larger scale rather than only a single cell is needed. Simulation on a cable can just be enough for that. Second, pacing setup as a single planar wave remains rudimentary since a stimulation protocol as in the form of multiple planar waves at different frequencies as in forming a restitution curve is not used. Another important lesson is that even matching APD RC is not sufficient setting aside matching AP morphology, as discussed before, is not enough to represent the electrophysiology completely. More about the limitations is discussed in section 6.4.

Once conductivity rate is matched, spiral wave simulations are performed for comparison. Resulting snapshots from the simulations are visualized in Figure 6.8. As mentioned in section 4.2, cross-field stimulation protocol is applied to initiate the spiral waves. Briefly, a planar wave is initiated from an edge propagating through lateral direction towards the opposite edge. As it is about a halfway through, a second planar wave perpendicular to the first one is initiated. The initial time for all simulations is then set to when the second wave is delivered. Note that because error computation in case of simulation on 2D tissue patch is burdensome requiring voltage intensity comparison throughout all nodes in the grid, in this context, only a qualitative comparison is conducted. It can be observed that the best approximation is achieved through the parameter set obtained via EKF

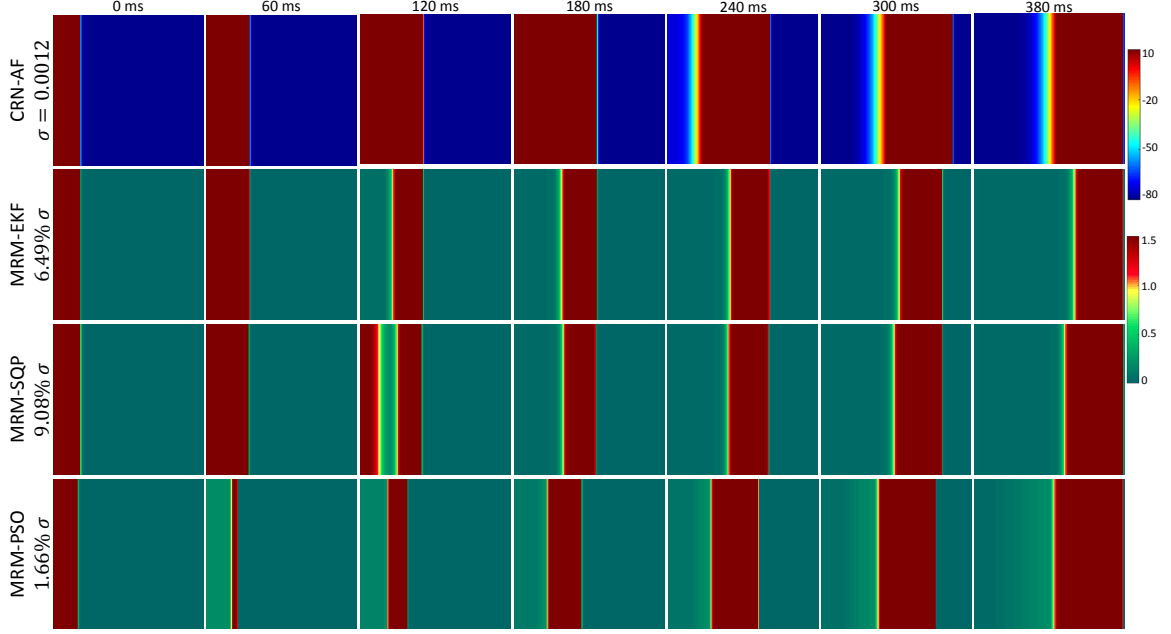


Figure 6.7: Diffusion coefficient adjustment of MRM parameters estimated through EKF, SQP, and PSO for the case of dynamic APs fitting. Diffusion coefficient of CRN, σ , is set as reference conductivity rate for the rest.

scheme which is also called MRM-EKF. In case of MRM-EKF, there are still differences with that of CRN although qualitatively similar spiral behaviors are obtained. The difference in waveback conduction velocity therefore wavelength is manifested in spiral thickness and the tip dynamics. Specifically, waveback propagates slowly in CRN and hence when the tip make a turn, it has to meander more to find a region which is not refractory whereas in case of MRM-EKF it has to meander less. This also makes difference in speed of rotation of spirals as it is faster in MRM-EKF such that during the time 1500 ms spirals in CRN and MRM-EKF made 4 and 6 turns, respectively. It is important to note that although wavefront conductivity rate is matched in case of a single planar wave, it can temporally and spatially differ in case of a spiral since different frequencies are present. MRM-SQP also results in a qualitatively close behavior but not as good as MRM-EKF. On the other hand, very poor matching is obtained using MRM-PSO where spiral breakup is emerged. This is expected given the inaccurate APD RC matching obtained previously. Once again, it is shown that considering AP morphology matching only can even be misleading.

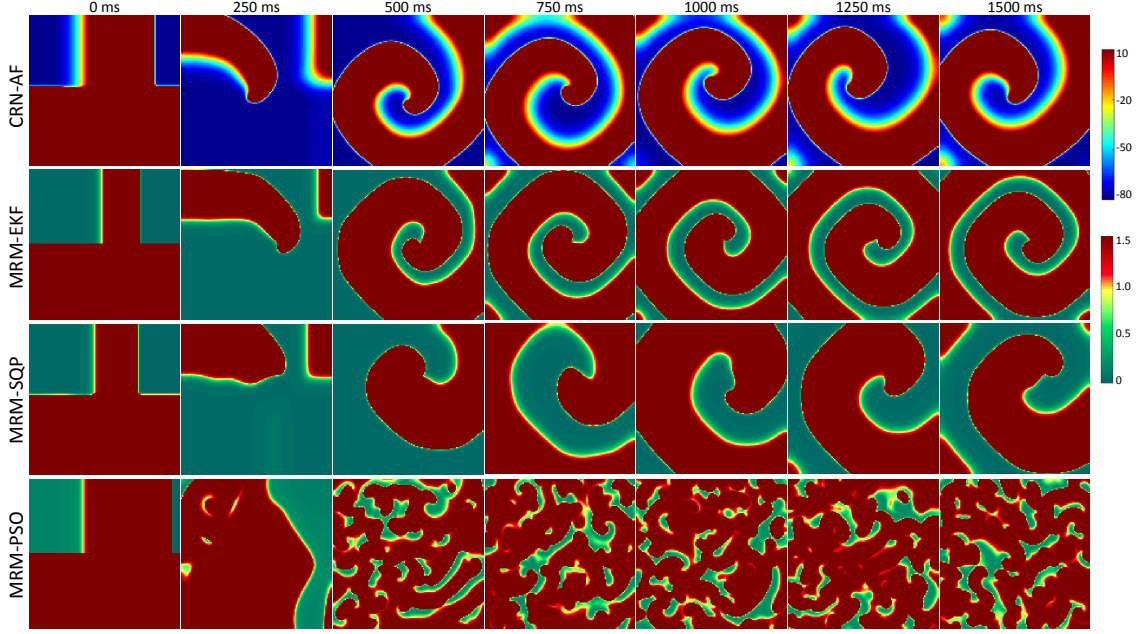


Figure 6.8: Excitation propagation comparison between CRN and estimated MRM parameters through EKF, SQP, and PSO for the dynamic pacing. Spiral waves for each case is initiated using cross-field stimulation protocol. The time for the delivery the second wave is set as initial time and excitation pattern is demonstrated through snapshots from different time instants.

The findings suggest that EKF and SQP are more favorable estimators than PSO for human atrial electrophysiology matching using MRM. This is due the fact that parameter sensitivity with respect to system dynamics is present in the structure of EKF and SQP whereas it is all stochastic in case of PSO. As higher level of electrophysiological dynamics such as restitution properties and excitation propagation on tissue are considered, EKF yields more accurate matching. The mechanism behind this can be explained through two factors: First, besides system dynamics, EKF scheme includes stochasticity. As discussed in Section 6.1, a moderate level of noise can be useful for finding better local minima. Second, the error used in the feedback mechanisms of both schemes are different. Specifically, EKF and SQP use local and global errors, respectively. From the fact that each parameter is in general responsible for a different period of a typical AP, a local error definition can prevent redundant parameter changes.

6.4 Limitations

A limitation in this context can be considered as simulation of AP only on a single cell. In this setup, conduction velocity and hence wavelength matching is neglected. Instead, conduction velocity matching is compensated by only manual adjustment of diffusion coefficient. Although this helps matching wavefront propagation velocity to an extent, it does not provide a full conduction velocity restitution portrait neither does it help matching waveback propagation velocity which involve adjustment of not only diffusion coefficient but also other parameters such as time constants and voltage thresholds. These limitations can be overcome if the simulations are performed on a cable or 2D tissue patch. Since simulation on 2D can be computationally and mathematically costly, a simulation on a cable with a moderate number of elements can be an optimal selection. In case of EKF, for instance, each time the number of cells in a network increases by one, the number of states increases by four.

Generalization of model complexity reduction method can be non-trivial since in this particular study the chosen complex and simple models have strong conceptual link. However, it could be interesting to test this method in other model reduction applications. Another important aspect of this study is to show the effectiveness of MRM for the investigation of Afib mechanisms in clinical environment. Unlike biophysical models, it is easier to analyze and take a systems approach towards. Hence, it is a more practical model when trying to assess individual electrophysiological parameters in case of Afib and improve therapeutic decision making. However, a drawback of it is that although advantage of simplification and ease of analysis is obtained through model complexity reduction, some dynamics can be lost. For instance, memory property of cardiac cell is lost in MRM.

Chapter 7: Results: Simplified Cardiodynamic Tissue Characterization

In this chapter, the results obtained using the methods described in Chapter 5 are discussed. Through forward simulation, 1500 simulations were performed. They were labeled as stationary, meandering or breakup using the criteria mentioned previously in Section 5.1. After the labeling, number of stationary, meandering and breakup behaviors was 500 each. In order to exemplify features/parameters extracted from each behavior, some spectral parameters such as organization - regularity index and dominant frequency together with average CL corresponding to each behavior is demonstrated in Figure 7.1. It should be noted that none of these parameters are included in neither clustering nor classification analyses.

Remainder of this chapter is organized as follows: In Section 7.1 and 7.2, clustering and classification analyses of simulated behaviors is carried out, respectively. In section 7.3, robustness in classification as to test the effect of intra-measurement, inter-measurement protocol variation, presence of noise and heterogeneous behaviors is implemented.

7.1 Clustering Analysis

In this section, spectral clustering is performed to compare the two information theoretical distance measure approaches explained in Sections 5.2 and 5.3. Feature-free approach using NCD was implemented through compressors `bzip2` and `gzip`. Throughout all the tests, only `bzip2` was used when features are represented to NCD scheme. After spectral representation, k-means clustering algorithm was run. Clustering analysis was carried through both JI and NMI. Only measurements taken from the PentaRay catheter placed at *Location 5* (see Figure 5.6) with unipolar readings were considered in this part.

Resulting groupings for each case are displayed in Figure 7.2. The best grouping (JI: 0.96) was achieved in case of EGM signals compressed with `bzip2` under feature-free NCD scheme. Also an automatic number of classes were accurately estimated via gap statistics for this case only. Feature-

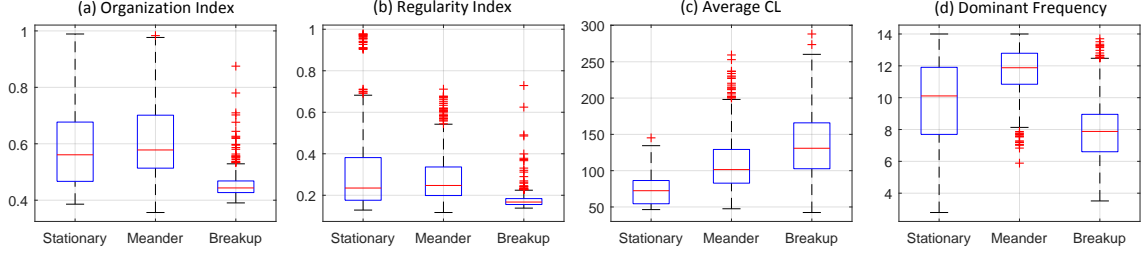


Figure 7.1: Comparison of parameters extracted from unipolar electrograms representing each spiral behaviors. Measurements were taken from the first unipole of PentaRay catheter from *Location 4* of the tissue.

bias approach using NFFTD resulted relatively poor grouping quality (JI: 0.85) as it was even worse in case of using series of CL (JI: 0.61) and EGM morphology indices (JI: 0.57). This suggests that introducing feature bias to the distance measure deteriorates the information captured from EGM signals in comparison to their direct representation as raw time series signals to the compressor `bzip2`. However, as far as clustering results are concerned, the same superiority was not observed when `gzip` is used (JI: 0.70). Another observation within feature-biased approaches is that NFFTD resulted in a better clustering quality than introducing list of CLs to NCD both of which are related to periodicity. This suggests in the present context that for a set of EGM signals, FFT operator comprises of intrinsic periodic properties which is more informative than what only list of CLs represents.

7.2 Classification Analysis

For the distance measure approaches comparison, effectiveness in classification was tested this time. In addition, several compressor types were tried for feature-free NCD scheme since performance of NCD may depend on the compressor used as was observed in the previous subsection. Once again, only measurements taken from the PentaRay catheter placed at location 5 with unipolar readings were used. For k-NN algorithm, 5 nearest neighbor were considered in all cases.

Comparison results are depicted in Figure 7.3 in a boxplot where average classification rate and confidence intervals estimated through the cross validation are displayed. Outstanding classification results were attained through feature-free NCD using compressors `bzip2` and `gzip`. Surprisingly,

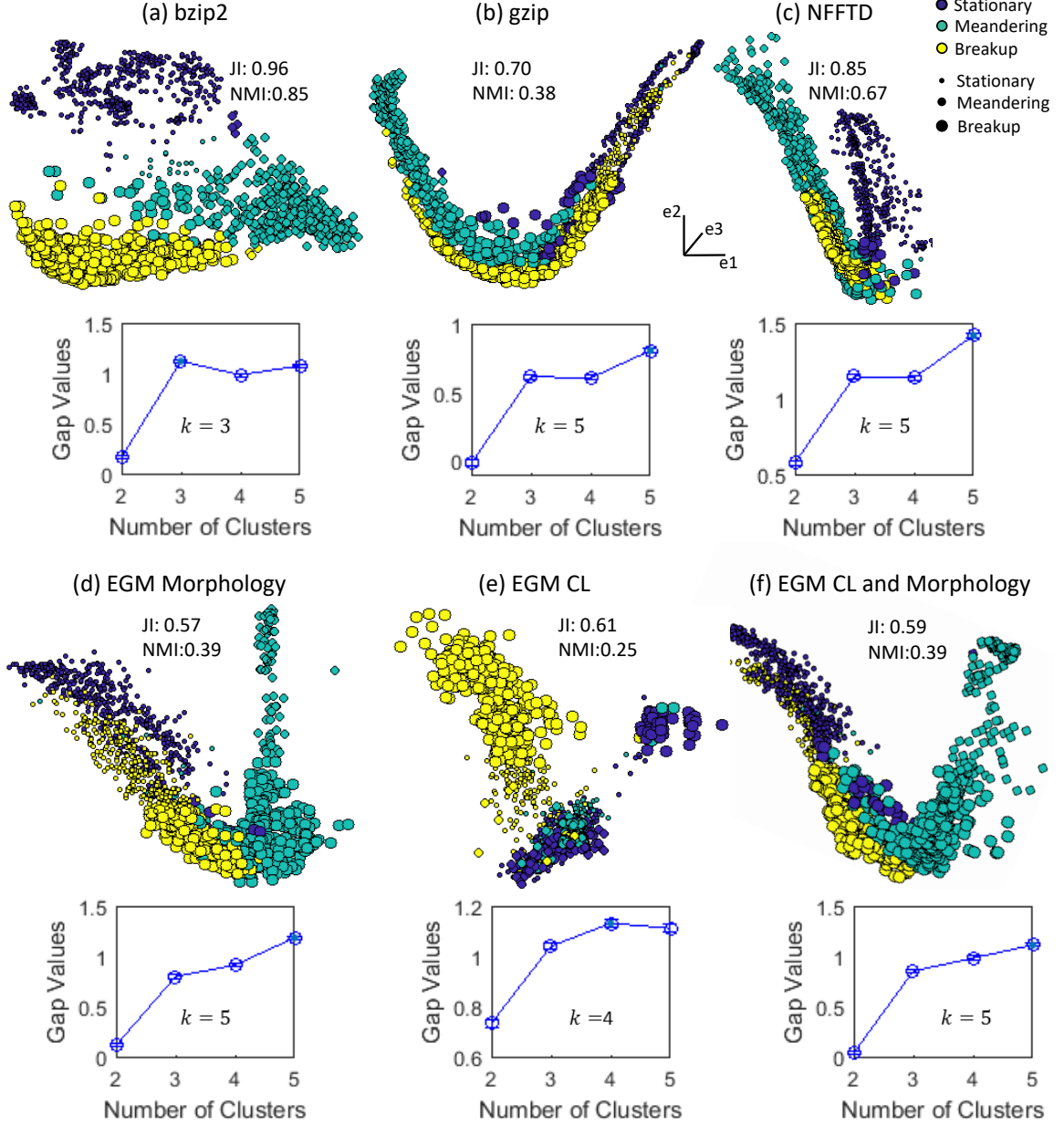


Figure 7.2: Spectral clustering with respective gap statistics for various distance measure assessments using feature-free NCD approach with bzip2 (a) and gzip (b), or using feature-biased approach with NFFTD (c), the series of EGM morphology indices (d) and of CLs (e) or of both (f). Optimal number of classes for each case, k , estimated via gap statistics are put in respective gap value plots. Ground truth and estimated labels are represented with colors and marker sizes, respectively (shown on top-right). Measurements were taken from PentaRay catheter on *Location 5* with unipolar readings. (JI: Jaccard index, NMI: Normalized Mutual Information)

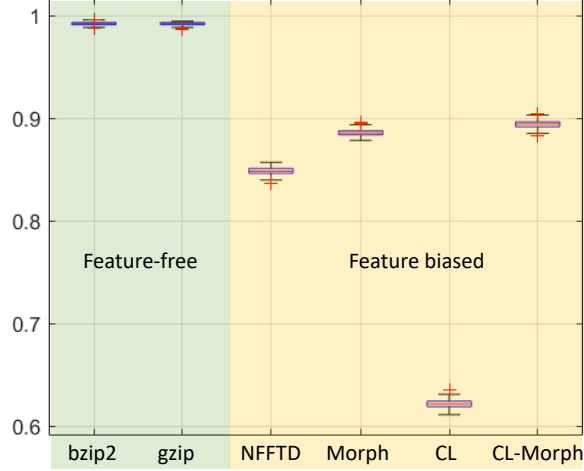


Figure 7.3: True classification rate comparison for different compression techniques. Specifically, featurefree NCD schemes using different compressors and feature-biased distance measure assesment techniques are involved in the comparison.

gzip yielded a dramatically better performance in contrast to poor clustering quality obtained in the previous section. Given the fact that gzip is much faster, it can be considered as an alternative compressor to bzip2 in classification. The image compressor JPEG that performs lossy compression, on the other hand, resulted in a poor classification performance. Similar to the clustering feature-biased approaches in general resulted in relatively poor classification accuracy in comparison to feature-free ones. In contrast to clustering, the list of EGM morphology indices yielded significantly better accuracy in classification. Also, difference between CL and EGM morphology lists in clustering quality was even more pronounced in classification performance. This indicates that EGM morphology index list is a better representative feature of EGM signals than CL list in terms of wave front propagation dynamics characterization. In contrast to observation in gzip, NFFTD yielded poorer performance in classification than k-means clustering. This suggested that the nearest neighbors considered in k-NN algorithm should be greater. In fact, when it was increased to 50, an average classification performance ($\sim 90\%$) was obtained which is closer to JI obtained after k-means clustering. Other than this, classification resulted in better discrimination than clustering for the rest of the cases. In fact, even better classification performance could be attained if optimal nearest neighbor for k-NN was found for each case as opposed to setting it fixed.

Table 7.1: Classification Performance for Measurement Setups

Locations	Catheter Type	
	PentaRay	Lasso
Location 1	UP: 97.46 ± 0.02	UP: 97.80 ± 0.02
	BP: 97.72 ± 0.02	BP: 98.18 ± 0.02
Location 2	UP: 98.93 ± 0.01	UP: 98.81 ± 0.02
	BP: 99.02 ± 0.01	BP: 98.93 ± 0.01
Location 3	UP: 99.39 ± 0.02	UP: 99.23 ± 0.01
	BP: 98.93 ± 0.01	BP: 98.41 ± 0.01
Location 4	UP: 99.53 ± 0.02	UP: 99.24 ± 0.01
	BP: 99.49 ± 0.01	BP: 98.42 ± 0.02
Location 5	UP: 99.23 ± 0.02	UP: 98.76 ± 0.01
	BP: 99.26 ± 0.01	BP: 98.22 ± 0.02

7.3 Analysis of Robustness in Classification

Intra-Measurement Configuration: As shown in Figure 5.6, different measurement configurations are adopted for each simulated behavior. More specifically, their representation is varied over location, catheter type used, and unipolar or bipolar readings. In this subsection, robustness of the classification scheme is tested over these variations. Classification using k-NN algorithm, using 5 nearest neighbors, was performed and classification accuracy was assessed using cross validation.

The resulting average classification accuracy in percentage together with confidence interval is shown in Table 7.1. An outstanding classification rate was overall achieved with considerably small standard deviation which suggests robustness of accuracy across permutations. The performance for varying measurement setups such as catheter type used, the location they were placed, and unipolar or bipolar reading did not result a pronounced difference. It was observed, however, readings on *Location 1* (see Figure 5.6) where generally the tip of spiral wave was located resulted in slightly lower performance comparing to other locations. This is believed to be due to occasional electrotonicity that causes unexcitedness therefore indistinct spikes on EGM signals measured on the region in question.

Inter-Measurement Configuration and Noise: The behaviors within the same location and time period were compared without considering noise. In a practical sense, however, the dynamic

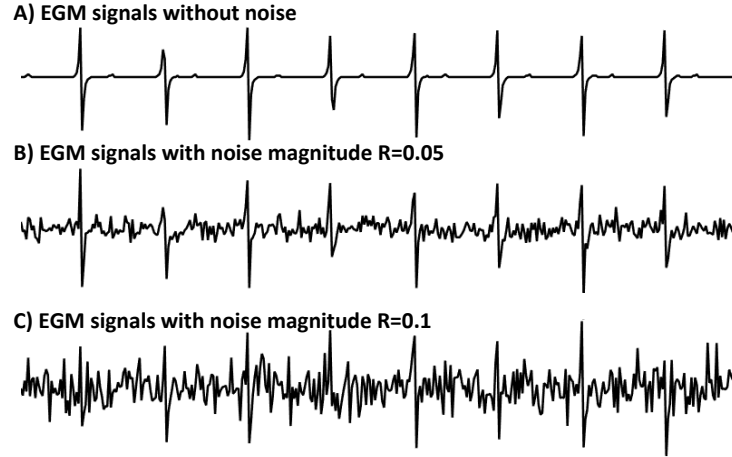


Figure 7.4: Display of effect of noise on a piece of unipolar EGM signal.

nature of electrical wave front propagation in cardiac tissue might not allow the same set of conditions. Additionally, clinical data is usually noisy. Therefore, for the classification to be robust, it should yield the same information even when the conditions are not fixed and when noise is introduced. To show this, measurements taken from a configuration including certain locations, time intervals, and noise profiles were considered as a training set whereas measurements taken from a different configuration were considered as a validation set and classified in a bootstrap fashion.

In this part, white noise was added on EGM signals with certain magnitudes. Figure 7.3 shows the

Table 7.2: Classification performance for inter-measurement configurations.

Data Set 1			Data Set 2			1-2	2-1
Loc.	T. Per. ^a	R ^b	Loc.	T. Per.	R	TCR ^c	TCR
5	[2.5,10]	0.05	5	[2.5,10]	0.05	0.95	-
5	[2.5,10]	0.1	5	[2.5,10]	0.1	0.92	-
3	[2.5,10]	0	5	[2.5,10]	0	0.97	0.96
3	[5,7.5]	0	5	[7.5,10]	0	0.99	0.99
3	[2.5,10]	0.05	5	[2.5,10]	0.05	0.90	0.89
3	[5,7.5]	0.05	5	[7.5,10]	0.05	0.89	0.85
3	[5,7.5]	0.1	5	[7.5,10]	0.1	0.72	0.69

^aTime period in sec.

^bR: Noise magnitude

^cTCR: True classification rate

Table 7.3: Inter Locations 3 and 5 Classification

	Stationary	Meandering	Breakup
Stationary	461	39	0
Meandering	3	494	3
Breakup	1	0	499

Table 7.4: Inter Locations 3 and 5 with Noise Classification

	Stationary	Meandering	Breakup
Stationary	394	23	83
Meandering	2	459	39
Breakup	8	2	490

effect of noise on an EGM signal with two different magnitudes. Similar to the previous subsections, unipolar readings from PentaRay catheter was considered only. For inter-location tests locations 3 and 5 were considered.

The results are shown in Table 7.2. Data sets 1 and 2 were obtained from measurements taken at different locations (either 3 or 5), time intervals and with different noise profiles. 1-2 refers to a case where data set 1 was considered as validation set whereas data set 2 was considered as training set and vice versa. Nearest neighbors for k-NN algorithm was set to 5. Overall, inter-locations and inter-time intervals classifications did not affect classification accuracy as outstanding classification accuracy was still attained. Only when noise was introduced, some deterioration happened which was not, however, as remarkable. An inspection was carried on two cases where inter-location classification was performed with and without noise through confusion matrices in Tables 7.3 and 7.4. Increases can be seen in the numbers where stationary and meandering behaviors were predicted as breakup. There is also some increase in the number where breakup is predicted as stationary. This is suspected to be due to effect of noise on EGM morphology therefore causing irregularity. However, this effect should only be occasional as can be seen in Figure 7.3 B where only one of the small deflection is affected. The noise also caused perturbations on the isoelectric baseline. The effect of this in classification performance should be minimal since a uniform increase in the number of each false prediction is not observed. Also, the noise magnitude whose effect is mostly observed

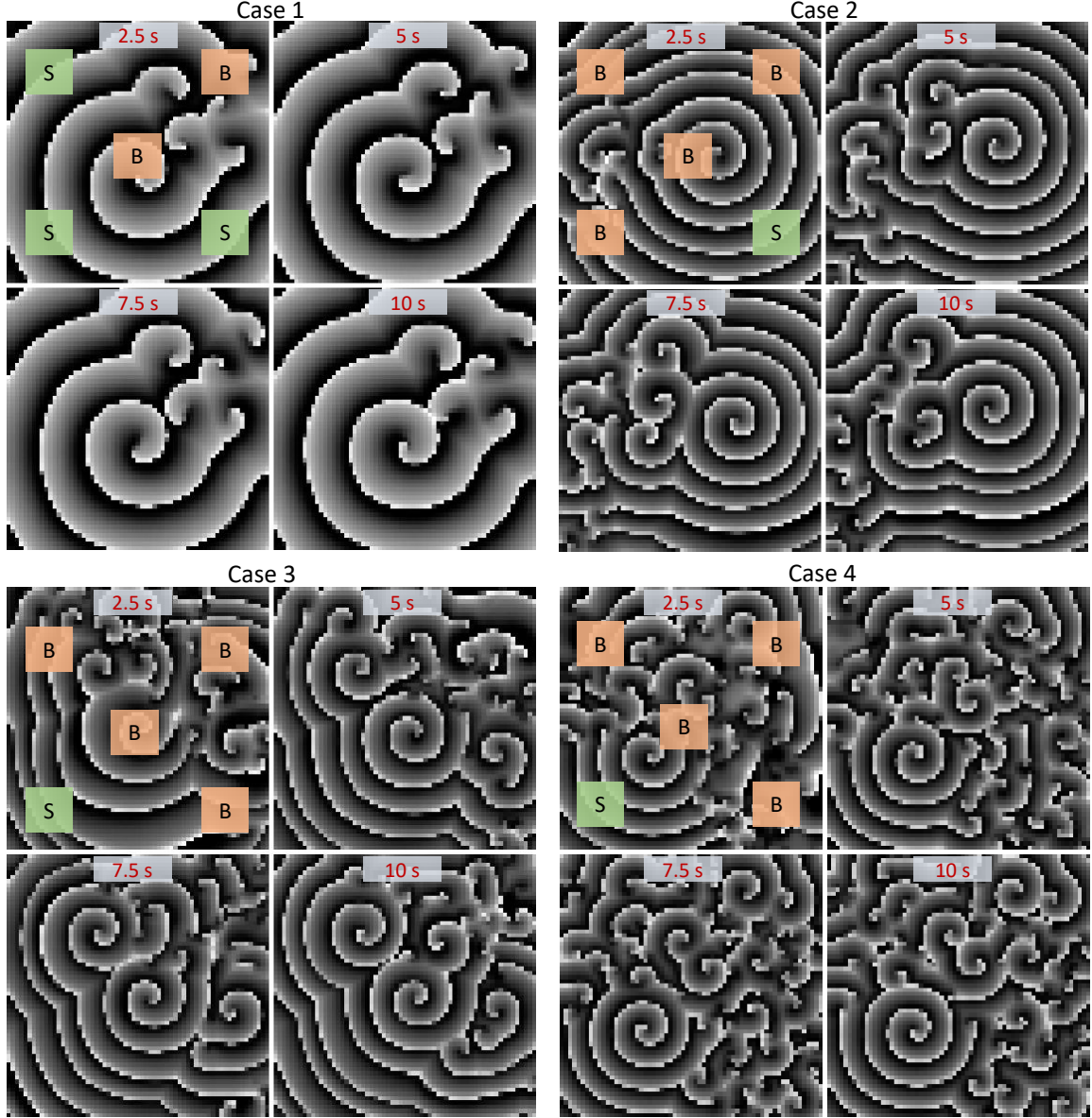


Figure 7.5: Classification of spiral behaviors in case of heterogeneous spiral behavior distribution around the tissue patch. Each case is represented with four snapshots taken at 2.5, 5, 7.5 and 10 s. Classified behaviors at each location is labeled with respective spiral behavior. S: Stationary, M: Meander, B: Breakup.

in perturbations of isoelectric baseline was not apparently effective in classification performance. In addition, when only noise was present and measurement setup was within intra-location and intra-time interval, classification performance was not affected. This agrees with the findings from [Cebrián et al.¹⁸⁸] where NCD was shown to be robust in spite of noise.

Heterogeneous Tissue: In some cases, simulations were resulted in heterogeneous spiral behaviors throughout the tissue although electro-physiological heterogeneity was not introduced. In general, a stationary rotor was located on a part of the tissue and wave breaks were all around which resembles a "mother rotor". Four of such cases are shown in Figure 7.5. Using unipolar electrograms recorded through PentaRay catheter, true classification was obtained in all simulations and locations except only in Case 2 stationary rotor at Location 3 was classified as breakup.

7.4 Discussions

7.4.1 Clinical Implications and Future Works

The findings in this context include connections primarily to mapping and analysis aspect of clinical applications. Therapeutic decision making is somehow independent because unraveling certain wavefront propagation pattern does not necessitate a certain belief about underlying mechanism(s). For instance, a same mapping may yield different interpretation with respect to theories of multiple wavelet [Moe and Abildskov⁵⁹, Allesie¹⁹⁴] and mother rotor [Sahadevan et al.⁶⁶, Vaquero et al.⁶⁵]. The Implication being here is rather potential reconstruction of activation patterns with a smaller number of electrodes via a characterization based on spiral wave behaviors.

It is important to note, however, the findings at this stage are not sufficient to claim that the approach fully developed in terms of clinical applications. However, various promising implications are present raising motivation for empirical verification(s). Verification(s) can be through clinical and/or experimental instruments as well as can be for different contributions made using the method *in silico*. To take usefulness of NCD in segregating EGMs as an example, verification of it can be implemented with respect to different assumed classes such as differentiating complex fractionated atrial EGMs. Another example could be verification of being able to predict global tissue rotor behavior from local EGM readings. In a clinical setting, a specific setup for this might be needed requiring simultaneous recordings obtained from both a MPDC and a basket catheter to show that data obtained from MPDC can be used to predict electrical rotor activity mapped through the basket catheter. This requires a non-standard clinical measurement setting.

7.4.2 Relevance to Clinical Applications

In this part, relevance of the approach and findings here to state of the art cardiac electrophysiology mapping is discussed. It is important to note, at this stage, the findings are not yet fully developed in terms of clinical applications including only implications. Therefore, the objective in this part is mainly to provide motivation for empirical verification of the method.

A premise in this study is that regardless of the mechanism behind it, the resulting wave front propagation patterns of cardiac electrical rotors are represented by only three subtype of spiral wave behaviors: stationary, meandering, and breakup. Justification for this comes from both experimental evidences and conceptual point of view. First, these behaviors are observed from *in vivo*, *in vitro* studies which are from animal and human hearts. More specifically, both stationary and meandering spiral waves were observed in perfused epicardial muscle from sheep and dogs [Davidenko et al.²⁵]. Using an optical mapping on a Langendorf-perfused left atrium of dogs, anchoring rotors were mapped and epicardial rotor ablation was shown to outperform non-rotor ablation in suppressing AF inducibility [Chou et al.¹⁹⁵]. The presence of both stationary and mobile rotors were demonstrated *in vivo* on a high density epicardial mapping using an electrode sock on human ventricles [Nash et al.²⁸, Ten Tusscher et al.²⁹]. The rotor breakups were revealed in high density mapping of human right atrium [Konings et al.²⁶]. Finally, both sustained [Narayan et al.³⁰] and migrating rotors [Narayan et al.³¹] in human atria were also mapped using basket catheters. From the conceptual point of view and using the insight from excitable media, the mentioned behaviors conclusively define the possible wave propagation patterns and/or their interactions. Even when mathematical possibilities of spiral waves which would be boundless when some details such as the wavelength, conductivity, respective location of the rotation centers, and the number of wavelets are taken into account, the patterns could be attached to the sub-categorization adopted in this study without necessarily leading to a new type of behavior. In other words, selected are encompassing behaviors to which further features can be attached. For instance, once a certain spiral behavior is assessed for a tissue, further quantities related to wavelength and conductivity can be contextualized within that behavior.

Today, electric rotors are reconstructed in clinics using tools such as monophasic action potential

(AP) catheter or basket catheter with multiple array of sensors providing global but low-resolution measurements. Computational mapping techniques are then used to reveal spatial and temporal organization of electrical rotors by constructing isopotential movies, isochronal maps or phase analysis [Narayan et al.³⁰, Narayan et al.¹⁰⁷, Narayan et al.³¹]. Furthermore, same investigators presented a treatment paradigm for AF by ablation of detected center of the rotational source [Narayan et al.⁹]. However, these tools are high-cost and not broadly present for most practitioners. Additionally, reconstruction of activation times, monophasic APs or phase maps is not robust because of the abrupt changes and variations in EGM amplitude, presence of conduction block, or slow conduction especially in atria regions. On the other hand, the most commonly used tools, MPDCs, yield more localized but high-resolution EGM readings and hence provide relatively limited spatial information. Their use in reconstruction of wavefront propagation mapping is therefore rudimentary. In this framework, we show by using synthetic data that the most commonly used and lower cost MPDCs can be utilized in a more improved way to characterize spatially extended electrophysiological activities. It should be noted, however, that clinical contribution of the proposed method in terms of treatment is not yet obvious since neither any of the mechanisms behind the fibrillatory rhythm is considered nor the identification and assessment of any electropathological source is targeted.

Another aspect for the proposed method is associated with the way EGM signals are used for the characterization. To date, various methods for analysis of fibrillatory dynamics through EGM signals are reported. A template matching technique was used for automatic characterization of unipolar human AF EGMs obtained from multi-electrode epicardial data and matched with a library of mathematically constructed unipolar EGM templates where fractionated EGMs were excluded that led to activation time detection and hence mapping of AF [Houben et al.¹¹⁹]. In a simulation study, EGM morphology was shown to reflect the wavefront propagation patterns and anisotropy in the tissue on a beat-to-beat basis [Jacquemet et al.¹²²]. Nollo et al. introduced a scheme that perform AF-type characterization based on Wells criteria through automatic classification of atrial EGM signals using JeffriesMatusita distance incorporating a multitude of features extracted from EGM signals [Nollo et al.³⁶]. Studies so far have characterized EGMs themselves and the association

between fibrillary dynamics were implied. Here, we characterize not EGMs themselves but what they point to in a context where cohort of EGMs from multi-channels are linked to rotor behaviors which are more visual and easier to interpret.

7.4.3 Limitations

Simulations were performed on a 2D tissue and electrophysiological homogeneity was assumed. The heterogeneity in that sense on a closed 3D geometry would better represent heart electroanatomy especially for atria. However, we would not expect emergence of totally new behaviors other than assumed ones in this study and hence new patterns in manifestation of EGM signals. Rather, corresponding spiral behavior for a certain parameter set would change. In other words, wavefront interactions may exhibit different dynamics and into a certain extent, spiral behaviors may transition to another state because as one can imagine on a closed geometry the boundary conditions will be different as a certain wave front can collide to another one instead of vanishing from boundary as it is in the case of 2D patch. In fact, the question is if there can exist conditions that the pattern of EGM manifestations would change even though the spiral wave behavior stays the same. We suspect this may happen through structural heterogeneity such as anisotropy in conductivity or configuration in cell coupling and/or decoupling that exists on the tissue. A previous work has demonstrated the effect of anisotropy on EGM morphology [Jacquemet et al.¹²²]. In such a scenario, training sets would have to be improved in order to keep the effectiveness in grouping.

Chapter 8: Conclusions

In this thesis, methods are developed for adaptation of a phenomenological model to represent human atrial electrophysiology properties and characterization of simulated cardiac tissue fibrillatory patterns. Challenges in respective fields are connected within a bigger framework of using an efficient model for analysis and interpretation of electrophysiological measurements obtained in clinics and adaptation of the model to patient-specific findings (see Figure 8.1).

In the first part, parameter estimation of MRM is performed to match electrophysiological properties of human atria. Successful adaptation of MRM in cellular level (APD and APD RC) and approximation in tissue level (wavefront excitation) provides significant implications because (1) MRM as a lower order model is easier for analysis hence its convergence to a desired state as can happen in matching a patient-specific data is expected to be rather easier, (2) it is computationally more efficient having the potential for nearly real time speed that enables it to be used in clinical settings. Furthermore, use of EKF is demonstrated to be advantageous for this task as it incorporates both dynamics of the system and stochasticity during the search for local minima, a factor providing room for finding better ones.

In the second part, a mapping and analysis framework for fibrillatory cardiac wavefront propagation patterns using simulated electrophysiology signals is proposed. Successful tests performed on the framework offers (1) data quantity reduction along with data quality increase and (2) enhanced performance of most commonly used diagnostic tools. The first is realized through a mapping from multi-dimensional voltage space to diagnostically more relevant cardiac tissue electrophysiology events, specifically electric rotors which are symptoms associated with reentry pathology observed in cardiac tissue through both clinical and experimental settings. Also, prediction of wavefront propagation patterns in both homogeneous and heterogeneous reentry behavior throughout entire tissue is demonstrated to be possible with only a small number of electrodes. That precipitates a ground for obtaining more information from the most commonly used, locally measuring but high-resolution

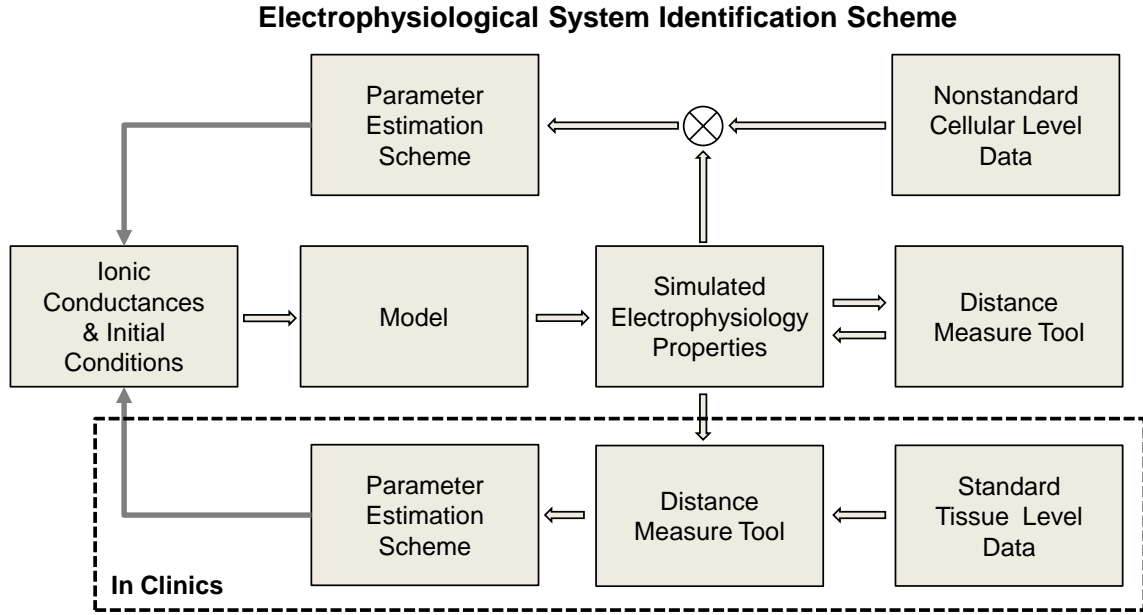


Figure 8.1: A diagram representing a system identification scheme that may lead to development of patient - specific electrophysiology modeling and simulation. Components inside the dashed box represent the workflow to be done only in a clinical environment.

catheters. We believe the proposed is a promising method that can be useful in its fully developed form in clinics for mapping and analysis of fibrillatory patterns.

The proposed methods can be considered as incremental steps precipitating patient-specific electrophysiology modeling and simulation hence their collective utilization on real patient data. A schematic diagram including the components for this long term goal is demonstrated in Figure 8.1. In the present thesis, the works outside the dashed box is implemented. First, parameter estimation of the model to reproduce a reference data is shown to be possible when the signals to be compared are compatible. In this respect, the reference data is constituted of cellular level signals that require nonstandard, special experimental measurement setups. Second, a robust tool that can assess a distance measure therefore can modulate an error value between multi-channel, time-varying electrogram signals which are not usually in conjunction is presented. The proposed method is theoretically validated using simulated data. However, there is still a need for verification of the method using real data requiring a nonstandard clinical measurement setting. Such a specific one might be in a form where simultaneous recordings from both an MPDC and a basket catheter are

used to demonstrate that data obtained from MPDC can be used to predict electrical rotor activity mapped through the basket catheter. In conclusion, the proposed methods are in compliance with utilization of computational and systems approach in clinics towards a better interpretation of electrophysiological signals and a better understanding of fibrillatory mechanisms therefore faster and improved therapeutic decision making.

Bibliography

- [1] Ulrich Schotten, Sander Verheule, Paulus Kirchhof, and Andreas Goette. Pathophysiological mechanisms of atrial fibrillation: a translational appraisal. *Physiological reviews*, 91(1):265–325, 2011.
- [2] Reza Wakili, Niels Voigt, Stefan Kääh, Dobromir Dobrev, and Stanley Nattel. Recent advances in the molecular pathophysiology of atrial fibrillation. *The Journal of clinical investigation*, 121(8):2955, 2011.
- [3] Joachim R. Ehrlich, Peter Biliczki, Stefan H. Hohnloser, and Stanley Nattel. Atrial-selective approaches for the treatment of atrial fibrillation. *Journal of the American College of Cardiology*, 51(8):787–792, 2008. doi: 10.1016/j.jacc.2007.08.067. URL <http://dx.doi.org/10.1016/j.jacc.2007.08.067>.
- [4] Stanley Nattel. New ideas about atrial fibrillation 50 years on. *Nature*, 415(6868):219–226, 2002.
- [5] Stanley Nattel, Brett Burstein, and Dobromir Dobrev. Atrial remodeling and atrial fibrillation mechanisms and implications. *Circulation: Arrhythmia and Electrophysiology*, 1(1):62–73, 2008.
- [6] Yu-ki Iwasaki, Kunihiro Nishida, Takeshi Kato, and Stanley Nattel. Atrial fibrillation pathophysiology implications for management. *Circulation*, 124(20):2264–2274, 2011.
- [7] Elizabeth M Cherry and Flavio H Fenton. Visualization of spiral and scroll waves in simulated and experimental cardiac tissue. *New Journal of Physics*, 10(12):125016, 2008.
- [8] Hugh Calkins, Karl Heinz Kuck, Riccardo Cappato, Josep Brugada, A John Camm, Shih-Ann Chen, Harry JG Crijns, Ralph J Damiano, D Wyn Davies, John DiMarco, et al. 2012 hrs/ehra/ecas expert consensus statement on catheter and surgical ablation of atrial fibrillation: recommendations for patient selection, procedural techniques, patient management and follow-up, definitions, endpoints, and research trial design. *Europace*, 14(4):528–606, 2012.
- [9] Sanjiv M Narayan, David E Krummen, Kalyanam Shivkumar, Paul Clopton, Wouter-Jan Rappel, and John M Miller. Treatment of atrial fibrillation by the ablation of localized sources: Confirm (conventional ablation for atrial fibrillation with or without focal impulse and rotor modulation) trial. *Journal of the American College of Cardiology*, 60(7):628–636, 2012.
- [10] Karen TS Konings, Joep LRM Smeets, Olaf C Penn, Hein JJ Wellens, and Maurits A Allessie. Configuration of unipolar atrial electrograms during electrically induced atrial fibrillation in humans. *Circulation*, 95(5):1231–1241, 1997.
- [11] Marc Courtemanche, Rafael J Ramirez, and Stanley Nattel. Ionic mechanisms underlying human atrial action potential properties: insights from a mathematical model. *American Journal of Physiology-Heart and Circulatory Physiology*, 275(1):H301–H321, 1998.
- [12] Zhilin Qu, Yuanfang Xie, Alan Garfinkel, and James N Weiss. T-wave alternans and arrhythmogenesis in cardiac diseases. *Frontiers in physiology*, 1, 2010.
- [13] NVIDIA Corporation. Cuda c programming guide, 2015. URL <https://docs.nvidia.com/cuda/cuda-c-programming-guide.html>.
- [14] CUDA Programming. What is "constant memory" in cuda?, 2012. URL <http://cuda-programming.blogspot.com/2013/01/what-is-constant-memory-in-cuda.html>.

- [15] Jianlin Feng, Lixia Yue, Zhiguo Wang, and Stanley Nattel. Ionic mechanisms of regional action potential heterogeneity in the canine right atrium. *Circulation Research*, 83(5):541–551, 1998.
- [16] G Seemann, C Höper, FB Sachse, H Zhang, and O Dössel. A detailed model of human atrium towards simulation of electromechanics in the heart. *Proc. MEDICON, Ischia, Italy*, 2004.
- [17] Marc Courtemanche, Rafael J Ramirez, and Stanley Nattel. Ionic targets for drug therapy and atrial fibrillation-induced electrical remodeling: insights from a mathematical model. *Cardiovascular research*, 42(2):477–489, 1999.
- [18] Ezio Bartocci, Rupinder Singh, Frederick B von Stein, Avesse Amedome, Alan Joseph J Caceres, Juan Castillo, Evan Closser, Gabriel Deards, Andriy Goltsev, Roumwelle Sta Ines, et al. Teaching cardiac electrophysiology modeling to undergraduate students: laboratory exercises and gpu programming for the study of arrhythmias and spiral wave dynamics. *Advances in physiology education*, 35(4):427–437, 2011.
- [19] A Nygren, C Fiset, L Firek, JW Clark, DS Lindblad, RB Clark, and WR Giles. Mathematical model of an adult human atrial cell the role of k^+ currents in repolarization. *Circulation Research*, 82(1):63–81, 1998.
- [20] Flavio Fenton and Alain Karma. Vortex dynamics in three-dimensional continuous myocardium with fiber rotation: filament instability and fibrillation. *Chaos: An Interdisciplinary Journal of Nonlinear Science*, 8(1):20–47, 1998.
- [21] Colleen C Mitchell and David G Schaeffer. A two-current model for the dynamics of cardiac membrane. *Bulletin of mathematical biology*, 65(5):767–793, 2003.
- [22] Alfonso Bueno-Orovio, Elizabeth M Cherry, and Flavio H Fenton. Minimal model for human ventricular action potentials in tissue. *Journal of theoretical biology*, 253(3):544–560, 2008.
- [23] P Comtois, J Kneller, and S Nattel. Of circles and spirals: bridging the gap between the leading circle and spiral wave concepts of cardiac reentry. *Europace*, 7(s2):S10–S20, 2005.
- [24] James L Cox, TE Canavan, RB Schuessler, ME Cain, BD Lindsay, C Stone, PK Smith, PB Corr, and JP Boineau. The surgical treatment of atrial fibrillation. ii. intraoperative electrophysiologic mapping and description of the electrophysiologic basis of atrial flutter and atrial fibrillation. *The Journal of thoracic and cardiovascular surgery*, 101(3):406–426, 1991.
- [25] JM Davidenko, AV Pertsov, R Salomonsz, W Baxter, and J Jalife. Stationary and drifting spiral waves of excitation in isolated cardiac muscle. *Nature*, 355(6358):349–351, 1992.
- [26] KT Konings, CJ Kirchhof, JR Smeets, HJ Wellens, Olaf C Penn, and Maurits A Allessie. High-density mapping of electrically induced atrial fibrillation in humans. *Circulation*, 89(4):1665–1680, 1994.
- [27] Richard A Gray, Arkady M Pertsov, and José Jalife. Spatial and temporal organization during cardiac fibrillation. *Nature*, 392(6671):75–78, 1998.
- [28] Martyn P Nash, Ayman Mourad, Richard H Clayton, Peter M Sutton, Chris P Bradley, Martin Hayward, David J Paterson, and Peter Taggart. Evidence for multiple mechanisms in human ventricular fibrillation. *Circulation*, 114(6):536–542, 2006.
- [29] Kirsten HWJ Ten Tusscher, Alexander V Panfilov, et al. Organization of ventricular fibrillation in the human heart. *Circulation Research*, 100(12):e87–e101, 2007.
- [30] Sanjiv M Narayan, David E Krummen, and Wouter-Jan Rappel. Clinical mapping approach to diagnose electrical rotors and focal impulse sources for human atrial fibrillation. *Journal of cardiovascular electrophysiology*, 23(5):447–454, 2012.

- [31] Sanjiv M Narayan, Kalyanam Shivkumar, David E Krummen, John M Miller, and Wouter-Jan Rappel. Panoramic electrophysiological mapping but not electrogram morphology identifies stable sources for human atrial fibrillation: Stable af rotors and focal sources relate poorly to fractionated electrograms. *Circulation: Arrhythmia and Electrophysiology*, pages CIRCEP–112, 2013.
- [32] Matthew W Kay and Richard A Gray. Measuring curvature and velocity vector fields for waves of cardiac excitation in 2-d media. *IEEE transactions on biomedical engineering*, 52(1):50–63, 2005.
- [33] A Murthy, E Bartocci, FH Fenton, J Glimm, RA Gray, EM Cherry, SA Smolka, and R Grosu. Curvature analysis of cardiac excitation wavefronts. *IEEE/ACM transactions on computational biology and bioinformatics/IEEE, ACM*, 10(2):323, 2013.
- [34] JL Wells Jr, RB Karp, NT Kouchoukos, WA MacLean, TN James, and AL Waldo. Characterization of atrial fibrillation in man: studies following open heart surgery. *Pacing and clinical electrophysiology: PACE*, 1(4):426–438, 1978.
- [35] Mathias Baumert, Prashanthan Sanders, and Anand Ganesan. Quantitative-electrogram-based methods for guiding catheter ablation in atrial fibrillation. *Proceedings of the IEEE*, 104(2):416–431, 2016.
- [36] Giandomenico Nollo, Mattia Marconcini, Luca Faes, Francesca Bovolo, Flavia Ravelli, and Lorenzo Bruzzzone. An automatic system for the analysis and classification of human atrial fibrillation patterns from intracardiac electrograms. *Biomedical Engineering, IEEE Transactions on*, 55(9):2275–2285, 2008.
- [37] Rudi Cilibrasi and Paul Vitanyi. Clustering by compression. *Information Theory, IEEE Transactions on*, 51(4):1523–1545, 2005.
- [38] Andrew R Cohen and Paul MB Vitányi. Normalized compression distance of multisets with applications. *IEEE transactions on pattern analysis and machine intelligence*, 37(8):1602–1614, 2015.
- [39] William M Feinberg, Joseph L Blackshear, Andreas Laupacis, Richard Kronmal, and Robert G Hart. Prevalence, age distribution, and gender of patients with atrial fibrillation: analysis and implications. *Archives of internal medicine*, 155(5):469–473, 1995.
- [40] Douglas P Zipes and Hein JJ Wellens. Sudden cardiac death. *Circulation*, 98(21):2334–2351, 1998.
- [41] Cees B de Vos, Ron Pisters, Robby Nieuwlaat, Martin H Prins, Robert G Tieleman, Robert-Jan S Coelen, Antonius C van den Heijkan, Maurits A Allessie, and Harry JGM Crijns. Progression from paroxysmal to persistent atrial fibrillation: clinical correlates and prognosis. *Journal of the American College of Cardiology*, 55(8):725–731, 2010.
- [42] Johan E.P. Waktare. Atrial fibrillation. *Circulation*, 106(1):14–16, 2002. doi: 10.1161/01.CIR.0000022730.66617.D9. URL <http://circ.ahajournals.org/content/106/1/14.short>.
- [43] Alan S Go, Elaine M Hylek, Kathleen A Phillips, YuChiao Chang, Lori E Henault, Joe V Selby, and Daniel E Singer. Prevalence of diagnosed atrial fibrillation in adults: national implications for rhythm management and stroke prevention: the anticoagulation and risk factors in atrial fibrillation (atria) study. *JAMA*, 285(18):2370–2375, 2001.
- [44] FD Richard Hobbs, DA Fitzmaurice, J Mant, E Murray, S Jowett, S Bryan, J Raftery, M Davies, and G Lip. A randomised controlled trial and cost-effectiveness study of systematic screening (targeted and total population screening) versus routine practice for the detection of atrial fibrillation in people aged 65 and over. the safe study. *Health Technology Assessment*, 9(40):93pp, 2005.

- [45] Yoko Miyasaka, Marion E Barnes, Bernard J Gersh, Stephen S Cha, Kent R Bailey, Walter P Abhayaratna, James B Seward, and Teresa SM Tsang. Secular trends in incidence of atrial fibrillation in olmsted county, minnesota, 1980 to 2000, and implications on the projections for future prevalence. *Circulation*, 114(2):119–125, 2006.
- [46] Susan Colilla, Ann Crow, William Petkun, Daniel E Singer, Teresa Simon, and Xianchen Liu. Estimates of current and future incidence and prevalence of atrial fibrillation in the us adult population. *The American journal of cardiology*, 112(8):1142–1147, 2013.
- [47] Philip A Wolf, Thomas R Dawber, H Emerson Thomas, and William B Kannel. Epidemiologic assessment of chronic atrial fibrillation and risk of stroke the fiamingham study. *Neurology*, 28(10):973–973, 1978.
- [48] Teresa SM Tsang, Yoko Miyasaka, Marion E Barnes, and Bernard J Gersh. Epidemiological profile of atrial fibrillation: a contemporary perspective. *Progress in cardiovascular diseases*, 48(1):1–8, 2005.
- [49] Ole Dyg Pedersen, Steen Z Abildstrøm, Michael M Ottesen, Christian Rask-Madsen, Henning Bagger, Lars Køber, and Christian Torp-Pedersen. Increased risk of sudden and non-sudden cardiovascular death in patients with atrial fibrillation/flutter following acute myocardial infarction. *European heart journal*, 27(3):290–295, 2006.
- [50] Stefan Knecht, Christian Oelschläger, Thomas Duning, Hubertus Lohmann, Johannes Albers, Christoph Stehling, Walter Heindel, Günter Breithardt, Klaus Berger, E Bernd Ringelstein, et al. Atrial fibrillation in stroke-free patients is associated with memory impairment and hippocampal atrophy. *European heart journal*, 29(17):2125–2132, 2008.
- [51] Leif Friberg, Niklas Hammar, and Mårten Rosenqvist. Stroke in paroxysmal atrial fibrillation: report from the stockholm cohort of atrial fibrillation. *European heart journal*, 31(8):967–975, 2010.
- [52] Constanze Schmidt, Jana Kisselbach, Patrick A Schweizer, Hugo A Katus, and Dierk Thomas. The pathology and treatment of cardiac arrhythmias: focus on atrial fibrillation. *Vascular health and risk management*, 7:193, 2011.
- [53] Edward J Vigmond, Vincent Tsoi, Yalin Yin, Pierre Page, and Alain Vinet. Estimating atrial action potential duration from electrograms. *Biomedical Engineering, IEEE Transactions on*, 56(5):1546–1555, 2009.
- [54] Heinrich Winterberg. Studien über herzflimmern. *Pflügers Archiv European Journal of Physiology*, 117(3):223–256, 1907.
- [55] George Ralph Mines. On dynamic equilibrium in the heart. *The Journal of physiology*, 46(4-5):349–383, 1913.
- [56] Walter E Garrey. The nature of fibrillary contraction of the heart: its relation to tissue mass and form. *Am J physiol*, 33:397–414, 1914.
- [57] Thomas Lewis, HS Feil, and WD Stroud. Observations upon flutter and fibrillation. *Heart*, 7: 127, 1920.
- [58] David Scherf. Studies on auricular tachycardia caused by aconitine administration. *Experimental Biology and Medicine*, 64(2):233–239, 1947.
- [59] GK Moe and JA Abildskov. Atrial fibrillation as a self-sustaining arrhythmia independent of focal discharge. *American heart journal*, 58(1):59–70, 1959.
- [60] Maurits A Allesie. Experimental evaluation of moe’s multiple wavelet hypothesis of atrial fibrillation. *Cardiac arrhythmias*, pages 265–276, 1985.

- [61] Michel Haissaguerre, Pierre Jaïs, Dipen C Shah, Atsushi Takahashi, Mélèze Hocini, Gilles Quiniou, Stéphane Garrigue, Alain Le Mouroux, Philippe Le Métayer, and Jacques Clémenty. Spontaneous initiation of atrial fibrillation by ectopic beats originating in the pulmonary veins. *New England Journal of Medicine*, 339(10):659–666, 1998.
- [62] Allan C Skanes, Ravi Mandapati, Omer Berenfeld, Jorge M Davidenko, and José Jalife. Spatiotemporal periodicity during atrial fibrillation in the isolated sheep heart. *Circulation*, 98(12):1236–1248, 1998.
- [63] Ravi Mandapati, Allan Skanes, Jay Chen, Omer Berenfeld, and José Jalife. Stable microreentrant sources as a mechanism of atrial fibrillation in the isolated sheep heart. *Circulation*, 101(2):194–199, 2000.
- [64] Moussa Mansour, Ravi Mandapati, Omer Berenfeld, Jay Chen, Faramarz H Samie, and José Jalife. Left-to-right gradient of atrial frequencies during acute atrial fibrillation in the isolated sheep heart. *Circulation*, 103(21):2631–2636, 2001.
- [65] Miguel Vaquero, David Calvo, and José Jalife. Cardiac fibrillation: from ion channels to rotors in the human heart. *Heart Rhythm*, 5(6):872–879, 2008.
- [66] Jayakumar Sahadevan, Kyungmoo Ryu, Leora Peltz, Celeen M Khrestian, Robert W Stewart, Alan H Markowitz, and Albert L Waldo. Epicardial mapping of chronic atrial fibrillation in patients preliminary observations. *Circulation*, 110(21):3293–3299, 2004.
- [67] Douglas P Zipes. Atrial fibrillation a tachycardia-induced atrial cardiomyopathy. *Circulation*, 95(3):562–564, 1997.
- [68] Kaoru Okishige, Tetsuo Sasano, Kei Yano, Kouji Azegami, Kou Suzuki, and Kuniyasu Itoh. Serious arrhythmias in patients with apical hypertrophic cardiomyopathy. *Internal Medicine*, 40(5):396–402, 2001.
- [69] Takanori Ikeda, Lawrence Czer, Alfredo Trento, Chun Hwang, James JC Ong, Dustan Hough, Michael C Fishbein, William J Mandel, Hrayr S Karagueuzian, and Peng-Sheng Chen. \ e induction of meandering functional reentrant wave front in isolated human atrial tissues. *Circulation*, 96(9):3013–3020, 1997.
- [70] Raymond Kapral and Kenneth Showalter. *Chemical waves and patterns*, volume 10. Springer Science & Business Media, 2012.
- [71] Harry L Swinney and Valentin I Krinsky. Waves and patterns in chemical and biological media. *Waves and Patterns in Chemical and Biological Media, Edited by Harry L. Swinney and Valentin I. Krinsky, pp. 264. ISBN 0-262-69150-7. Cambridge, Massachusetts, USA: The MIT Press, December 1991.(Paper)*, 1, 1991.
- [72] Jay Chen, Ravi Mandapati, Omer Berenfeld, Allan C Skanes, and José Jalife. High-frequency periodic sources underlie ventricular fibrillation in the isolated rabbit heart. *Circulation Research*, 86(1):86–93, 2000.
- [73] José Jalife, Omer Berenfeld, and Moussa Mansour. Mother rotors and fibrillatory conduction: a mechanism of atrial fibrillation. *Cardiovascular research*, 54(2):204–216, 2002.
- [74] Raymond E Ideker and Jack M Rogers. Human ventricular fibrillation wandering wavelets, mother rotors, or both? *Circulation*, 114(6):530–532, 2006.
- [75] Maurits CEF Wijffels, Charles JHJ Kirchhof, Rick Dorland, and Maurits A Allessie. Atrial fibrillation begets atrial fibrillation a study in awake chronically instrumented goats. *Circulation*, 92(7):1954–1968, 1995.

- [76] Trine Krogh-Madsen, Geoffrey W Abbott, and David J Christini. Effects of electrical and structural remodeling on atrial fibrillation maintenance: a simulation study. *PLoS Comput Biol*, 8(2):e1002390, 2012.
- [77] Carlos A Morillo, George J Klein, Douglas L Jones, and Colette M Guiraudon. Chronic rapid atrial pacing structural, functional, and electrophysiological characteristics of a new model of sustained atrial fibrillation. *Circulation*, 91(5):1588–1595, 1995.
- [78] Pieter L Rensma, Maurits A Allesie, WJ Lammers, FI Bonke, and Martin J Schalij. Length of excitation wave and susceptibility to reentrant atrial arrhythmias in normal conscious dogs. *Circulation research*, 62(2):395–410, 1988.
- [79] Maurits A Allesie. Atrial electrophysiologic remodeling: another vicious circle? *Journal of cardiovascular electrophysiology*, 9(12):1378–1393, 1998.
- [80] CJ Garratt, M Duytschaever, M Killian, R Dorland, F Mast, and MA Allesie. Repetitive electrical remodeling by paroxysms of atrial fibrillation in the goat: no cumulative effect on inducibility or stability of atrial fibrillation. *Journal of cardiovascular electrophysiology*, 10(8):1101–1108, 1999.
- [81] Simon P Fynn, Derick M Todd, W Julian C Hobbs, Karen L Armstrong, Adam P Fitzpatrick, and Clifford J Garratt. Clinical evaluation of a policy of early repeated internal cardioversion for recurrence of atrial fibrillation. *Journal of cardiovascular electrophysiology*, 13(2):135–141, 2002.
- [82] Martin K Stiles, Bobby John, Christopher X Wong, Pawel Kuklik, Anthony G Brooks, Dennis H Lau, Hany Dimitri, Kurt C Roberts-Thomson, Lauren Wilson, Paolo De Sciscio, et al. Paroxysmal lone atrial fibrillation is associated with an abnormal atrial substrate: characterizing the second factor. *Journal of the American College of Cardiology*, 53(14):1182–1191, 2009.
- [83] Jill E Bishop. Regulation of cardiovascular collagen deposition by mechanical forces. *Molecular medicine today*, 4(2):69–75, 1998.
- [84] Brett Burstein and Stanley Nattel. Atrial fibrosis: mechanisms and clinical relevance in atrial fibrillation. *Journal of the American College of Cardiology*, 51(8):802–809, 2008.
- [85] Felix Gramley, Johann Lorenzen, Christian Knackstedt, Obaida R Rana, Erol Saygili, Dirk Frechen, Sven Stanzel, Francesco Pezzella, Eva Koellensperger, Christian Weiss, et al. Age-related atrial fibrosis. *Age*, 31(1):27–38, 2009.
- [86] Maurits Allesie, Jannie Ausma, and Ulrich Schotten. Electrical, contractile and structural remodeling during atrial fibrillation. *Cardiovascular research*, 54(2):230–246, 2002.
- [87] Stefan H Hohnloser, Karl-Heinz Kuck, Jurgen Lilienthal, PIAF Investigators, et al. Rhythm or rate control in atrial fibrillationpharmacological intervention in atrial fibrillation (piaf): a randomised trial. *The Lancet*, 356(9244):1789–1794, 2000.
- [88] Isabelle C Van Gelder, Vincent E Hagens, Hans A Bosker, J Herre Kingma, Otto Kamp, Tsjerk Kingma, Salah A Said, Julius I Darmanata, Alphons JM Timmermans, Jan GP Tijssen, et al. A comparison of rate control and rhythm control in patients with recurrent persistent atrial fibrillation. *New England Journal of Medicine*, 347(23):1834–1840, 2002.
- [89] DG Wyse, AL Waldo, JP DiMarco, MJ Domanski, Y Rosenberg, EB Schron, JC Kellen, HL Greene, MC Mickel, JE Dalquist, et al. A comparison of rate control and rhythm control in patients with atrial fibrillation. *N Engl J Med*, 347(23):1825–33, 2002.

- [90] Jörg Carlsson, Sinisa Miketic, Jürgen Windeler, Alessandro Cuneo, Sebastian Haun, Stefan Micus, Sabine Walter, Ulrich Tebbe, STAF Investigators, et al. Randomized trial of rate-control versus rhythm-control in persistent atrial fibrillation. *Journal of the American College of Cardiology*, 41(10):1690–1696, 2003.
- [91] Affirm Investigators et al. Relationships between sinus rhythm, treatment, and survival in the atrial fibrillation follow-up investigation of rhythm management (affirm) study. *Circulation*, 109(12):1509–1513, 2004.
- [92] Stanley Nattel and Leif Carlsson. Innovative approaches to anti-arrhythmic drug therapy. *Nature reviews Drug discovery*, 5(12):1034–1049, 2006.
- [93] Stanley Nattel and Lionel H Opie. Controversies in atrial fibrillation. *The Lancet*, 367(9506):262–272, 2006.
- [94] Francisco G Cosio, Etienne Aliot, Giovanni Luca Botto, Hein Heidebüchel, Christoph Johan Geller, Paulus Kirchhof, Jean-Claude De Haro, Robert Frank, Julian Perez Villacastin, Johan Vijgen, et al. Delayed rhythm control of atrial fibrillation may be a cause of failure to prevent recurrences: reasons for change to active antiarrhythmic treatment at the time of the first detected episode. *Europace*, 10(1):21–27, 2008.
- [95] Pierre Jai, Michel Hai, Dipen C Shah, Salah Chouairi, Laurent Gencel, Jacques Cle, et al. A focal source of atrial fibrillation treated by discrete radiofrequency ablation. *Circulation*, 95(3):572–576, 1997.
- [96] Shih-Ann Chen, Ming-Hsiung Hsieh, Ching-Tai Tai, Chin-Feng Tsai, VS Prakash, Wen-Chung Yu, Tsui-Lieh Hsu, Yu-An Ding, and Mau-Song Chang. Initiation of atrial fibrillation by ectopic beats originating from the pulmonary veins electrophysiological characteristics, pharmacological responses, and effects of radiofrequency ablation. *Circulation*, 100(18):1879–1886, 1999.
- [97] Michel Haïssaguerre, Dipen C Shah, Pierre Jaïs, Mélèze Hocini, Teiichi Yamane, Isabel Deisenhofer, Michel Chauvin, Stéphane Garrigue, and Jacques Clémenty. Electrophysiological breakthroughs from the left atrium to the pulmonary veins. *Circulation*, 102(20):2463–2465, 2000.
- [98] Michel Haïssaguerre, Mélèze Hocini, Prashanthan Sanders, Yoshihide Takahashi, Martin Rotter, Frederic Sacher, Thomas Rostock, Li-Fern Hsu, Anders Jonsson, Mark D O'Neill, et al. Localized sources maintaining atrial fibrillation organized by prior ablation. *Circulation*, 113(5):616–625, 2006.
- [99] Edward P Gerstenfeld, Alan V Sahakian, and Steven Swiryn. Evidence for transient linking of atrial excitation during atrial fibrillation in humans. *Circulation*, 86(2):375–382, 1992.
- [100] Pierre Jais, Michel Haïssaguerre, Dipen C Shah, Salah Chouairi, and Jacques Clementy. Regional disparities of endocardial atrial activation in paroxysmal atrial fibrillation. *Pacing and clinical electrophysiology*, 19(11):1998–2003, 1996.
- [101] Koonlawee Nademanee, John McKenzie, Erol Kosar, Mark Schwab, Buncha Sunsaneewitayakul, Thaveekiat Vasavakul, Chotikorn Khunnawat, and Tachapong Ngarmukos. A new approach for catheter ablation of atrial fibrillation: mapping of the electrophysiologic substrate. *Journal of the American College of Cardiology*, 43(11):2044–2053, 2004.
- [102] Maurits A Allessie, Natasja MS de Groot, Richard PM Houben, Ulrich Schotten, Eric Boersma, Joep L Smeets, and Harry J Crijns. Electropathological substrate of long-standing persistent atrial fibrillation in patients with structural heart disease longitudinal dissociation. *Circulation: Arrhythmia and Electrophysiology*, 3(6):606–615, 2010.
- [103] Arthur T Winfree. *When time breaks down: the three-dimensional dynamics of electrochemical waves and cardiac arrhythmias*. Princeton University Press Princeton, 1987.

- [104] Mark-Anthony Bray and John P Wikswo. Considerations in phase plane analysis for nonstationary reentrant cardiac behavior. *Physical Review E*, 65(5):051902, 2002.
- [105] Mark-Anthony Bray and John P Wikswo. Use of topological charge to determine filament location and dynamics in a numerical model of scroll wave activity. *Biomedical Engineering, IEEE Transactions on*, 49(10):1086–1093, 2002.
- [106] Sanjiv Narayan and Carey Robert Briggs. System and method for reconstructing cardiac activation information, August 29 2014. US Patent App. 14/473,572.
- [107] Sanjiv M Narayan, David E Krummen, Michael W Enyeart, and Wouter-Jan Rappel. Computational mapping identifies localized mechanisms for ablation of atrial fibrillation. *PloS one*, 7(9):e46034, 2012.
- [108] William Robert Macneil and Ruchir Sehra. System and method to define a rotational source associated with a biological rhythm disorder, March 20 2014. US Patent App. 14/220,662.
- [109] Omer Berenfeld, Ravi Mandapati, Sanjay Dixit, Allan C Skanes, JAY Chen, Moussa Mansour, and José Jalife. Spatially distributed dominant excitation frequencies reveal hidden organization in atrial fibrillation in the langendorff-perfused sheep heart. *Journal of cardiovascular electrophysiology*, 11(8):869–879, 2000.
- [110] Thomas H Everett, J Randall Moorman, Lai-Chow Kok, Joseph G Akar, and David E Haines. Assessment of global atrial fibrillation organization to optimize timing of atrial defibrillation. *Circulation*, 103(23):2857–2861, 2001.
- [111] Sanjiv M Narayan, David E Krummen, Andrew M Kahn, Pamela L Karasik, and Michael R Franz. Evaluating fluctuations in human atrial fibrillatory cycle length using monophasic action potentials. *Pacing and clinical electrophysiology*, 29(11):1209–1218, 2006.
- [112] David E Krummen, Kevin A Peng, John R Bullinga, and Sanjiv M Narayan. Centrifugal gradients of rate and organization in human atrial fibrillation. *Pacing and clinical electrophysiology*, 32(11):1366–1378, 2009.
- [113] Frank M Weber, Christopher Schilling, Gunnar Seemann, Armin Luik, Claus Schmitt, Cristian Lorenz, and Olaf Dössel. Wave-direction and conduction-velocity analysis from intracardiac electrograms—a single-shot technique. *Biomedical Engineering, IEEE Transactions on*, 57(10):2394–2401, 2010.
- [114] Luca Faes, Giandomenico Nollo, Renzo Antolini, Fiorenzo Gaita, and Flavia Ravelli. A method for quantifying atrial fibrillation organization based on wave-morphology similarity. *Biomedical Engineering, IEEE Transactions on*, 49(12):1504–1513, 2002.
- [115] Sanjiv M Narayan, Dhruv Kazi, David E Krummen, and Wouter-Jan Rappel. Repolarization and activation restitution near human pulmonary veins and atrial fibrillation initiation: a mechanism for the initiation of atrial fibrillation by premature beats. *Journal of the American College of Cardiology*, 52(15):1222–1230, 2008.
- [116] Sanjiv M Narayan, Michael R Franz, Paul Clopton, Etienne J Pruvot, and David E Krummen. Repolarization alternans reveals vulnerability to human atrial fibrillation. *Circulation*, 123(25):2922–2930, 2011.
- [117] G Lalani, A Schricker, M Gibson, A Rostamianian, DE Krummen, and SM Narayan. Dynamic conduction slowing precedes human atrial fibrillation initiation: insights from bi-atrial basket mapping on transitions to atrial fibrillation. *J Am Coll Cardiol*, 59:595–606, 2012.
- [118] Frank M Weber, Armin Luik, Christopher Schilling, Gunnar Seemann, Martin W Krueger, Cristian Lorenz, Claus Schmitt, and Olaf Dössel. Conduction velocity restitution of the human atrium: an efficient measurement protocol for clinical electrophysiological studies. *Biomedical Engineering, IEEE Transactions on*, 58(9):2648–2655, 2011.

- [119] Richard PM Houben, Natasja MS de Groot, Fred W Lindemans, and Maurits A Allesie. Automatic mapping of human atrial fibrillation by template matching. *Heart Rhythm*, 3(10):1221–1228, 2006.
- [120] Richard PM Houben and MA Allesie. Processing of intracardiac electrograms in atrial fibrillation. *Engineering in Medicine and Biology Magazine, IEEE*, 25(6):40–51, 2006.
- [121] Richard PM Houben, Natasja De Groot, Maurits Allesie, et al. Analysis of fractionated atrial fibrillation electrograms by wavelet decomposition. *Biomedical Engineering, IEEE Transactions on*, 57(6):1388–1398, 2010.
- [122] Vincent Jacquemet, Nathalie Virag, Zenichi Ihara, Lam Dang, Olivier Blanc, Steeve Zozor, Jean-Marc Vésin, Lukas Kappenberger, and Craig Henriquez. Study of unipolar electrogram morphology in a computer model of atrial fibrillation. *Journal of cardiovascular electrophysiology.*, 14:no–10, 2003.
- [123] Frank B Sachse. *Computational Cardiology: Modeling of Anatomy, Electrophysiology, and Mechanics*, volume 2966. Springer Science & Business Media, 2004.
- [124] Alan L Hodgkin and Andrew F Huxley. A quantitative description of membrane current and its application to conduction and excitation in nerve. *The Journal of physiology*, 117(4):500–544, 1952.
- [125] Go W Beeler and H Reuter. Reconstruction of the action potential of ventricular myocardial fibres. *The Journal of physiology*, 268(1):177–210, 1977.
- [126] Leo Priebe and Dirk J Beuckelmann. Simulation study of cellular electric properties in heart failure. *Circulation research*, 82(11):1206–1223, 1998.
- [127] Olivier Bernus, Ronald Wilders, Christian W Zemlin, Henri Verschelde, and Alexander V Panfilov. A computationally efficient electrophysiological model of human ventricular cells. *American Journal of Physiology-Heart and Circulatory Physiology*, 282(6):H2296–H2308, 2002.
- [128] KHWJ Ten Tusscher, D Noble, PJ Noble, and AV Panfilov. A model for human ventricular tissue. *American Journal of Physiology-Heart and Circulatory Physiology*, 286(4):H1573–H1589, 2004.
- [129] Vivek Iyer, Reza Mazhari, and Raimond L Winslow. A computational model of the human left-ventricular epicardial myocyte. *Biophysical journal*, 87(3):1507–1525, 2004.
- [130] Richard FitzHugh. Impulses and physiological states in theoretical models of nerve membrane. *Biophysical journal*, 1(6):445, 1961.
- [131] P Colli Franzone, L Guerri, and S Rovida. Wavefront propagation in an activation model of the anisotropic cardiac tissue: asymptotic analysis and numerical simulations. *Journal of mathematical biology*, 28(2):121–176, 1990.
- [132] Maxime Sermesant, Ender Konukoglu, Hervé Delingette, Yves Coudière, Phani Chinchapatnam, Kawal Rhode, Reza Razavi, and Nicholas Ayache. An anisotropic multi-front fast marching method for real-time simulation of cardiac electrophysiology. *Functional Imaging and Modeling of the Heart*, pages 160–169, 2007.
- [133] J Keener and J Sneyd. Mathematical physiology i: Cellular physiology, ii: Systems physiology, 2009.
- [134] Berl G Bass. Restitution of the action potential in cat papillary muscle. *American Journal of Physiology-Legacy Content*, 228(6):1717–1724, 1975.

- [135] Zhilin Qu, James N Weiss, and Alan Garfinkel. Cardiac electrical restitution properties and stability of reentrant spiral waves: a simulation study. *American Journal of Physiology-Heart and Circulatory Physiology*, 276(1):H269–H283, 1999.
- [136] James N Weiss, Alan Garfinkel, Mark L Spano, and William L Ditto. Chaos and chaos control in biology. *Journal of Clinical Investigation*, 93(4):1355, 1994.
- [137] Alan Garfinkel, Peng-Sheng Chen, Donald O Walter, Hrayr S Karagueuzian, Boris Kogan, Steven J Evans, Mikhail Karpoukhin, Chun Hwang, Takumi Uchida, Masamichi Gotoh, et al. Quasiperiodicity and chaos in cardiac fibrillation. *Journal of Clinical Investigation*, 99(2):305, 1997.
- [138] Richard L Verrier and Bruce D Nearing. Electrophysiologic basis for t wave alternans as an index of vulnerability to ventricular fibrillation. *Journal of cardiovascular electrophysiology*, 5(5):445–461, 1994.
- [139] David S Rosenbaum, Lance E Jackson, Joseph M Smith, Hasan Garan, Jeremy N Ruskin, and Richard J Cohen. Electrical alternans and vulnerability to ventricular arrhythmias. *New England Journal of Medicine*, 330(4):235–241, 1994.
- [140] Joseph M Smith, Edward A Clancy, C Robert Valeri, Jeremy N Ruskin, and Richard J Cohen. Electrical alternans and cardiac electrical instability. *Circulation*, 77(1):110–121, 1988.
- [141] Joseph M Pastore, Steven D Girouard, Kenneth R Laurita, Fadi G Akar, and David S Rosenbaum. Mechanism linking t-wave alternans to the genesis of cardiac fibrillation. *Circulation*, 99(10):1385–1394, 1999.
- [142] T Klingenhoben, M Zabel, RB D’Agostino, RJ Cohen, and SH Hohnloser. Predictive value of t-wave alternans for arrhythmic events in patients with congestive heart failure. *The Lancet*, 356(9230):651–652, 2000.
- [143] Sanjiv M Narayan, Frank Bode, Pamela L Karasik, and Michael R Franz. Alternans of atrial action potentials during atrial flutter as a precursor to atrial fibrillation. *Circulation*, 106(15):1968–1973, 2002.
- [144] JB Nolasco and Roger W Dahlen. A graphic method for the study of alternation in cardiac action potentials. *J Appl Physiol*, 25(2):191–196, 1968.
- [145] MR Guevara, G Ward, A Shrier, and L Glass. Electrical alternans and period doubling bifurcations. *IEEE Comp. Cardiol*, 562:167–170, 1984.
- [146] Alain Karma. Electrical alternans and spiral wave breakup in cardiac tissue. *Chaos: An Interdisciplinary Journal of Nonlinear Science*, 4(3):461–472, 1994.
- [147] Marcus L Koller, Mark L Riccio, and Robert F Gilmour Jr. Dynamic restitution of action potential duration during electrical alternans and ventricular fibrillation. *American Journal of Physiology-Heart and Circulatory Physiology*, 275(5):H1635–H1642, 1998.
- [148] Blas Echebarria and Alain Karma. Instability and spatiotemporal dynamics of alternans in paced cardiac tissue. *Physical review letters*, 88(20):208101, 2002.
- [149] Flavio H Fenton, Elizabeth M Cherry, Harold M Hastings, and Steven J Evans. Multiple mechanisms of spiral wave breakup in a model of cardiac electrical activity. *Chaos: An Interdisciplinary Journal of Nonlinear Science*, 12(3):852–892, 2002.
- [150] Mari A Watanabe, Flavio H Fenton, Steven J Evans, Harold M Hastings, and Alain Karma. Mechanisms for discordant alternans. *Journal of cardiovascular electrophysiology*, 12(2):196–206, 2001.

- [151] Robert Plonsey and Roger C Barr. *Bioelectricity: a quantitative approach*. Springer Science & Business Media, 2007.
- [152] Nathalie Virag, Vincent Jacquemet, CS Henriquez, Steeve Zozor, Olivier Blanc, J-M Vesin, Etienne Pruvot, and Lukas Kappenberger. Study of atrial arrhythmias in a computer model based on magnetic resonance images of human atria. *Chaos: An Interdisciplinary Journal of Nonlinear Science*, 12(3):754–763, 2002.
- [153] Andrew J Pullan, Leo K Cheng, and Martin L Buist. *Mathematically modelling the electrical activity of the heart: From cell to body surface and back again*. World Scientific, 2005.
- [154] David UJ Keller, Frank M Weber, Gunnar Seemann, and Olaf Doessel. Ranking the influence of tissue conductivities on forward-calculated eegs. *Biomedical Engineering, IEEE Transactions on*, 57(7):1568–1576, 2010.
- [155] CD Werner, FB Sachse, and O Dössel. Electrical excitation propagation in the human heart. *International Journal of Bioelectromagnetism*, 2(2), 2000.
- [156] Adriaan van Oosterom and Vincent Jacquemet. Genesis of the p wave: atrial signals as generated by the equivalent double layer source model. *Europace*, 7(s2):S21–S29, 2005.
- [157] Daisuke Sato, Yuanfang Xie, James N Weiss, Zhilin Qu, Alan Garfinkel, and Allen R Sander-son. Acceleration of cardiac tissue simulation with graphic processing units. *Medical & biological engineering & computing*, 47(9):1011–1015, 2009.
- [158] Fawang Liu, John Walmsley, and Kevin Burrage. Parameter estimation for a phenomenological model of the cardiac action potential. *ANZIAM Journal*, 52:482–499, 2011.
- [159] M Boutjdir, JY Le Heuzey, T Lavergne, S Chauvaud, L Guize, A Carpentier, and P Peronneau. Inhomogeneity of cellular refractoriness in human atrium: factor of arrhythmia? *Pacing and clinical electrophysiology: PACE*, 9(6 Pt 2):1095, 1986.
- [160] Rudolph Emil Kalman. A new approach to linear filtering and prediction problems. *Journal of Fluids Engineering*, 82(1):35–45, 1960.
- [161] Ian B Rhodes. A tutorial introduction to estimation and filtering. *Automatic Control, IEEE Transactions on*, 16(6):688–706, 1971.
- [162] Dan Simon. *Optimal state estimation: Kalman, H infinity, and nonlinear approaches*. John Wiley & Sons, 2006.
- [163] Richard E Kopp and Richard J Orford. Linear regression applied to system identification for adaptive control systems. *AIAA Journal*, 1(10):2300–2306, 1963.
- [164] John Sum, Chi-Sing Leung, Gilbert H Young, and Wing-Kay Kan. On the kalman filtering method in neural network training and pruning. *Neural Networks, IEEE Transactions on*, 10(1):161–166, 1999.
- [165] Xiaogang Ruan, Mingxiao Ding, Daoxiong Gong, and Junfei Qiao. On-line adaptive control for inverted pendulum balancing based on feedback-error-learning. *Neurocomputing*, 70(4):770–776, 2007.
- [166] Dan Simon. Kalman filtering with state constraints: a survey of linear and nonlinear algorithms. *IET Control Theory & Applications*, 4(8):1303–1318, 2010.
- [167] Roger Fletcher. *Practical methods of optimization*. John Wiley & Sons, 2013.
- [168] Stephen Boyd and Lieven Vandenberghe. *Convex optimization*. Cambridge university press, 2004.

- [169] Klaus Schittkowski. Nlpql: A fortran subroutine solving constrained nonlinear programming problems. *Annals of operations research*, 5(2):485–500, 1986.
- [170] James Kennedy. Particle swarm optimization. In *Encyclopedia of Machine Learning*, pages 760–766. Springer, 2010.
- [171] Joaquín Meza, Helbert Espitia, Carlos Montenegro, Elena Giménez, and Rubén González-Crespo. Movpso: Vortex multi-objective particle swarm optimization. *Applied Soft Computing*, 52:1042–1057, 2017.
- [172] Joaquín Meza, Helbert Espitia, Carlos Montenegro, and Rubén González Crespo. Statistical analysis of a multi-objective optimization algorithm based on a model of particles with vorticity behavior. *Soft Computing*, 20(9):3521–3536, 2016.
- [173] Sankalap Arora and Satvir Singh. An effective hybrid butterfly optimization algorithm with artificial bee colony for numerical optimization. *changes*, 26:27, 2017.
- [174] Amy M Goodman, Robert A Oliver, Craig S Henriquez, and Patrick D Wolf. A membrane model of electrically remodelled atrial myocardium derived from in vivo measurements. *Europace*, 7(s2):S135–S145, 2005.
- [175] Elizabeth M Cherry, Joachim R Ehrlich, Stanley Nattel, and Flavio H Fenton. Pulmonary vein reentry properties and size matter: insights from a computational analysis. *Heart Rhythm*, 4(12):1553–1562, 2007.
- [176] Celal Alagoz, Saran Phatharodom, and Allon Guez. Parameter estimation of a phenomenological cardiac model based on a biophysically detailed model of human atria: A method for model complexity reduction using extended kalman filter. In *Modeling, Simulation, and Applied Optimization (ICMSAO), 2015 6th International Conference on*, pages 1–6. IEEE, 2015.
- [177] Celal Alagoz, John R Bullinga, and Allon Guez. Parameter fitting of a phenomenological model to a biophysically detailed model of human atria for action potential dynamics. *AIHLS2013*, page 9, 2013.
- [178] Arthur T Winfree. Varieties of spiral wave behavior: An experimentalists approach to the theory of excitable media. *Chaos: An Interdisciplinary Journal of Nonlinear Science*, 1(3):303–334, 1991.
- [179] Boris Y Kogan, Walter J Karplus, Brian S Billett, Alex T Pang, Hrayr S Karagueuzian, and Steven S Khan. The simplified fitzhugh-nagumo model with action potential duration restitution: effects on 2d wave propagation. *Physica D: Nonlinear Phenomena*, 50(3):327–340, 1991.
- [180] Arkady M Pertsov, Jorge M Davidenko, Remy Salomonsz, William T Baxter, and Jose Jalife. Spiral waves of excitation underlie reentrant activity in isolated cardiac muscle. *Circulation Research*, 72(3):631–650, 1993.
- [181] Richard A Gray, José Jalife, Alexandre Panfilov, William T Baxter, Cándido Cabo, Jorge M Davidenko, and Arkady M Pertsov. Nonstationary vortexlike reentrant activity as a mechanism of polymorphic ventricular tachycardia in the isolated rabbit heart. *Circulation*, 91(9):2454–2469, 1995.
- [182] Kirsten HWJ ten Tusscher and Alexander V Panfilov. Alternans and spiral breakup in a human ventricular tissue model. *American Journal of Physiology-Heart and Circulatory Physiology*, 291(3):H1088–H1100, 2006.
- [183] Isabelle Banville and Richard A Gray. Effect of action potential duration and conduction velocity restitution and their spatial dispersion on alternans and the stability of arrhythmias. *Journal of cardiovascular electrophysiology*, 13(11):1141–1149, 2002.

- [184] Hui-nam Pak, Soon Jun Hong, Gyo Seung Hwang, Hyun Soo Lee, Sang-weon Park, Jeong Cheon Ahn, Young Moo Ro, and Young-hoon Kim. Spatial dispersion of action potential duration restitution kinetics is associated with induction of ventricular tachycardia/fibrillation in humans. *Journal of Cardiovascular Electrophysiology*, 15(12):1357–1363, 2004.
- [185] A Giaquinta, S Boccaletti, and FT Arecchi. Superexcitability induced spiral breakup in excitable systems. *International Journal of Bifurcation and Chaos*, 6(09):1753–1759, 1996.
- [186] Athanasius FM Marée and Alexander V Panfilov. Spiral breakup in excitable tissue due to lateral instability. *Physical review letters*, 78(9):1819, 1997.
- [187] Alexandre V Panfilov. Spiral breakup as a model of ventricular fibrillation. *Chaos: An Interdisciplinary Journal of Nonlinear Science*, 8(1):57–64, 1998.
- [188] Manuel Cebrián, Manuel Alfonseca, and Alfonso Ortega. The normalized compression distance is resistant to noise. *IEEE Transactions on Information Theory*, 53(5):1895–1900, 2007.
- [189] Michael Burrows and David J Wheeler. A block-sorting lossless data compression algorithm. 1994.
- [190] James F Kaiser. On a simple algorithm to calculate the energy of a signal. In *Acoustics, Speech, and Signal Processing, 1988. ICASSP-88., 1988 International Conference on*, pages 381–384, 1990.
- [191] Andrew Y Ng, Michael I Jordan, Yair Weiss, et al. On spectral clustering: Analysis and an algorithm. *Advances in neural information processing systems*, 2:849–856, 2002.
- [192] Andrew R Cohen, Francisco LAF Gomes, Badrinath Roysam, and Michel Cayouette. Computational prediction of neural progenitor cell fates. *Nature methods*, 7(3):213–218, 2010.
- [193] Robert Tibshirani, Guenther Walther, and Trevor Hastie. Estimating the number of clusters in a data set via the gap statistic. *Journal of the Royal Statistical Society: Series B (Statistical Methodology)*, 63(2):411–423, 2001.
- [194] Maurits A Allesie. The electropathological substrate of longstanding persistent af: A new insight into caf mechanism. *Journal of Arrhythmia*, 27(Supplement):APSY2.5–APSY2.5, 2011.
- [195] Chung-Chuan Chou, Po-Cheng Chang, Ming-Shien Wen, Hui-Ling Lee, Tse-Ching Chen, San-Jou Yeh, and Delon Wu. Epicardial ablation of rotors suppresses inducibility of acetylcholine-induced atrial fibrillation in left pulmonary vein–left atrium preparations in a beagle heart failure model. *Journal of the American College of Cardiology*, 58(2):158–166, 2011.
- [196] IM Tsyganov, MA Tsyganov, AB Medvinskii, and GR Ivanitskii. Self-organization processes in strongly excitable media: Opened catalogue of new structures. In *Doklady Akademii Nauk*, volume 346, pages 825–832. Mezhdunarodnaya Kniga 39 Dimitrova UL., 113095 Moscow, Russia, 1996.

Appendix A: Minimal Resistor Model Equations

MRM is a phenomenological cardiac model with four state variables and three currents. The state variables are described as:

$$\dot{u} = I_{st} - (I_{fi} + I_{so} + I_{si}) \quad (\text{A.1})$$

$$\dot{v} = (1 - H(u - \theta_v))(v_\infty - v)/\tau_v^- - H(u - \theta_v)v/\tau_v^+ \quad (\text{A.2})$$

$$\dot{w} = (1 - H(u - \theta_w))(w_\infty - w)/\tau_w^- - H(u - \theta_w)w/\tau_w^+ \quad (\text{A.3})$$

$$\dot{s} = ((1 + \tanh(k_s(u - u_s)))/2 - s)\tau_s \quad (\text{A.4})$$

where u is membrane voltage, v , w , and s are gating variables. Three currents are defined as:

$$I_{fi} = -vH(u - \theta_v)(u - \theta_v)(u_u - u)/\tau_{fi} \quad (\text{A.5})$$

$$I_{so} = (u - u_o)(1 - H(u - \theta_w))/\tau_o + H(u - \theta_w)/\tau_{so} \quad (\text{A.6})$$

$$I_{si} = -H(u - \theta_w)ws/\tau_{si} \quad (\text{A.7})$$

where I_{fi} is the fast inward, I_{so} is the slow outward, I_{si} is the slow inward current, and $H(x)$ is

the standard Heaviside function. The time constants are defined as:

$$\tau_v^- = (1 - H(u - \theta_v^-))\tau_{v1}^- + H(u - \theta_v^-)\tau_{v2}^-\tau_w^- = \quad (\text{A.8})$$

$$\tau_w^- = \tau_{w1}^- + (\tau_{w2}^- - \tau_{w1}^-)(1 + \tanh(k_w^-(u - u_w^-)))/2 \quad (\text{A.9})$$

$$\tau_{so} = \tau_{so1} + (\tau_{so2} - \tau_{so1})(1 + \tanh(k_{so}(u - u_{so}))) / 2 \quad (\text{A.10})$$

$$\tau_s = (1 - H(u - \theta_w))\tau_{s1} + H(u - \theta_w)\tau_{s2} \quad (\text{A.11})$$

$$\tau_o = (1 - H(u - \theta_o))\tau_{o1} + H(u - \theta_o)\tau_{o2} \quad (\text{A.12})$$

and the infinite values are defined as:

$$v_\infty = \begin{cases} 1, & u < \theta_v^- \\ 0, & u \geq \theta_v^- \end{cases} \quad (\text{A.13})$$

$$v_\infty = (1 - H(u - \theta_o))(1 - u/\tau_{w\infty}) + H(u - \theta_o)w_\infty^* \quad (\text{A.14})$$

Appendix B: Minimal Resistor Model Parameters

Table B.1: Upper and lower bounds of MRM parameters

Param	Lower	Upper	Param	Lower	Upper
1. u_o	0	ϵ	15. τ_{fi}	0.05	0.125
2. u_u	1	1.75	16. τ_{o1}	300	600
3. θ_v	0.298	0.302	17. τ_{o2}	2	10
4. θ_w	ϵ	1.25	18. τ_{so1}	10	100
5. θ_v^-	ϵ	1.25	19. τ_{so2}	ϵ	5
6. θ_o	ϵ	1.25	20. k_{so}	1	10
7. τ_{v1}^-	10	200	21. u_{so}	0.45	0.65
8. τ_{v2}^-	1	1500	22. τ_{s1}	1	10
9. τ_v^+	0.1	3	23. τ_{s2}	2	20
10. τ_{w1}^-	5	450	24. k_s	1	10
11. τ_{w2}^-	5	450	25. u_s	0.8	1
12. k_w^-	10	250	26. τ_{si}	1	20
13. u_w^-	0.01	0.05	27. $\tau_{w\infty}$	0.005	0.5
14. τ_w^+	5	450	28. w_∞^*	0.4	1

Table B.2: Fitted Parameters of MRM for Afib-AP under dynamic stimuli.

Param	EKF	SQP	PSO	Param	EKF	SQP	PSO
1. u_o	ϵ	0.002	ϵ	15. τ_{fi}	0.06	0.05	0.02
2. u_u	1.35	1.0521	1.12	16. τ_{o1}	470	570	165
3. θ_v	0.302	0.298	0.3	17. τ_{o2}	6.05	10	7.1
4. θ_w	0.13	0.13	0.03	18. τ_{so1}	40	100	34
5. θ_v^-	0.2	0.2	0.7	19. τ_{so2}	1.35	5	1.86
6. θ_o	0.006	0.006	1.37	20. k_{so}	3.31	1.32	3.24
7. τ_{v1}^-	75	121	44	21. u_{so}	0.65	0.45	0.6
8. τ_{v2}^-	10	10	431	22. τ_{s1}	2.74	1	10.18
9. τ_v^+	2.48	1.495	1.41	23. τ_{s2}	2.44	16.6	8.59
10. τ_{w1}^-	6	197	48	24. k_s	1.63	1	0.07
11. τ_{w2}^-	140	20	229	25. u_s	0.91	.89	0.73
12. k_w^-	200	168	311	26. τ_{si}	3.75	9.21	2
13. u_w^-	0.046	0.045	0.027	27. $\tau_{w\infty}$	0.02	0.02	0.39
14. τ_w^+	280	206	79	28. w_∞^*	0.7	1	1

Table B.3: Parameters sets of MRM used for spiral wave generation

Param	EPI	ENDO	EKF	
1. u_o	0	0	0	
2. u_u	1.55	1.56	1.3649	
3. θ_v	0.3	0.3	0.3	
4. θ_w	0.13	0.13	0.13	
5. θ_v^-	0.006	0.2	0.2	
6. θ_o	0.006	0.006	0.006	
7. τ_{v1}^-	60	75	75	
8. τ_{v2}^-	1150	10	10	
9. τ_v^+	1.4506	1.4506	2.9958	
10. τ_{w1}^-	60	6	6	varied
11. τ_{w2}^-	15	140	140	varied
12. k_w^-	65	200	200	
13. u_w^-	0.03	0.016	0.0176	
14. τ_w^+	200	280	280	varied
15. τ_{fi}	0.11	0.1	0.0726	varied
16. τ_{o1}	400	470	470	
17. τ_{o2}	6	6	6.06	
18. τ_{so1}	30.0181	40	40.02	varied
19. τ_{so2}	0.9957	1.2	1.7695	
20. k_{so}	2.0458	2	3.2345	
21. u_{so}	0.65	0.65	0.4844	
22. τ_{s1}	2.7342	2.7342	2.7272	
23. τ_{s2}	16	2	2.2351	
24. k_s	2.0994	2.0994	1.4843	
25. u_s	0.9087	0.9087	0.8	
26. τ_{si}	1.8875	2.9013	3.4358	varied
27. $\tau_{w\infty}$	0.07	0.0273	0.0215	
28. w_∞^*	0.94	0.78	0.78	

Appendix C: Spiral Wave Generation

MRM was used to generate spiral waves. Detailed model equations are given in Appendix A. Six parameters τ_{w1}^- , τ_{w2}^- , τ_w^+ , τ_{fi} , τ_{so1} , τ_{si} out of twenty eight parameters is varied to generate different behaviors. Three parameter sets, EPI and ENDO from Bueno-Orovio et al.²² and EKF from Alagoz et al.¹⁷⁶, a parameter set generated to match a human atrial model CRN (Courtemanche et al.¹¹) AP and APD restitution properties, is chosen for remaining non-varying parameters. The parameter sets are shown in Table B.3 and the respective AP shapes and APD restitution properties when six parameters mentioned were not varied are shown in Figure C.1.

Using each of the parameter sets, three behavior types were aimed in the generation of spiral waves: stationary, meandering, and breakup. The mechanism for each behavior and their relation to the MRM parameters varied are elucidated in Section 5.1. For stationary spiral waves, tissue properties needed to be set to high excitability and less effective refractory dispersion. Therefore, small τ_{fi} , either greater τ_{w1}^- and freely varying τ_w^+ or smaller τ_w^+ and freely varying τ_{w1}^- were chosen. Snapshots of resulting behaviors in a compound image format are displayed in Figure C.2 for EPI, Figure C.3 for ENDO, and Figure C.4 for EKF. For meandering spiral waves, tissue with low excitability was arranged as effective refractory dispersion varied freely. Therefore greater τ_{fi} was chosen. Resulting behaviors are displayed in Figure C.5 for EPI, Figure C.6 for ENDO and EKF. For breakup on the other hand, tissue with higher excitability and effective refractory dispersion needed. For that, small τ_{fi} and relatively higher τ_w^- values were chosen.

Resulting behaviors are displayed in Figures C.7 and C.8 for EPI, Figures C.9 and C.10 for ENDO, and Figures C.11 and C.12 for EKF. Respective APs and APD restitution curves are also displayed for each parameter configuration. Stationary spiral waves were generally associated with rather smaller APDs and flat APD restitution curves whereas meandering spiral waves were generally associated with varying APDs and steeper APD restitution curves for smaller BCLs. In the case of spiral breakup, APDs were varied but not too small and APD restitution curves would repre-

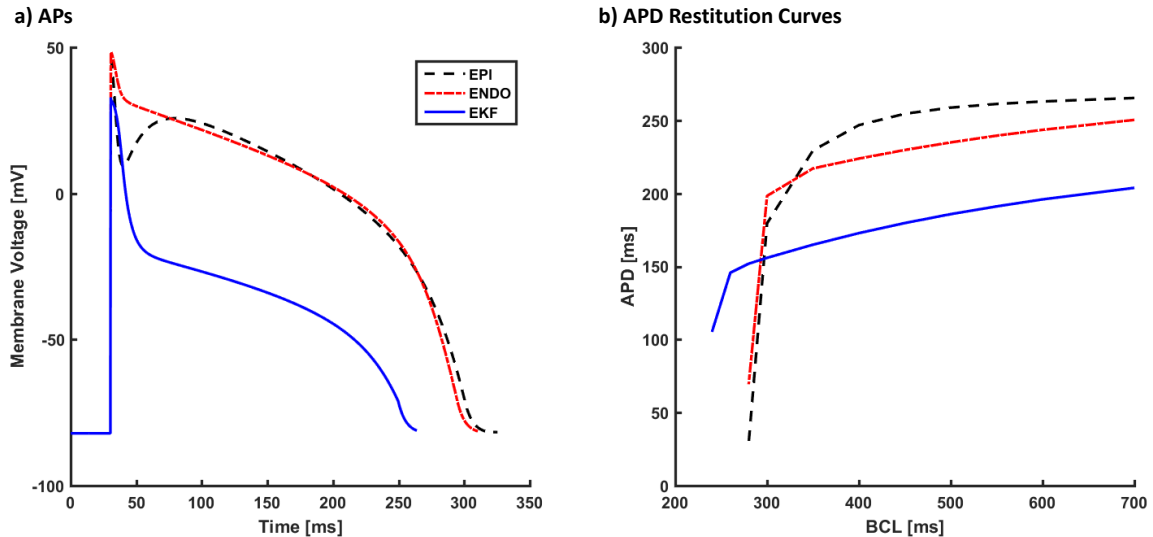


Figure C.1: Respective APs and APD restitutions for the parameter sets EPI, ENDO, and EKF.

sent higher and rather uniform with respect to BCL steepness. On some occasions different spiral behaviors resulted from what was aimed because parameter variations were not clipped and some combinations of them would unfold a variety of effective refractoriness dispersion. For instance, when generating breakup, parameter regimes associated with smaller APDs and rather flat APD restitution curves resulted stationary spiral waves. Furthermore, transitory behaviors are also observed as in the case of breakup generation again, transition from stationary to breakup yielded more organized rather than chaotic breakup behaviors with fewer wavelets. That certain behavior was named autocycling and described in (Tsyganov et al.¹⁹⁶). In some cases, the resulting behavior looked more like mother rotor (Fenton et al.¹⁴⁹) with a stationary spiral and wavelets at the tail which are either organized or chaotic.

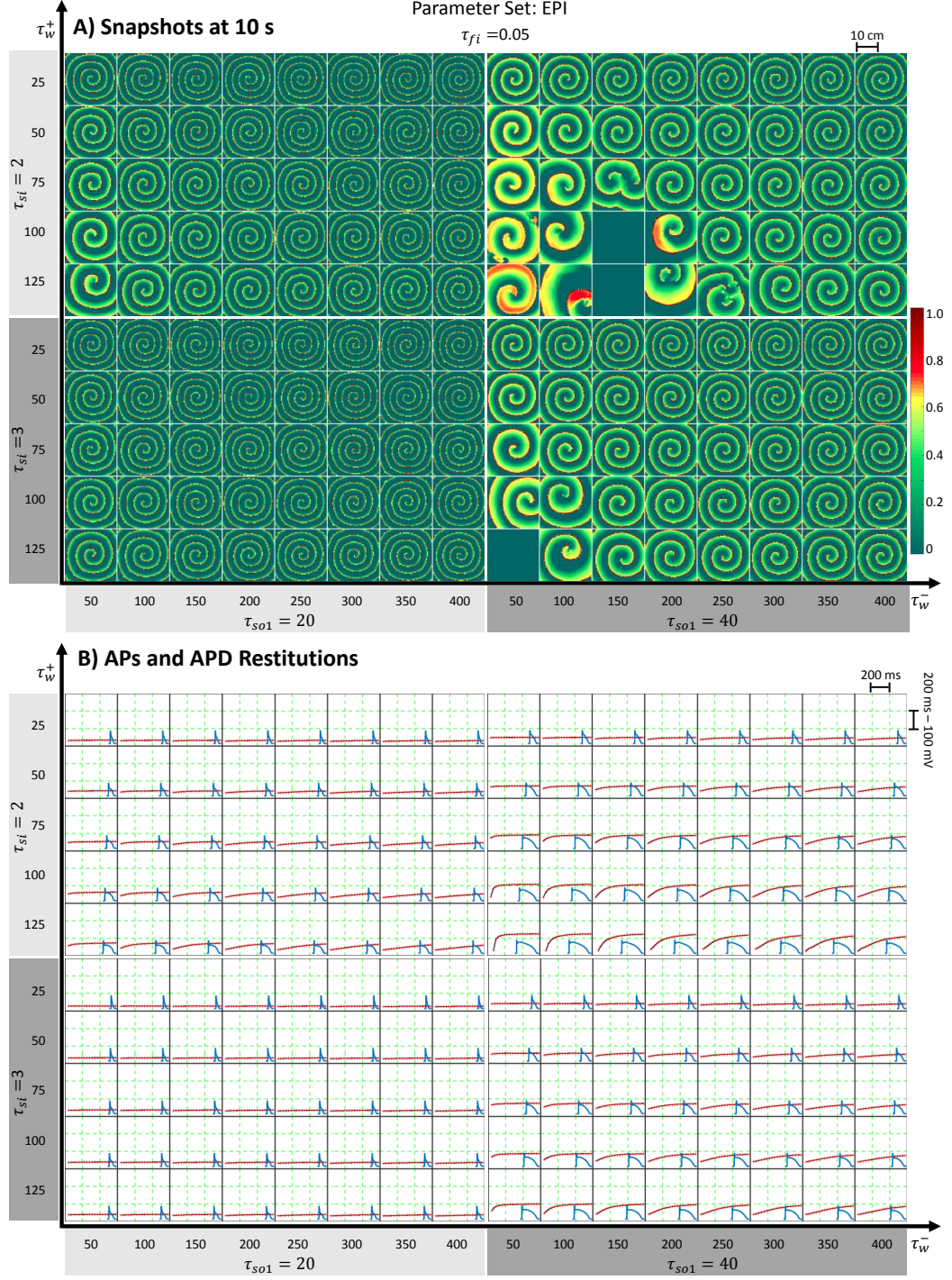


Figure C.2: Snapshots of spiral waves and their corresponding APs and APD restitutions when parameters varied for producing stationary spiral behaviors using the parameter set EPI. τ_{fi} is fixed at 0.05, τ_{si} is varied as 2 and 3, τ_w^+ varied between 25 and 125, τ_w^- is varied between 50 and 400, and τ_{so1} is varied as 20 and 40. Spiral wave led to breakup for same parameter combinations associated with longer APD and steeper APD restitution curves. Spiral wave is not sustained, indicated by the images with only green background, for the parameter regimes that result longer APDs.

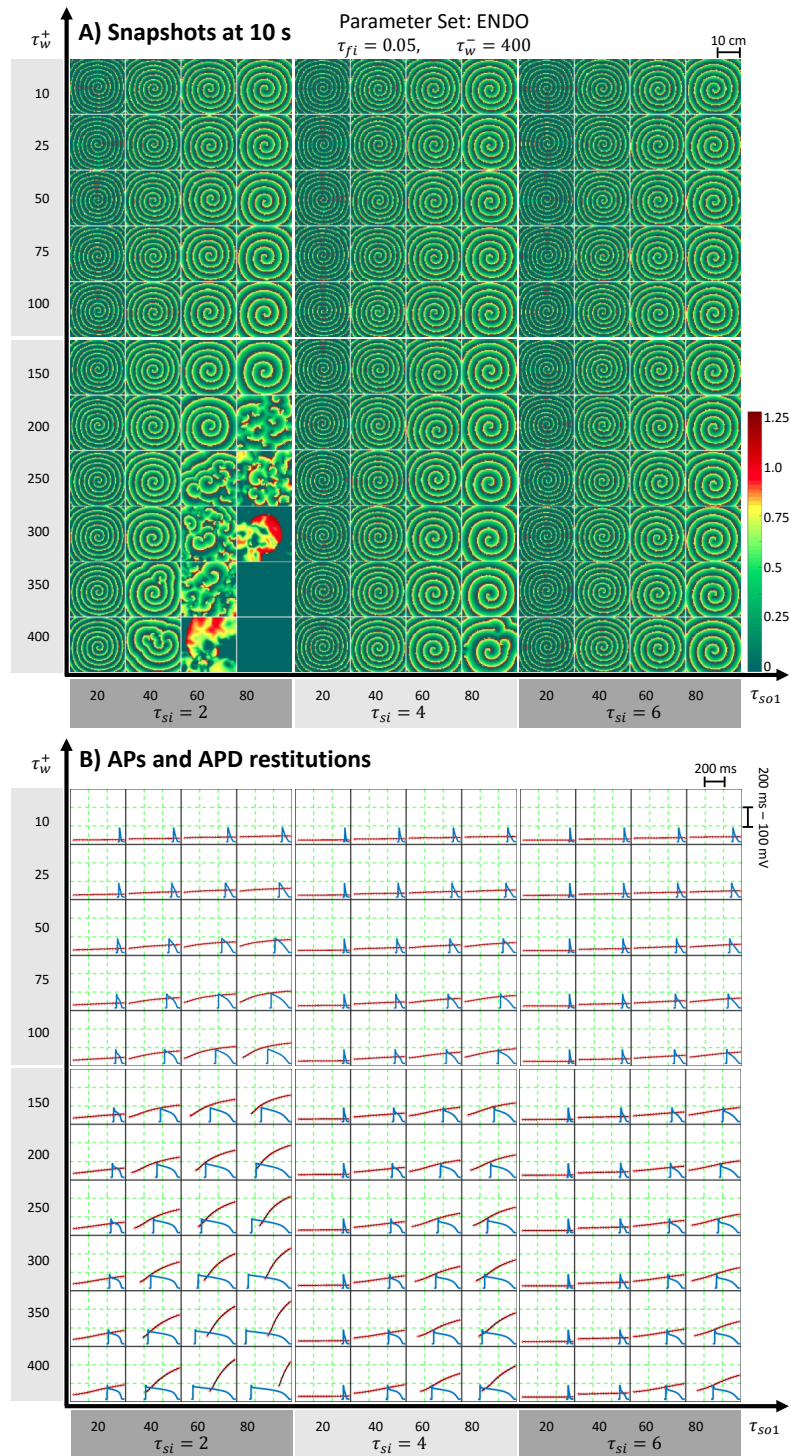


Figure C.3: Snapshots of spiral waves and their corresponding APs and APD restitutions when parameters varied for producing stationary spiral behaviors using the parameter set ENDO. τ_{fi} is fixed at 0.05, τ_{si} is varied between 2 and 6, τ_w^+ varied between 10 and 400, τ_w^- is fixed at 400, and τ_{so1} varied between 20 and 80. Spiral wave led to breakup for same parameter combinations associated with longer APD and steeper APD restitution curves. Spiral wave is not sustained, indicated by the images with only green background, for the parameter regimes that result longer APDs and highly steep APD resitution curves.

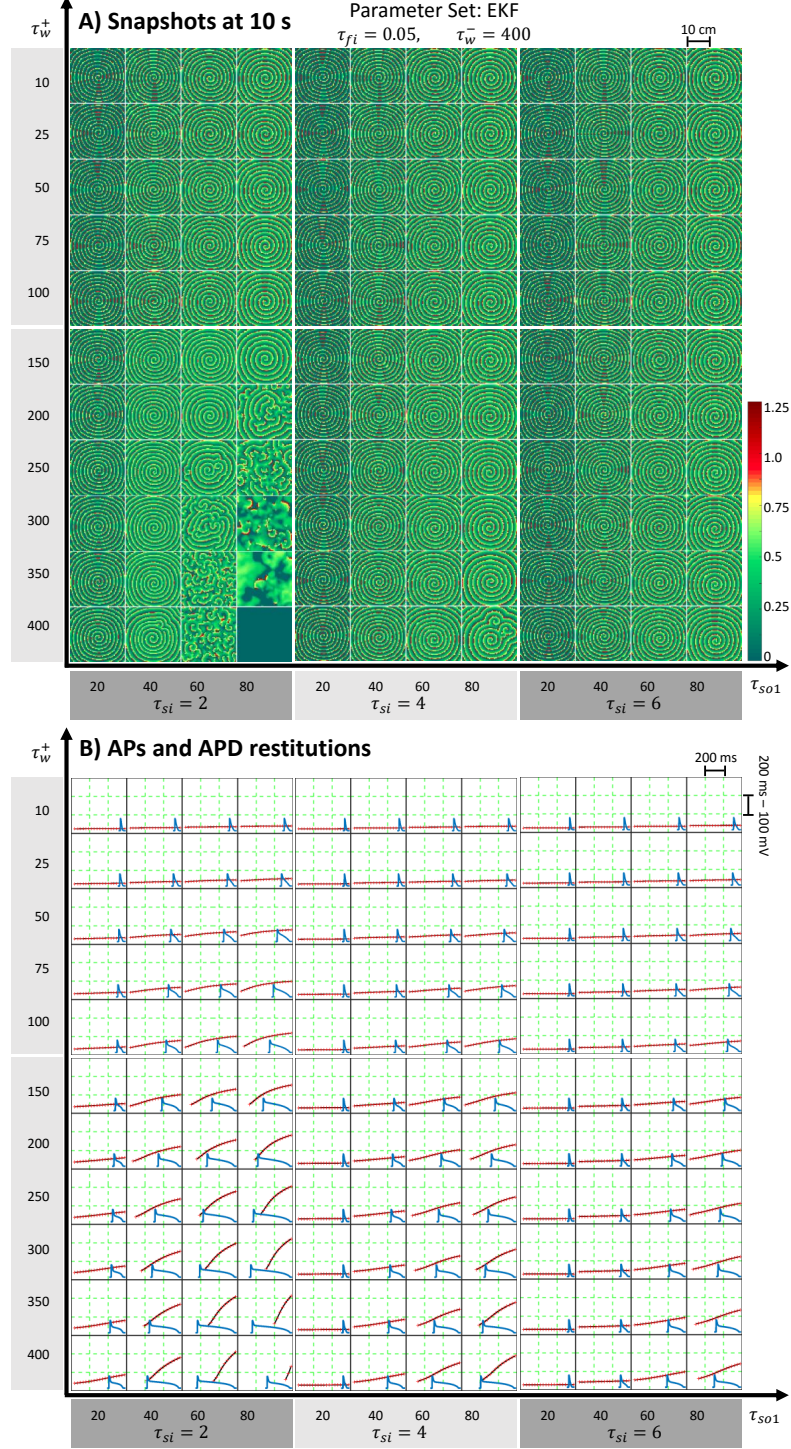


Figure C.4: Snapshots of spiral waves and their corresponding APs and APD restitutions when parameters varied for producing stationary spiral behaviors using the parameter set EKF. τ_{fi} is fixed at 0.05, τ_{si} is varied between 2 and 6, τ_w^+ varied between 10 and 400, τ_w^- is fixed at 400, and τ_{so1} varied between 20 and 80. Spiral wave led to breakup for same parameter combinations associated with longer APD and steeper APD restitution curves. Spiral wave is not sustained, indicated by the images with only green background, for the parameter regime that result longer APDs and highly steep APD restitution curves.

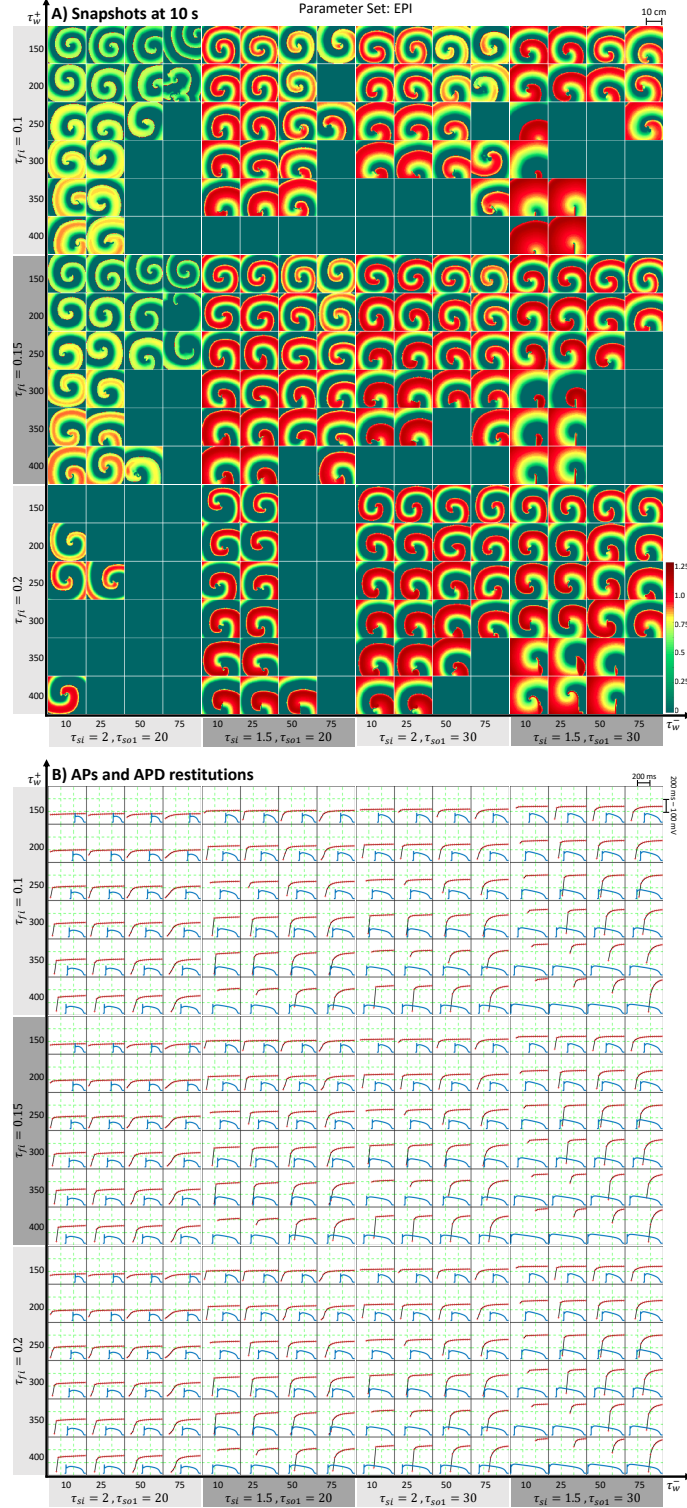


Figure C.5: Snapshots of spiral waves and their corresponding APs and APD restitution curves when parameters varied for producing meandering spiral behaviors using the parameter set EPI. τ_{fi} is varied as 0.1 and 0.2, τ_{si} is varied as 1.5 and 2, τ_w^+ varied between 150 and 350, τ_w^- varied between 50 and 400, and τ_{so1} varied between 30 and 50. Spiral wave is not sustained, indicated by the images with only green background, for parameter regimes that result longer APDs and highly steep APD restitution curves.

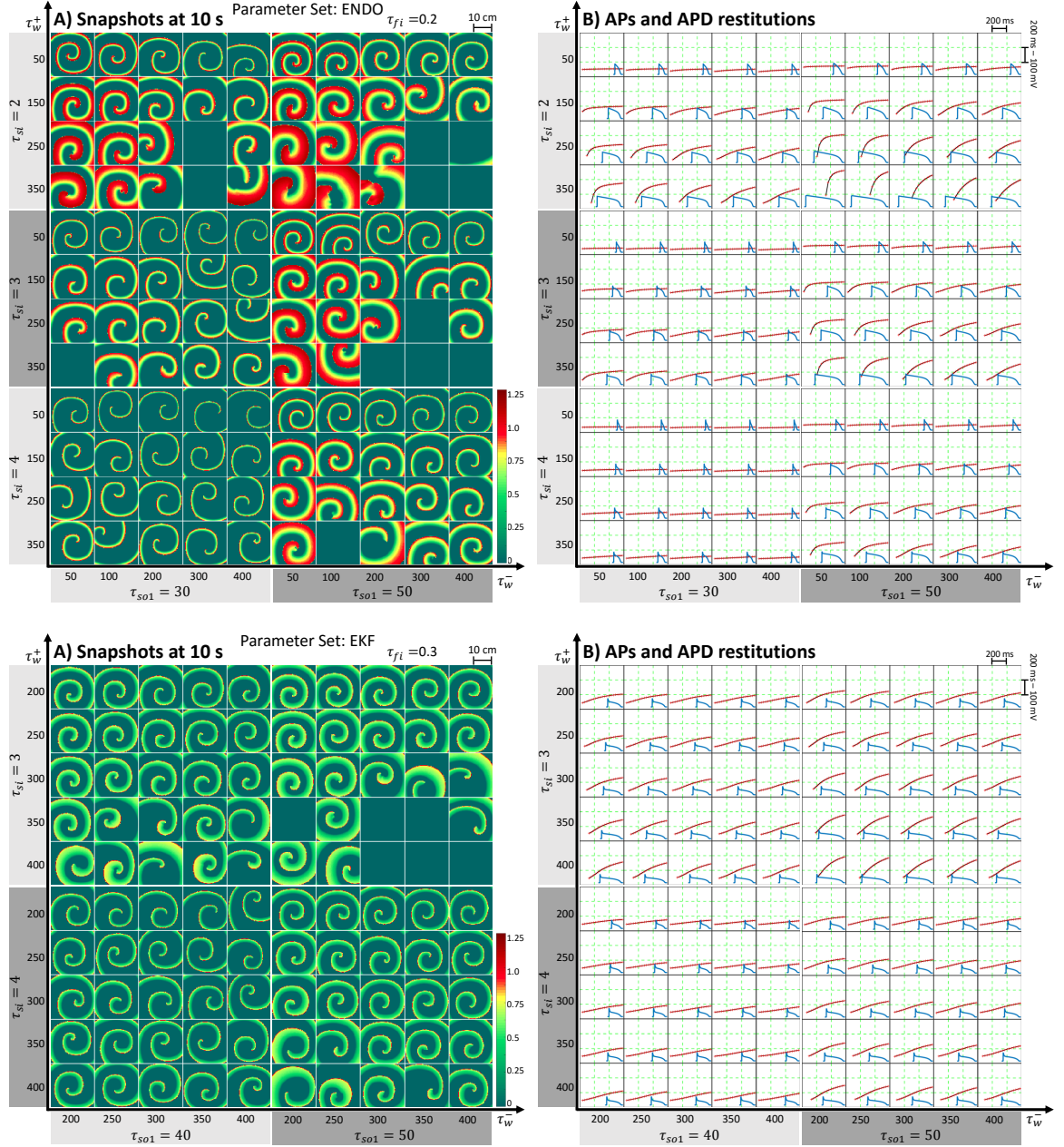


Figure C.6: Snapshots of spiral waves and their corresponding APs and APD restitutions when parameters varied for producing meandering spiral behaviors using the parameter set ENDO (top) and EKF (bottom). In case of ENDO, τ_{fi} is fixed at 0.2, τ_{si} is varied as 2 and 4, τ_w^+ varied between 50 and 350, τ_w^- varied between 50 and 400, and τ_{so1} varied between 30 and 50. In case of EKF, τ_{fi} is fixed at 0.3, τ_{si} is varied as 3 and 4, τ_w^+ varied between 200 and 400, τ_w^- varied between 200 and 400, and τ_{so1} varied between 40 and 50. Spiral wave is not sustained, indicated by the images with only green background, for parameter regimes that result longer APDs and highly steep APD resitution curves.

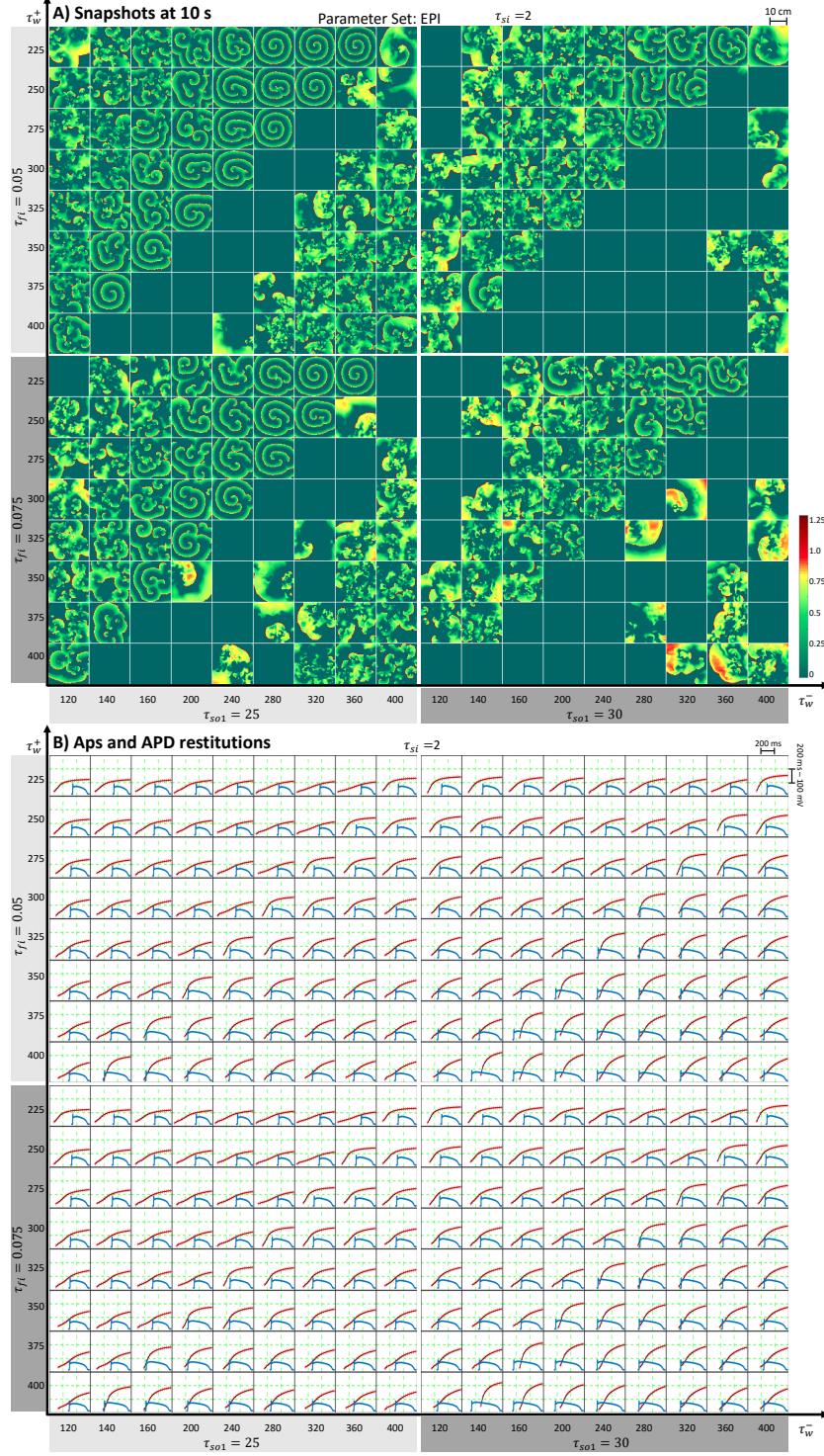


Figure C.7: Snapshots of spiral waves and their corresponding APs and APD restitutions when parameters varied for producing spiral breakup behaviors using the parameter set EPI. τ_{si} is fixed at 2, τ_{fi} is varied as 0.05 and 0.075, τ_w^+ varied between 225 and 400, τ_w^- varied between 120 and 400, and τ_{so1} varied between 25 and 30. Breakup did not take place for parameter regimes associated with shorter APDs and more flat APD restitution curve. Also, spiral wave is not sustained, indicated by the images with only green background, for parameter regimes that result longer APDs and highly steep APD resitution curves.

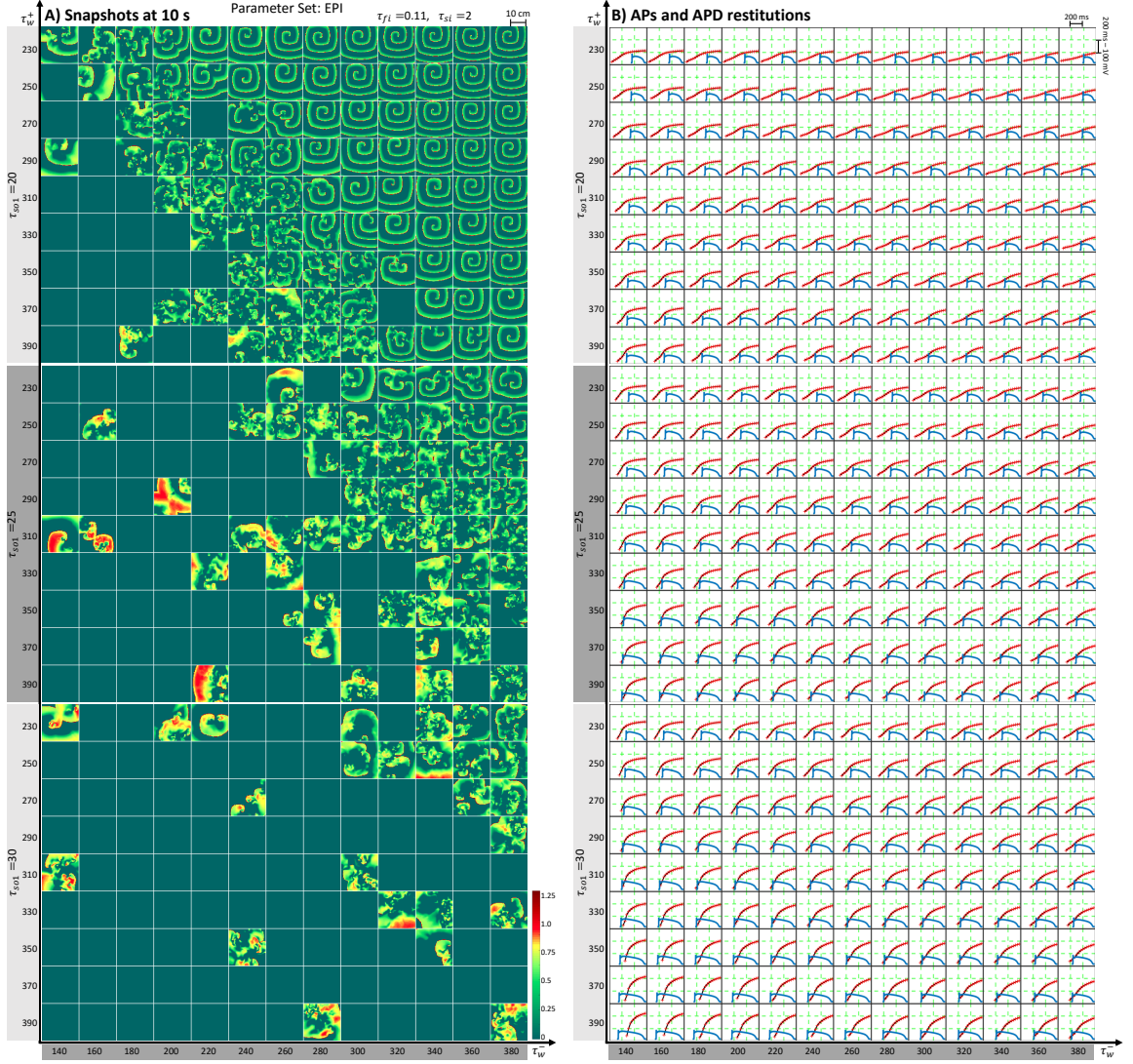


Figure C.8: Snapshots of spiral waves and their corresponding APs and APD restitution behaviors when parameters varied for producing spiral breakup behaviors using the parameter set EPI. τ_{fi} is fixed at 0.11, τ_{si} is fixed at 1.89, τ_w^+ varied between 230 and 390, τ_w^- varied between 140 and 380, and τ_{so1} varied between 20 and 30. Breakup did not take place for parameter regimes associated with shorter APDs and more flat APD restitution curve. Also, spiral wave is not sustained, indicated by the images with only green background, for parameter regimes that result longer APDs and highly steep APD restitution curves.

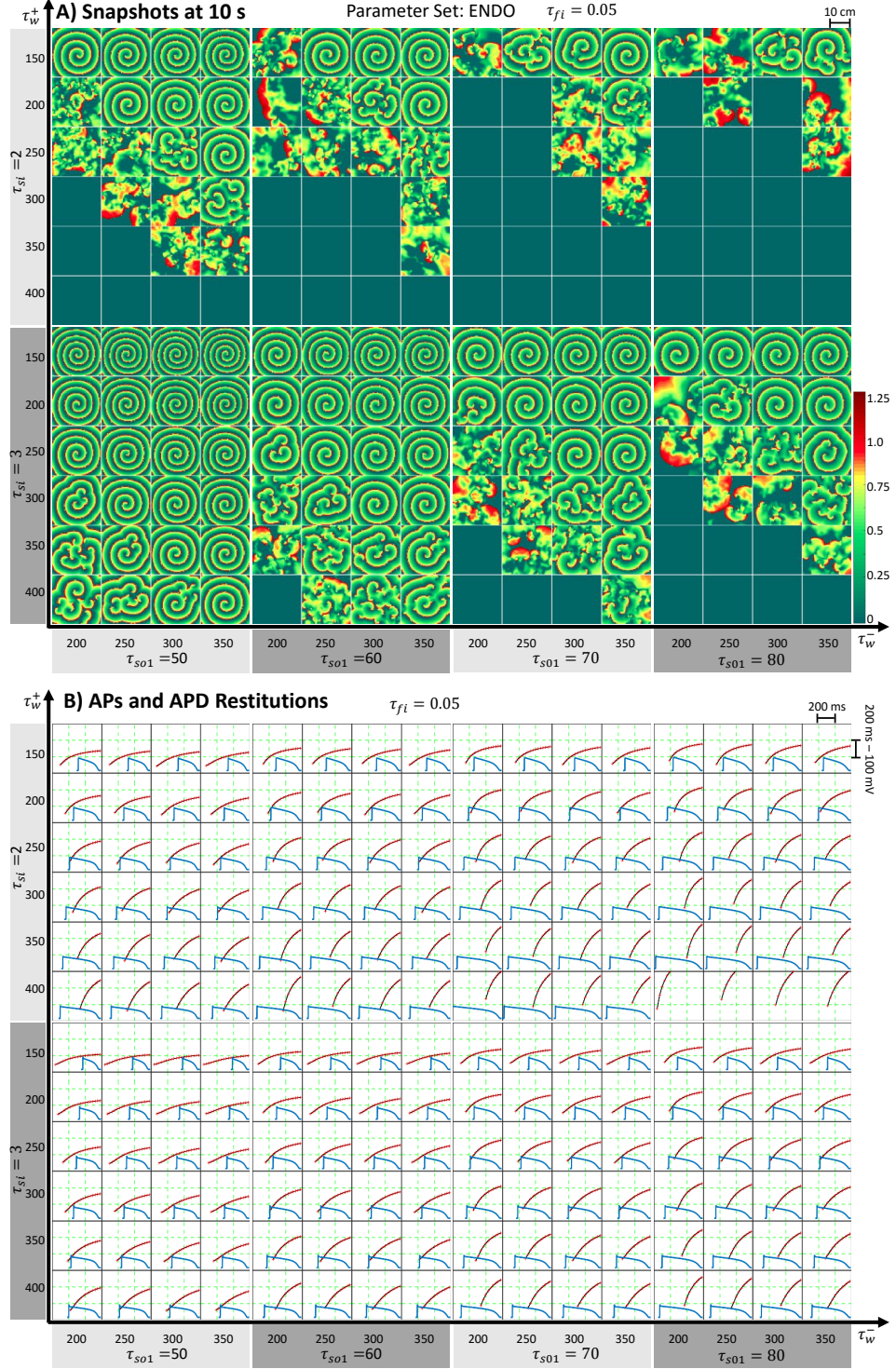


Figure C.9: Snapshots of spiral waves and their corresponding APs and APD restitutions when parameters varied for producing spiral breakup behaviors using the parameter set ENDO. τ_{fi} is fixed at 0.05, τ_w^+ varied between 150 and 400, τ_w^- varied between 200 and 400, τ_{si} varied as 2 and 3 and τ_{so1} varied between 40 and 60. Breakup did not take place for parameter regimes associated with shorter APDs and rather flat APD restitution curve. Also, spiral wave is not sustained, indicated by the images with only green background, for parameter regimes that result longer APDs and highly steep APD resitution curves.

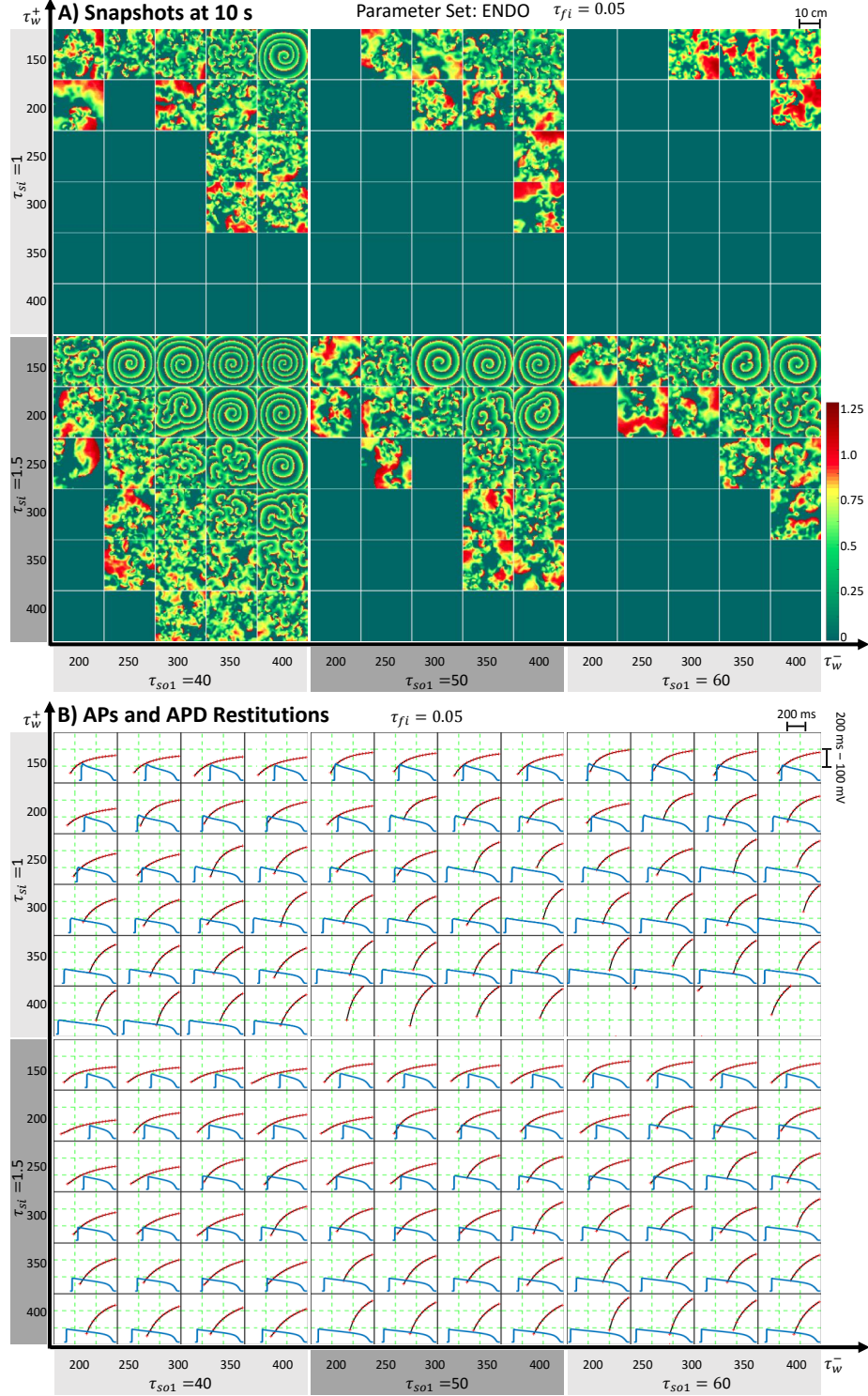


Figure C.10: Snapshots of spiral waves and their corresponding APs and APD restitutions when parameters varied for producing spiral breakup behaviors using the parameter set ENDO. τ_{fi} is fixed at 0.05, τ_w^+ varied between 150 and 400, τ_w^- varied between 200 and 350, τ_{si} varied as 1 and 1.5 and τ_{so1} varied between 40 and 60. Breakup did not take place for parameter regimes associated with shorter APDs and rather flat APD restitution curve. Also, spiral wave is not sustained, indicated by the images with only green background, for parameter regimes that result longer APDs and highly steep APD restitution curves.

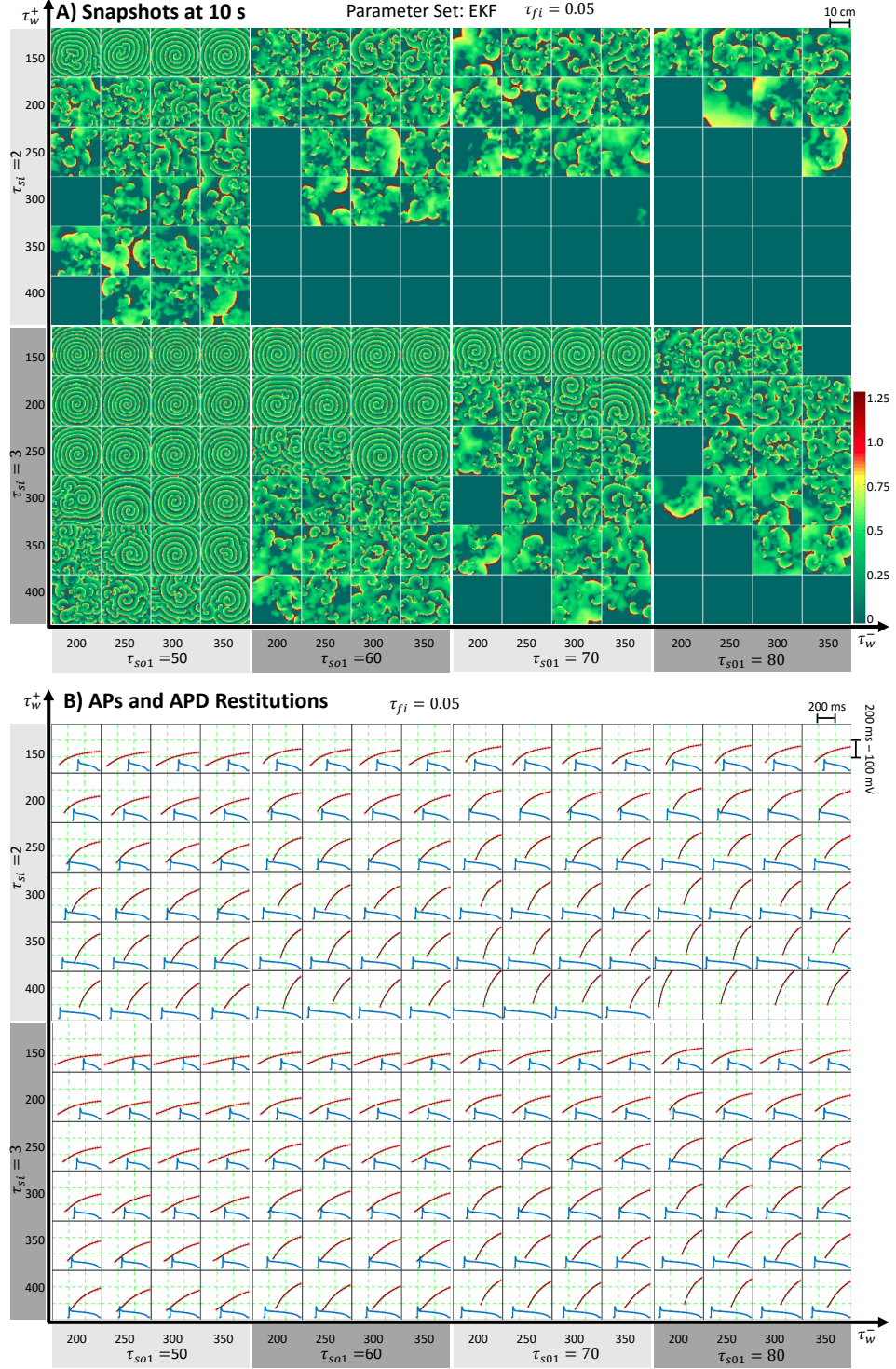


Figure C.11: Snapshots of spiral waves and their corresponding APs and APD restitutions when parameters varied for producing spiral breakup behaviors using the parameter set EKF. τ_{fi} is fixed at 0.05, τ_w^+ varied between 150 and 400, τ_w^- varied between 200 and 350, τ_{si} varied as 2 and 3 and τ_{so1} varied between 40 and 60. Breakup did not take place for parameter regimes associated with shorter APDs and rather flat APD restitution curve. Also, spiral wave is not sustained, indicated by the images with only green background, for parameter regimes that result longer APDs and highly steep APD resitution curves.

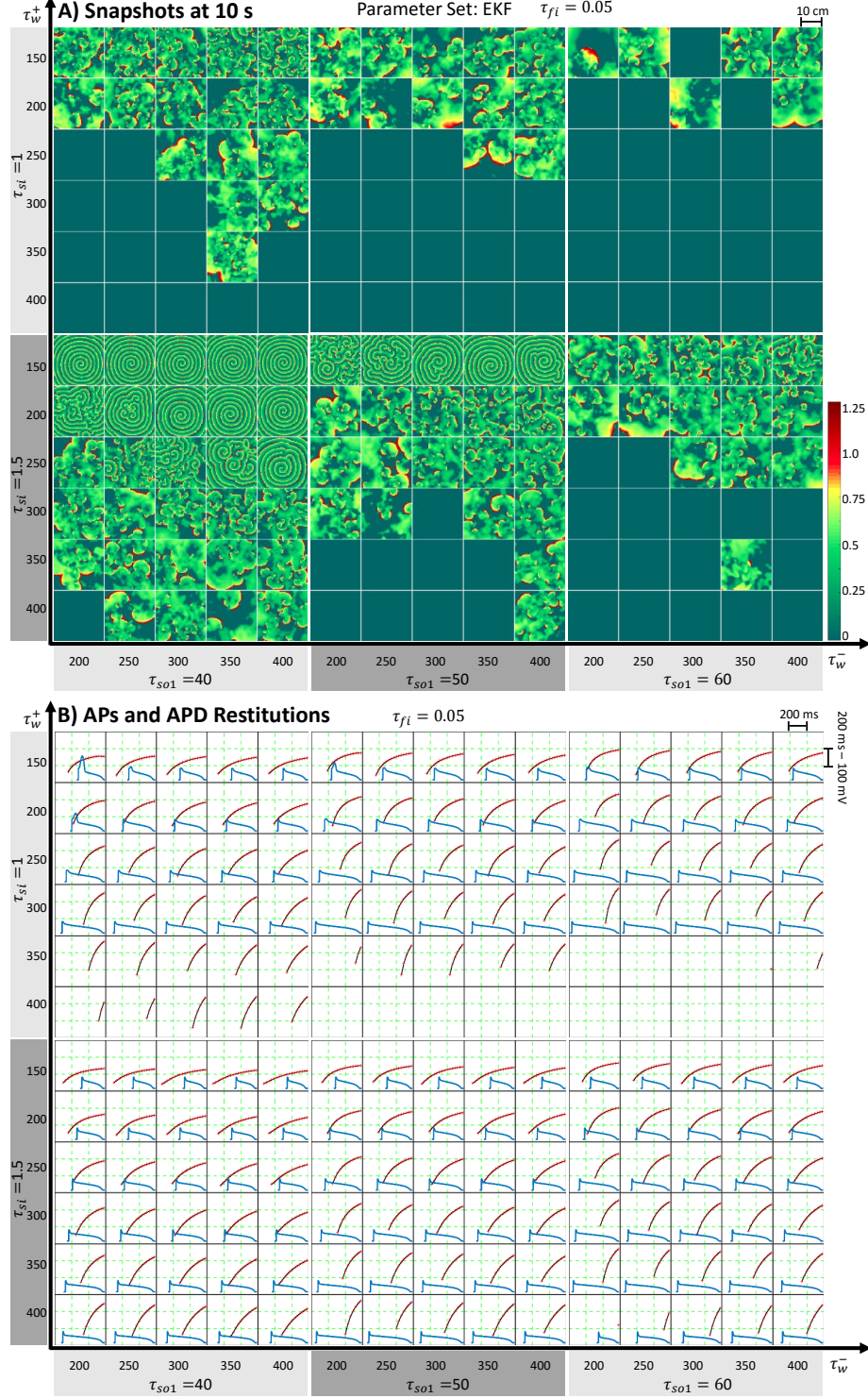


Figure C.12: Snapshots of spiral waves and their corresponding APs and APD restitutions when parameters varied for producing spiral breakup behaviors using the parameter set EKF. τ_{fi} is fixed at 0.05, τ_w^+ varied between 150 and 400, τ_w^- varied between 200 and 400, τ_{si} varied as 1 and 1.5 and τ_{soi1} varied between 40 and 60. Breakup did not take place for parameter regimes associated with shorter APDs and rather flat APD restitution curve. Also, spiral wave is not sustained, indicated by the images with only green background, for parameter regimes that result longer APDs and highly steep APD restitution curves.

Vita

Celal Alagöz

Date of Birth March 5, 1983

Place of Birth Kahramanmaraş, Turkey

Education BS in Electrical Engineering, Yıldız Technical University, 2006
MSE in Electrical and Computer Engineering, The Johns Hopkins University, 2010

Journal Publications C. Alagoz, A.R. Cohen, D.R. Frisch, B. Tunç, S. Phatharodom, A. Guez, "In silico Cardiac Electric Rotor Classification Using Normalized Compression Distance", *Biomed Eng Online*, [submitted in March 2017].

C. Alagoz, S. Phatharodom, A. Guez, "Complexity Reduction in Cardiac Modeling Using Extended Kalman Filter", *JRAT*, [submitted in March 2017]

C. Alagoz, A.R. Cohen, D.R. Frisch, B. Tunç, S. Phatharodom, A. Guez, "Spiral Waves Clustering: Implications for an Automated Cardiodynamic Tissue Characterization", *Comput Methods Programs Biomed*, [submitted in Feb 2017].

Conference Publications C. Alagoz, A. Guez, A. R. Cohen, J. R. Bullinga, Spiral Wave Classification Using Normalized Compression Distance: Towards Atrial Tissue Spatiotemporal Electrophysiological Behavior Characterization, In *Engineering in Medicine and Biology Society (EMBC), 2015 37th Annual International Conference of the IEEE*, pp. 4503-4506. IEEE, 2015.

C. Alagoz, S. Phatharodom, A. Guez, Parameter Estimation of a Phenomenological Cardiac Model based on a Biophysically Detailed Model of Human Atria: A Method for Model Complexity Reduction Using Extended Kalman Filter, In *Modeling, Simulation and Applied Optimization (ICMSAO), 2015 6th International Conference*, pp. 1-6. IEEE, 2015.

C. Alagoz, A.R. Cohen, A. Guez, J.R. Bullinga, "Spiral Waves Clustering Using Normalized Compression Distance", In *Computing in Cardiology Conference (CinC) 2014*, pp. 221-224. IEEE, 2014.

C. Alagoz, J.R. Bullinga, A. Guez, Parameter Fitting of a Phenomenological Model to a Biophysically Detailed Model of Human Atria for Action Potential Dynamics, In *AIHLS2013*, p. 9, 2013.

